INTRAMOLECULAR ELECTRONIC COMMUNICATION BETWEEN

DIMETAL UNITS WITH MULTIPLE METAL–METAL BONDS

A Dissertation

by

ZHONG LI

Submitted to the Office of Graduate Studies of
Texas A&M University
in partial fulfillment of the requirements for the degree of

DOCTOR OF PHILOSOPHY

August 2007

Major Subject: Chemistry

INTRAMOLECULAR ELECTRONIC COMMUNICATION BETWEEN

DIMETAL UNITS WITH MULTIPLE METAL–METAL BONDS

A Dissertation

by

ZHONG LI

Submitted to the Office of Graduate Studies of
Texas A&M University
in partial fulfillment of the requirements for the degree of

DOCTOR OF PHILOSOPHY

Approved by:

Co-Chairs of Committee, Carlos A. Murillo
                             John P. Fackler, Jr.
Committee Members,   Donald J. Darensbourg
                             Francois P. Gabbaï
                             Max D. Summers
Head of Department,   David H. Russell

August 2007

Major Subject: Chemistry

ABSTRACT

Intramolecular Electronic Communication Between Dimetal Units with Multiple

Metal–Metal Bonds. (August 2007)

Zhong Li, B.S., Nanjing University

Co-Chairs of Advisory Committee: Dr. Carlos A. Murillo
Dr. John P. Fackler, Jr.

Intramolecular electron transfer between a donor and an acceptor group is a fundamental process with considerable implications in chemistry, biology, physics and molecular electronics. In this work, quadruply bonded dimolybdenum units have been employed to build supramolecules, including dimer of dimers and tetranuclear clusters. Electronic communication between the dimetal units has been investigated both experimentally and theoretically.

Dimer of dimers, described by a general formula [Mo$_2$]L[Mo$_2$], where [Mo$_2$] = [Mo$_2$(DAniF)$_3$]$^+$ and DAniF = N,N'–di–p–anisylformamidinate, have been synthesized and these compounds can be chemically oxidized in a controllable way. The molecular structures and electronic properties of these complexes have been modified by changes in the bridging ligands. In this work, diamidates, fluoflavinate and dithioxamidates have been utilized as bridging ligands, L. It was found that, generally, the electronic coupling between the metal centers increases as substitution of O–donor atoms to N or S in the linkers, if the substution does not change the structure substantially. Density Functional Theory calculations on model compounds show that metal to ligand back bonding is critical to the electron transfer pathway.

Tetranuclear Mo_4 clusters with two $[Mo_2(cis–DAniF)_2]^{2+}$ units linked by single atoms usually show large electronic communication, attributed to the short separation between dimetal units and possible direct δ to δ orbital interactions. In this dissertation the shortest distance between the dimetal centers, ca. 3.25 Å, were found for the compounds linked by alkoxides, $[Mo_2(cis–DAniF)_2]_2(\mu–OR)_4$, R = Me or Et. The separation between the dimetal units decreases as $[Mo_2(cis–DAniF)_2]_2(\mu–OCH_3)_4$ is singly and then doubly oxidized, which suggests bond formation between dimetal centers. The analogous tetranuclear compounds linked by bidentate bridges, $[Mo_2]_2(\mu–X—X)_2$ (X = O or S), have also been obtained. $[Mo_2(cis–DAniF)_2]_2(\mu–o–S_2C_6H_4)_2$ shows an exceptionally strong electronic coupling due to super–exchange pathway, even though the $Mo_2\cdots Mo_2$ distance of 3.724 Å is considerably larger than 3.267 Å for the corresponding O bridged compound.

DEDICATION

To Nini

ACKNOWLEDGEMENTS

TABLE OF CONTENTS

LIST OF FIGURES

FIGURE   Page

LIST OF TABLES

CHAPTER I

INTRODUCTION

Electron transfer processes permeate virtually all aspects of chemical, physical, and biological sciences ranging from photosynthesis and multiple enzymatic routes to simpler redox processes.[1] Compounds with two redox sites, particularly those in which there are chemically identical metal–containing subunits, mainly single metal ion sites, have been extensively studied to understand the fundamentals of intramolecular electron transfer or electronic communication.[2] A classic example is the pyrazine bridged diruthenium complexes, $[Ru(NH_3)_5]pry[Ru(NH_3)_5]^{n+}$ ($n = 4$–6), prepared by Creutz and Taube in the late 1960s.[3] In the mixed valence (MV) species $[Ru(NH_3)_5]pry[Ru(NH_3)_5]^{5+}$ and many other MV compounds, the electronic communication or electronic coupling between the units depends on the nature of the linker. The odd electron may stay on one end, move back and forth between the metal centers, or equally distribute on both sites. A large number of experiments and theoretical efforts have been devoted to determine the factors that affect the strength of electronic coupling. Conjugated electron carriers, such as polyenes, polyphenyls, polyynes and polypyrroles are the frequently used bridges to promote the electronic coupling between terminal subunits,[4] and in many cases, the electronic coupling is found to decrease according to an exponential law.[5] These complexes can potentially be

---

This dissertation follows the style of *Inorganic Chemistry*.

used as molecular wires or single–molecule transistors and also as electronic components for a new generation of computers.

Because understanding electron transfer processes within various components of a molecule is fundamental to many fields with considerable implications, many techniques employing electrochemical, spectroscopic, and magnetic measurements have been used to evaluate the electronic communication between metal units and the effect of the linker. In general, the electrochemistry of these compounds show two successive one–electron redox processes, and the separation between the two $E_{1/2}$ values, $\Delta E_{1/2}$, is associated with the comproportionation constant Kc (Scheme 1).

Scheme 1

$$M^{II} \sim M^{II} + M^{III} \sim M^{III} \xrightleftharpoons{\quad K_c \quad} 2M^{III} \sim M^{II}$$

$$Kc = e^{\Delta E_{1/2}/25.69}$$
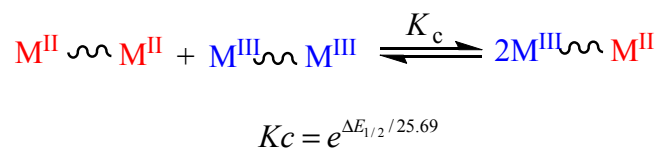
The comproportionation constant Kc, which is exponentially related to $\Delta E_{1/2}$, measures the thermodynamic stability of the mixed–valence species, and has also been used to evaluate the extent of electronic communication between redox sites. It is usually accepted that comproportionation constants above 10^6 (for which a $\Delta E_{1/2}$ of 355 mV would be required) justify the assumption that delocalization occurs. [6] The Creutz–Taube ion barely meets this criterion ($\Delta E_{1/2} = 390$ mV; Kc $= 3.9 \times 10^6$).

Recently, covalently bonded dimetal units have been used to assemble supramolecules and a variety of geometries have been obtained including dimers, loops, squares, triangles, complex polygons, and extended three–dimensional materials.[7,8]

These systems resemble those with single metal atoms in some respects, but in others they provide significant advantages and new probes in the electronic interaction between the metal sites. For example, because of the variability in the time–resolution of the various techniques, there is still uncertainty in Creutz–Taube ion (C–T) regarding the location of the odd electron. In principle, the question might be answered by structure determination that would show distinct structural differences between one end of the molecule (Ru^{II}) and the other (Ru^{III}) for a localized $Ru^{+2}LRu^{+3}$, while no difference for a delocalized system $Ru^{+2.5}LRu^{+2.5}$. Unfortunately, for the two crystalline forms of the series of C–T ion, one with chloride counter ions and one with tosylate anions, the detectable structural differences between the Ru^{II} and Ru^{III} units are negligible.[9] However, the crystal structures and electronic configurations for dimetal units with multiple metal–metal bonds have been well studied. For instance, removal of an electron from dimetal units such as M_2^{4+}, M = Mo, W, changes the electronic configuration from of $\sigma^2\pi^4\delta^2$ to $\sigma^2\pi^4\delta^1$ and the bond order decreases from 4 to 3.5 (Figure 1). Consequently, the bond distance lengthens by 0.04–0.06 Å.[10] The structural change can be precisely and unambiguously measured by X–ray crystallography and used to monitor the localization or delocalization of charge. This was clearly shown by the compounds with two dimolbydenum units linked by $M(OR)_4^{2-}$ (M = Zn, Co). The singly oxidized species $[Mo_2](CH_3O)_2M(CH_3O)_2[Mo_2](PF_6)$ show asymmetric molecular structures with two distinct [Mo_2] units. In each case, one of the [Mo_2] units has a lengthened Mo–Mo bond distance of 2.151[1] Å, as expected for one–electron oxidation, whereas the other remains unchanged at 2.115[1] Å.[11] The crystallographic results thus show

unambiguously that in the crystalline state the mixed–valence compounds are electronically localized and the unpaired electron is trapped on one [Mo$_2$] unit.
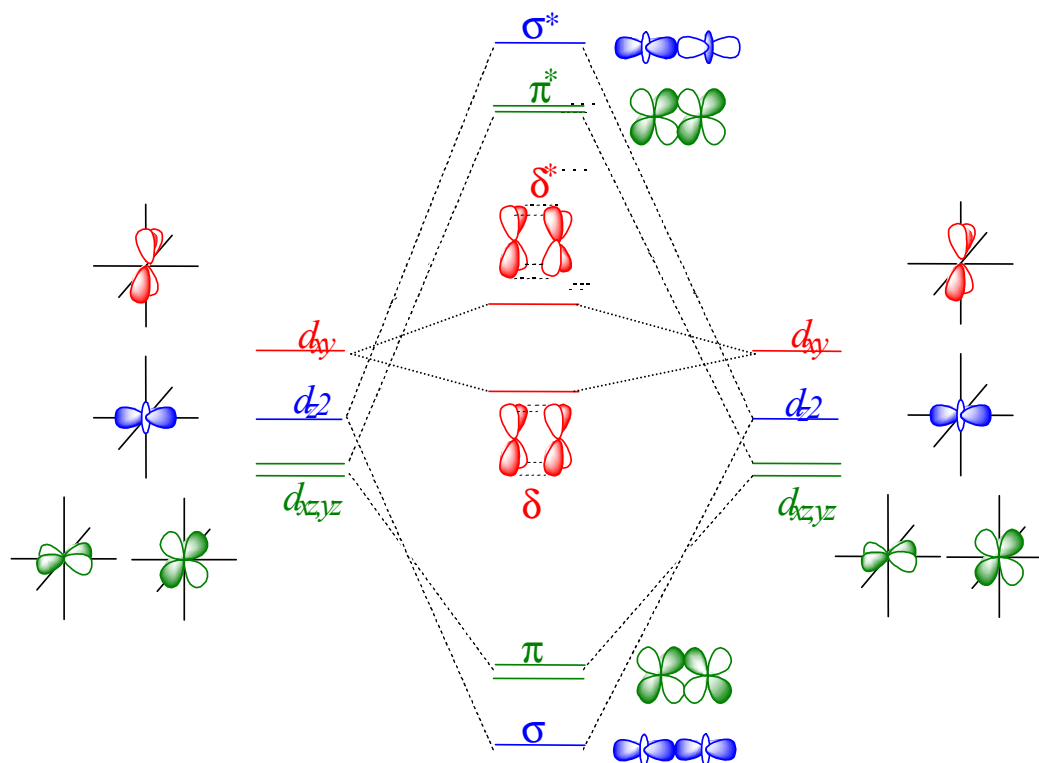
Figure 1. Molecular orbital diagram for quadruply bonded dimetal units, Mo$_2^{n+}$ (n = 4, 5, 6).

Some other advantages using dimetal units instead of single metals sites include: (1) Dimetal units can be used to create neutral rather than highly positive charged oligomers, which can then be oxidized in a controlled way, with retention of structural integrity. (2) An enormous range of metals are potentially available to form homologous structures. (3) A very large variety of organic ligands may be used to modulate the interaction between dimetal units. For example, by selectively changing the linkers, different level of electronic communication between dimetal units ranging from $K_c = 4$ to $K_c = 6.2 \times 10^{13}$ have been obtained.[12]

The general goal of this research is to gain more insight into the fundamental aspects of intramolecular electronic communication employing metal–metal bonded metal units, specifically the pursuit of systems with strong electronic coupling and gathering information on the electron transfer pathways. This work has mainly focused on two types of compounds with two quadruply bonded dimolybdenum units, namely, dimer of dimers (a) and tetranuclear clusters (b) (Scheme 2).

Scheme 2

(a)   (b)
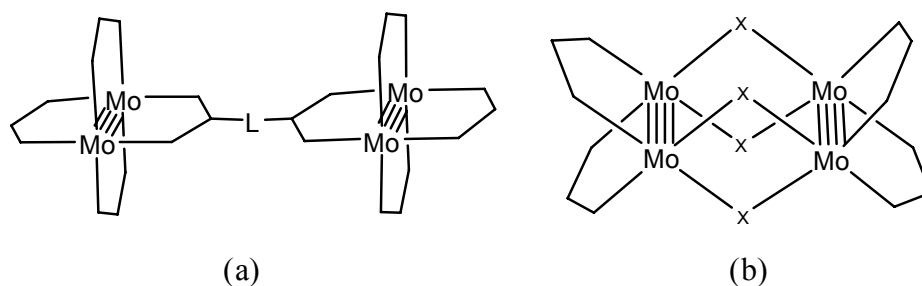
For the dimer of dimers, the first series compounds are those linked by dicarboxylates. The dimolybdenum units $[(Bu^tCO_2)_3Mo_2]^+$ and $[(DAniF)_3Mo_2]^+$ (DAniF = N,N'–di–p–anisylformamidinate) were utilized.[13] Similarly to compounds with single–metal units, the communication is enhanced when linkers have conjugated systems instead of saturated structures. Furthermore, in compounds of the form $[(DAniF)_3Mo_2]_2(\mu-O_2C(CH=CH)_nCO_2]$, where n = 0–4, communication diminishes as the separation between Mo_2 units increases. The greatest $\Delta E_{1/2}$ value of 212 mV is found for the oxalate linked compound.[14,15] The planar conformation of this compound at solid state is not retained in solution and free rotation along the central C–C is possible.

Some functionalization on the dicarboxylates was also performed to modify the electronic communication. For example, introducing hydroxyl groups to the terephthalate linker, the dihedral angles between the terephthalate C_6 ring and the two CO_2 units can be controlled, and consequently the degree of interaction can be switched as shown in the Scheme 3 below.[16] Other efforts to modify dicarboxylate bridges include the use of thienyl dicarboxylates or unsymmetrical polar bridges.[17] Overall, the dicarboxylate bridges only afford relatively weak electronic coupling (Scheme 3).

Scheme 3

$$[(DAniF)_3Mo_2](oxalate)[Mo_2(DAniF)_3]$$

$= N,N'\text{-di}(p\text{-anisyl})formamidinate\ (DAniF)$
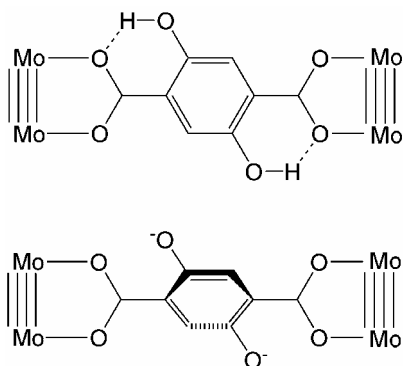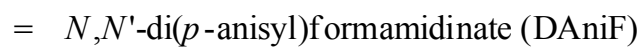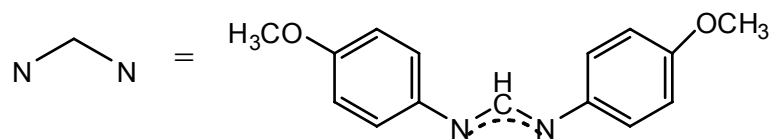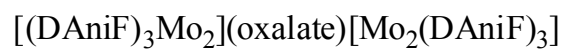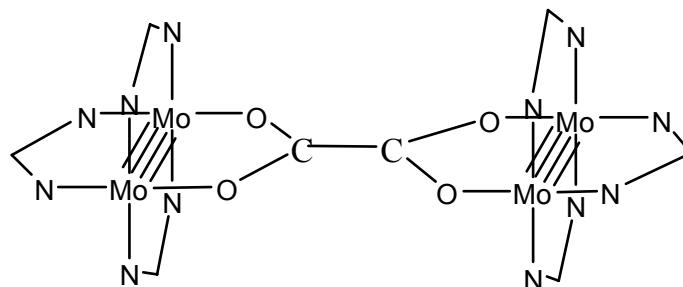
Figure 2. Generic representation of a dimer of dimolybdenum units linked by an oxalate dianion.

Compared to dicarboxylate anions, isoelectronic diamidate groups (shown in the Scheme 4 below) have drawn much less attention as linkers for supramolecular arrays. Because amidate groups are much stronger Lewis bases than the corresponding carboxylate groups, it is anticipated that the resulting complexes would be thermodynamically more stable than the carboxylate prototypes. Preliminary study using diamidate ligands shows that the electronic communication is greater than that for the analogous dicarboxylate bridged compounds (Scheme 4).[18]

Scheme 4

dicarboxylate   diamidate
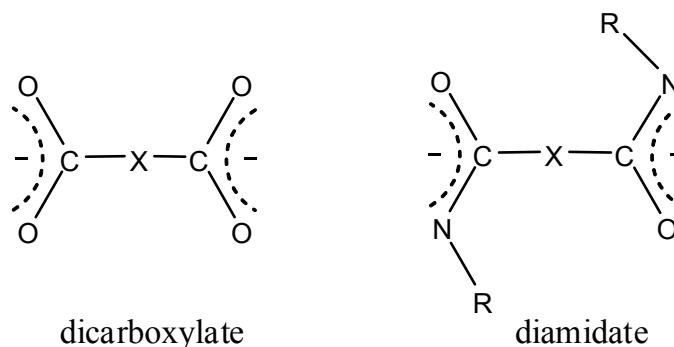
Remarkably, two isomers varying in linkage conformation, namely, α and β, have been obtained as diaryoxamidate ligands, ⁻RN(O)C–C(O)NR⁻ (C₆H₅, p–CH₃OC₆H₄), were used as the linker.[19] In the α form, the amidate linker was non planar, with the two RN(O)C planes being approximately perpendicular. For the β form, the C–C unit and the Mo–Mo bonds essentially parallel to each other, and the oxidized species have a heteronaphthalene–like structure. When the substituted R groups are CH₃ groups, only the β form has been obtained.[20] It is speculated that the even if the α form might be kinetically favored, the β form is so much more thermodynamically favored that no α

form can survive long enough to be seen. The α and β isomers show distinct electronic communication as the $\Delta E_{1/2}$ for the redox processes of Mo_2 units is significantly larger for the β isomers. This is supported also by the structural differences, EPR spectrum and the intervalence charge–transfer band in the near infrared region upon oxidation of the two isomers (Scheme 5).

Scheme 5

α form   β form
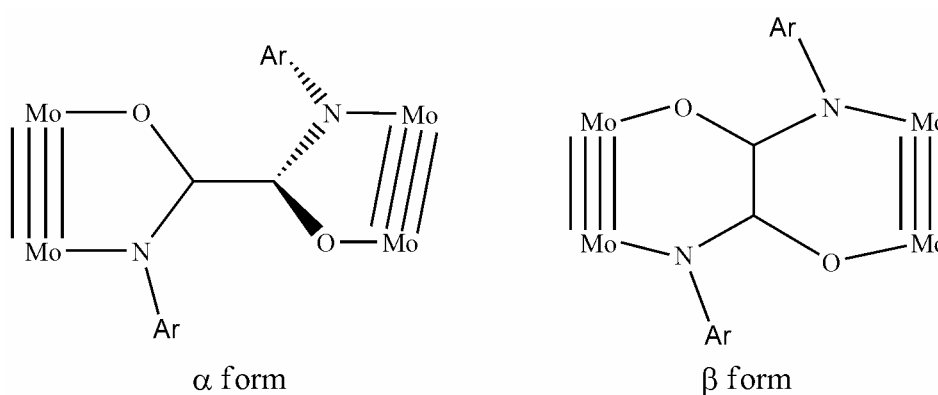
Generally, through the study of these compounds with two dimolybdenum units linked by a variety of polydentate ligands (L), formulated as $[Mo_2]L[Mo_2]$ ($[Mo_2]$ = $[Mo_2(DAniF)_3]^+$), it has been established that efficient metal (δ) – ligand (π*) orbital interaction is critical to promote strong electronic communication through the linker L.

For the type of tetranulcear clusters, numerous cyclic Mo_4 compounds consisting of two triply– or quadruply–bonded dimetal units joined by four single–atom bridging ligands have been reported. Three important types (**I**, **II** and **III)** are shown in Scheme 6 below.[7]

Scheme 6

I   II

III

The bridging groups, X, used in such molecules have been of considerable variety. In compounds of type **I**, two quadruple bonds have undergone [2 + 2] cycloaddition to form a metallocyclobutadiyne ring by cleaving the δ bonds and then forming two σ bonds between the two dimolybdenum pairs.[21] For example, in the tetrachloro–bridged compound $Mo_4Cl_4(PEt_3)_4$, the short (ca. 2.21 Å) and long edges (2.90 Å) of the Mo_4 rectangle correspond to Mo≡Mo triple bonds and Mo–Mo single bonds, respectively.[22] When the separation between the two dimetal units is large, the loss of δ bonding to give two new single bonds does not occur, and a molecule of type **II** is obtained. An example of this type occurs when X = I. Compounds of type **III** differ from those of types **I** and **II** in that they have two Mo_2^{4+} units supported by two, three–atom bridging ligands, typically *N,N′*–di–*p*–anisylformamidinate (DAniF) in *cis* positions. These compounds, described by the general formula $[Mo_2(cis–DAniF)_2]_2(\mu–X_4)$, have been reported for X = Cl, Br and I.[23] Their structural characterization revealed that such molecules, even the chloride, retain their quadruple bonds with Mo–Mo distances of 2.12 Å and the

non–bonded separations between the two Mo_2 units range from 3.6 to 3.9 Å, depending on the atomic radius of the bridging atom. For compounds of this type, cycloaddition does not occur, even though the core is similar and the bridging ligands are the same as those in group **I**, e. g., Cl^-.

It has been noted that the two Mo_2 units in the halide–bridged compounds of type **III** are strongly coupled, although there is no bond between them. For example, $[Mo_2(cis–DAniF)_2]_2(\mu–Cl_4)$ has a large $\Delta E_{1/2}$ value of 540 mV, which corresponds to a comproportionation constant of 1.3×10^9. Because of the large comproportionation constant, oxidation of the neutral precursor gives a mixed–valence complex with the unpaired electron delocalized over all four Mo atoms.[23] It should be noted that the metal to ligand back bonding mechanism proposed for $[Mo_2]L[Mo_2]$ compounds may not applicable to the halide system. Because of the very short metal to metal separation, direct head to head interaction between the two δ orbitals (shown in Scheme 7) is the more likely cause of the strong coupling.

Scheme 7
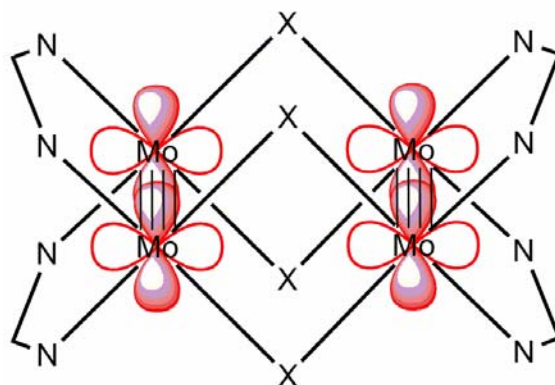
This dissertation is divided into seven chapters. In Chapter II, several new polyamidate–linked dimolybdenum compounds are reported and the electronic communication is discussed. After the study of amidate ligand by changing half of the O donor atoms to N, the natural next step is to try to use a linker with all–N–donor atoms. In Chapter III, the fluoflavinate anion (the dianion of 5,11–dihydroquinoxalino[2,3–b]quinoxaline, $C_{14}H_8N_4^{2-}$) is used to link two [Mo$_2$] subunits. This is the only all–nitrogen donor–linker that has so far been used to bind two dimetal centers. In contrast to all other dimolybdenum systems studied thus far that show a maximum of two redox waves, the [Mo$_2$](fluoflavinate)[Mo$_2$] compound show three reversible one–electron redox processes. Because of the "non–innocent" redox nature of the fluoflavinate linker, interesting questions are raised concerning the appearance of the three rather than only two redox processes. In Chapter IV, unsubstituted oxamidate and dithiooxamidate were used to bridge two dimolybdenum units in a way different form α or β forms. Changing O atoms from oxamidate to S lowers the barrier energy for the metal–to–ligand charge transfer pathway and the electronic coupling between the dimetal centers was greatly enhanced.

Chapters V and VI describe the study of the electronic communication in the tetranuclear Mo$_4$ clusters. In Chapter V, [Mo$_2$(cis–DAniF)$_2$]$^{2+}$, units are linked by alkoxides. The non–bonding separation between the midpoints of the quadruply bonded units, ca. 3.25 Å, is the shortest among compounds having two linked Mo$_2^{4+}$ units. Electrochemical measurements show two redox waves for each compound with large $\Delta E_{1/2}$ values that correspond to K_C values on the order of 10^9. The large electronic

communication is attributed to the short separation between dinuclear units that favor direct δ to δ orbital interactions between the two dimetal centers. Study on the oxidized species show that a transformation from a neutral compound with no bonding interaction between the two Mo_2 units to a doubly oxidized compound that has a bonding interaction between the two dimolybdenum units was observed. Chapter VI describes the utilization of two bidentate ligands to bring two $[Mo_2]$ together. By doing this, extra constrains are added to the structural motif, which have an effect in increasing the thermodynamic stability of these compounds. The sulfur donor ligand, o–$S_2C_6H_4$, has been used for the first time to build a Mo_4 cluster, and this compound shows exceptionally large potential separation ($\Delta E_{1/2}$ = 776 mV), while for the oxygen bridged analogue this value is only 560 mV, even though the former has a $Mo_2\cdots Mo_2$ distance of 3.724 Å, considerably larger than 3.267Å for the latter. DFT calculations show that the enhancement in electronic communication between the metal centers in the S–bridge compound is due to the existence of a super–exchange pathway that is less important for the O–analogue.

All of these compounds have been characterized by X–ray crystallography, elemental analysis, UV–vis and, as appropriate, by various techniques such as NMR, EPR, NIR and magnetic measurements. General characterization and calculation details will be given in the experimental section the first time they are used in this dissertation.

CHAPTER II

MOLECULAR PAIRS AND A PROPELLER CONTAINING QUADRUPLY
BONDED DIMOLYBDENUM UNITS LINKED BY POLYAMIDATE LIGANDS[*]

INTRODUCTION

In our laboratory, polycarboxylate linkers have been employed to assemble covalently bonded dimetal units such as $[Mo_2(DAniF)_n]^{4-n}$ (DAniF = *N,N'*–di–*p*–anisylformamidinate) to produce Mo_2–containing architectures, and electronic communication between the dimetal centers are investigated.[15] Compared to dicarboxylate anions, isoelectronic diamidate groups have drawn much less attention as linkers for supramolecular arrays. However, the amidate ligands possess attractive properties absent in the parent carboxylate species. Because amidate groups are much stronger Lewis bases than the corresponding carboxylate groups, it is anticipated that the resulting complexes would be thermodynamically more stable than the corresponding carboxylate. Furthermore, for amidate ligands the R substituents on the N atoms, are synthetically adjustable in both steric and electronic properties, and therefore can modify the molecular structure and tune the electronic properties of the complexes.

It should also be noted that the large difference in acid and base properties between

dicarboxylate and diamidate groups affects the reactivity towards metal ions. While carboxylate anions can be readily prepared and are easily handled, deprotonation of the amide ligands requires use of strong bases, and produces very basic and reactive anions that may complicate further reaction with certain starting materials. For example, the dimolybdenum complex $[Mo_2(DAniF)_3(NCCH_3)_2]^+$, an excellent starting material for the preparation of dicarboxylate–linked Mo_2 pairs, cannot be used for the syntheses of diamidate analogues because there is nucleophilic attack by the diamidate anion on one of the coordinated acetonitrile molecules.[18] This difficulty can be overcome by use of the mixed–ligand compound $Mo_2(DAniF)_3(O_2CH_3)$ as starting material.

Here we report several new polyamidate–linked dimolybdenum compounds, prepared in good yield and high purity by direct assembly of $Mo_2(DAniF)_3(O_2CCH_3)$ with polyamides in the presence of strong base (H^-) (Figure 3). There are two molecular pairs with phthaloyldiamidate linkers, $[Mo_2(DAniF)_3]_2\{1,4–C_6H_4[C(O)NEt]_2\}$ (**1**) and $[Mo_2(DAniF)_3]_2\{1,3–C_6H_4[C(O)NPh]_2\}$ (**2**), and a molecular propeller having three dimolybdenum units linked by a triamidate ligand, $[Mo_2(DAniF)_3]_3\{1,3,5–C_6H_3[C(O)NPh]_3\}$ (**3**). To examine the electronic coupling interactions in the pairs, a compound with two Mo_2^{5+} units, $\{[Mo_2(DAniF)_3]_2[1,4–C_6H_4[C(O)NEt]_2]\}(BF_4)_2$ (**4**), has been prepared by oxidation of **1**. There is only weak electronic communication as revealed by electrochemical measurements of the precursor **1**, and magnetic studies of **4** that show that one unpaired electron localized on each of the $[Mo_2]$ units.
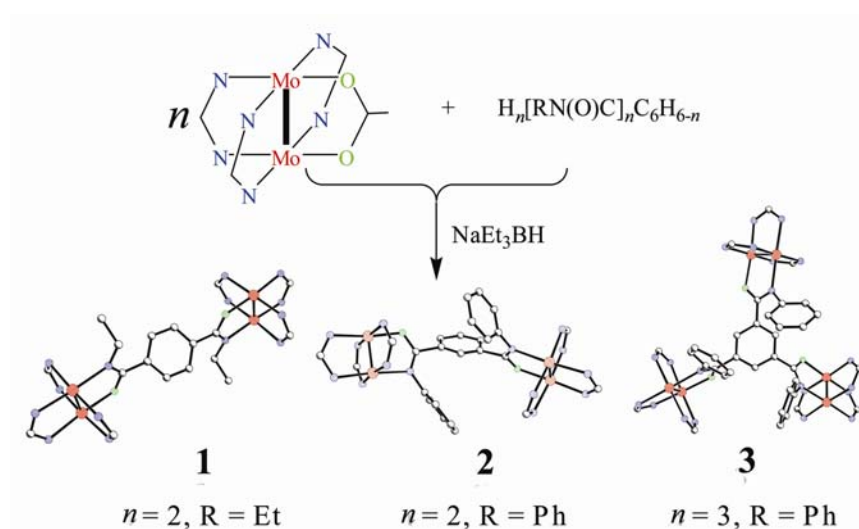
Figure 3. Reaction diagrams for the polyamidate–linked dimolybdenum compounds.

EXPERIMENTAL SECTION

Materials and Methods. All manipulations were performed under a nitrogen atmosphere, using either a drybox or standard Schlenk line techniques. Solvents were purified under argon using a Glass Contour solvent purification system or distilled over appropriate drying agents under nitrogen. The starting material $Mo_2(DAniF)_3(O_2CCH_3)$ was synthesized following a reported procedure,[19] and commercially available chemicals were used as received. The polyamide linkers were conveniently prepared by reaction of the polycarboxylic chlorides with the corresponding amines.

Physical Measurements. Elemental analyses were performed by Robertson Microlit Laboratories, Madison, New Jersey. Electronic spectra were measured at room temperature on a Shimadzu UV–2501PC spectrometer in CH_2Cl_2 solution. ^{1}H NMR spectra were recorded on a Inova–300 or Mercury NMR spectrometer with chemical shifts (δ ppm) referenced to $CDCl_3$. Cyclic voltammogram and differential pulse

voltammogram were collected on a BAS 100 electrochemical analyzer with Pt working and auxiliary electrodes, Ag/AgCl reference electrode, scan rate (for CV) of 100 mV/s, and 0.10 M Bu_4NPF_6 (in CH_2Cl_2) as electrolyte. The EPR spectrum was recorded on a Bruker ESP300 spectrometer and Magnetic susceptibility measurements were performed on a Quantum Design SQUID MPMS–XL magnetometer.

Preparation of [Mo$_2$(DAniF)$_3$]$_2$[N,N'–diethylterephthamidate], 1. To a solution of $Mo_2(DAniF)_3(O_2CCH_3)$ (610 mg, 0.600 mmol) and N,N'–diethylterephthamide (66 mg, 0.30 mmol) in 30 mL of THF was added with stirring 0.60 mL of a 1.0 M solution of $NaBEt_3H$ in THF. The color of the mixture changed from yellow to brown. The reaction mixture was stirred at room temperature for 6 h and then the solvent was removed under vacuum. The remaining solid was extracted with 3 × 5 mL of dichloromethane and filtered through a filter frit packed with Celite. The volume of the filtrate was reduced to about 2 mL under vacuum, and then 50 mL of ethanol was added, producing a yellow solid and a brown supernatant solution. After the solution was decanted, the solid was washed with ethanol (2 × 15 mL) followed by hexanes (2 × 15 mL) and then dried under vacuum. The crude product was dissolved in 15 mL of dichloromethane and layered with hexanes. An orange–yellow crystalline solid formed within 2 days. The solid was collected by filtration and briefly placed under vacuum. Yield: 0.525 g (82%). ^{1}H NMR (δ, ppm in CDCl$_3$): 8.46 (s, 4H, –NCHN–), 8.42 (s, 2H, –NCHN–), 7.57 (s, 4H, aromatic C–H in linker), 6.62 (d, 4H, aromatic H), 6.57 (m, 24H, aromatic H), 6.38 (m, 16H, aromatic H), 6.14 (d, 4H, aromatic H), 3.71 (s, 6H, –OCH_3), 3.70 (s, 12H, –OCH_3), 3.67 (s, 12H, –OCH_3), 3.61 (s, 6H, –OCH_3), 3.42 (q, 4H, CH_2),

0.25 (t, 6H, CH_3). UV–vis, λ_{max} (nm) (ε, M^{-1}cm^{-1}): 442 (3.2 × 10^3). Anal. Calcd for

C$_{105.5}$H$_{111}$Cl$_6$N$_{14}$O$_{14}$Mo$_4$ (**1**·3.5CH$_2$Cl$_2$): C, 52.01; H, 4.56; N, 8.05. Found: C, 51.79; H,

4.86; N, 8.18.

Preparation of [Mo$_2$(DAniF)$_3$]$_2$\{1,3–C$_6$H$_4$[C(O)NPh]$_2$\}, 2. This yellow compound

was made similarly to **1**. Yield: 340 mg (76%). ^{1}H NMR (δ, ppm in CDCl$_3$): 8.56(s, 4H,

–NCHN–), 8.38(s, 2H, –NCHN–), 7.67 (s, 1H, aromatic C–H in linker), 7.01 (t, 1H,

aromatic C–H in linker), 6.71 (d, 2H, aromatic H), 6.68 (m, 8H, aromatic H), 6.64 (d,

12H, aromatic H), 6.60 (d, 2H, aromatic H), 6.49 (d, 8H, aromatic H), 6.42 (m, 8H,

aromatic H), 6.32 (m, 4H, aromatic H), 6.20 (d, 4H, aromatic H), 6.12 (d, 4H, aromatic

H), 5.96 (d, 8H, aromatic H), 3.72 (s, 12H, –OCH_3), 3.69 (s, 12H, –OCH_3), 3.68 (s, 6H,

–OCH_3), 3.67 (s, 6H, –OCH_3). UV–vis, λ_{max} nm (ε, M^{-1}mol^{-1}): 436 (3.0 × 10^3). Anal.

Calcd for **2**·2.5CH$_2$Cl$_2$ (C$_{112.5}$H$_{109}$Cl$_5$Mo$_4$N$_{14}$O$_{14}$): C, 55.33; H, 4.50; N, 8.03. Found: C,

55.22; H, 4.69; N, 8.16.

Preparation of [Mo$_2$(DAniF)$_3$]$_3$\{C$_6$H$_3$[C(O)NPh]$_3$\}, 3. To a mixture of

Mo$_2$(DAniF)$_3$(O$_2$CCH$_3$) (610 mg, 0.600 mmol) and 1,3,5–benzenetricarboxanilide (87.2

mg, 0.200 mmol) was added 30 mL of THF producing a yellow solution. With stirring,

1.8 mL of a 1.0 M solution of NaEt$_3$BH in THF was then added to the yellow solution

which quickly turned brown. Following a crystallization procedure similar to that for **1**,

orange crystals were obtained. Yield: 0.458 g (69.3%). ^{1}H NMR (δ, ppm in CDCl$_3$): 8.57

(s, 6H, –NCHN–), 8.32 (s, 3H, –NCHN–), 7.49 (s, 3H, aromatic C–H), 6.69 (d, 12H,

aromatic H), 6.56 (m, 24H, aromatic H), 6.43 (d, 12H, aromatic H), 6.36 (m, 12H,

aromatic H), 6.26 (m, 6H, aromatic H), 6.16 (d, 6H, aromatic H), 6.01 (d, 6H, aromatic

H), 5.87 (d, 12H, aromatic *H*), 3.71 (s, 18H, –OC*H*$_3$), 3.65 (s, 9H, –OC*H*$_3$), 3.64 (s, 9H,

–OC*H*$_3$), 3.60 (s, 18H, –OC*H*$_3$). UV–vis, λ_{max} (nm) (ε, M^{-1}cm^{-1}): 447 (9.4 $\times$ 10^3). Anal.

Calcd for **4**·3.5CH$_2$Cl$_2$ (C$_{165.5}$H$_{160}$N$_{21}$O$_{21}$Mo$_6$): C, 55.16; H, 4.44; N, 8.17. Found: C,

54.85; H, 4.66; N, 8.18.

Preparation of {[Mo$_2$(DAniF)$_3$]$_2$[C$_2$H$_5$N(O)CC$_6$H$_4$C(O)NC$_2$H$_5$](BF$_4$)$_2$, 4.
Solutions of **1** (106 mg, 0.050 mmol) in 10 mL of CH$_2$Cl$_2$ and ferrocenium

tetrafluoroborate (30 mg, 0.11 mmol) in 10 mL of CH$_2$Cl$_2$ were prepared separately and

cooled to −78 °C. The solution of Cp$_2$FeBF$_4$ was transferred to the solution of **1**, the

color changed immediately from yellow–orange to dark brown. The mixture was stirred

at low temperature for 30 min, and then an isomeric mixture containing 40 mL of

pre–cooled hexanes was added to precipitate a brown solid. A yellow supernatant

solution was decanted, and the remaining solid was washed with cooled hexanes (2 × 15

mL) and dried under vacuum. The dry solid was dissolved in 15 mL of dichloromethane

in a Schlenk tube, and the solution was layered with hexanes. The Schlenk tube was kept

in a freezer at −50 °C. Very dark (almost black) crystals formed within 2 weeks. Yield:

86 mg (75%). UV–vis, λ_{max} nm (ε, M^{-1}mol^{-1}): 458 (3.3 $\times$ 10^3). Anal. Calcd. for

4·CH$_2$Cl$_2$ (C$_{103}$H$_{106}$B$_2$Cl$_2$F$_8$Mo$_4$N$_{14}$O$_{14}$): C, 51.33; H, 4.52; N, 8.14. Found: C, 51.22; H,

4.32; N, 7.99.

X–ray Structure Determinations. Single crystals suitable for X–ray diffraction

analysis of all compounds were obtained by diffusion of hexanes into a CH$_2$Cl$_2$ solution

of corresponding product. Each crystal was mounted and centered in the goniometer of a

Bruker SMART 1000 CCD area detector diffractometer and cooled to −60 °C. Cell

parameters were determined using the program SMART.[24] Data reduction and integration were performed with the software package SAINT,[25] and absorption corrections were applied using the program SADABS.[26] In all structures, the positions of the heavy atoms were found via direct methods using the program SHELXTL.[27] Subsequent cycles of least–square refinement followed by difference Fourier syntheses revealed the positions of the remaining non–hydrogen atoms. Hydrogen atoms were added in idealized positions. Non–hydrogen atoms were refined with anisotropic displacement parameters. Some of the anisyl group in the DAniF ligands and interstitial CH_2Cl_2 molecules were found disordered, and they were refined with soft constraints.

RESULTS AND DISCUSSION

Syntheses. Compounds **1** and **2** were synthesized by mixing the dimolybdenum starting material $Mo_2(DAniF)_3(O_2CCH_3)$ with the corresponding diamides in the presence of the strong base $NaEt_3BH$. Use the mixed–ligand compound $Mo_2(DAniF)_3(O_2CCH_3)$ instead of $[Mo_2(DAniF)_3(NCCH_3)_2]^+$ to introduce the dimetal building blocks, precludes nucleophilic attacks of basic ligands onto coordinated acetonitrile molecules.[28] This procedure also requires only short reaction times and produces significantly higher yields than those reported for the first dimolybdenum pairs linked by diamidate groups which were prepared by reaction of $Mo_2(DAniF)_3Cl_2$ with Zn in the presence of the linker.[28]

The molecular propeller **3** was synthesized similarly to **1** and **2** but a longer reaction time and an excess of base were required to ensure the addition of an $[Mo_2]$ unit to each

of the three amidate groups of the linker. It should be noted that a carboxylate analogue

using the anion of trimesic acid, $[Mo_2(DAniF)_3]_3[(1,3,5-C_6H_3)(CO_2)_3$, was previously

synthesized by using a different and tedious method.[29]   The synthesis of **3** also required

a modification of the procedure developed earlier for the syntheses of pairs linked by

oxamidates in which sodium methoxide reacts first with $Mo_2(DAniF)_3(O_2CCH_3)$ and

then with the linker, a procedure that can also be used for the syntheses of **1** and **2**. The

preparative methodology for the three neutral compounds can be generally described by

the general reaction:

$$n Mo_2(DAniF)_3(O_2CCH_3) \quad + \quad H_n[RN(O)C]_nC_6H_{6-n} \quad + \quad nH^- \quad \rightarrow$$

$$[Mo_2(DAniF)_3]_n[RN(O)C]_nC_6H_{6-n} + nH_2 \; (R = Ph \; or \; Et)$$
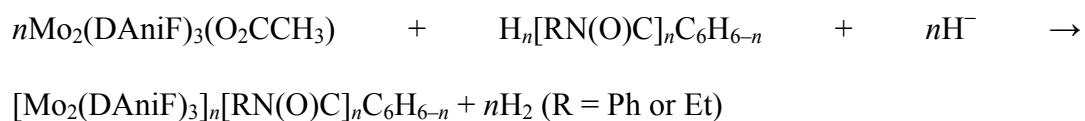
However, when $NaOCH_3$ was used in an attempt to prepare **3**, an incomplete

reaction was observed. From a reaction using $NaOCH_3$ as the base, crystals of a

compound with only two dimolybdenum units were isolated. It should also be noted that

a synthesis employing sodium methoxide reported earlier and the one reported here

using $NaEt_3BH$ appear to be mechanistically different. When sodium methoxide is used,

the reagent reacts with the dimolybdenum starting material upon mixing to form

$Mo_2(DAniF)_3(OCH_3)(CH_3OH)$. This highly reactive species then reacts with the diamide

to form the target molecule. On the other hand, the $NaEt_3BH$ base appears to be strong

enough to directly attack and deprotonate the polyamides.

The ionic compound **4** was obtained by reaction at low temperature of the neutral compound **1** using two equivalents of ferrocenium tetrafluoroborate as the oxidizing agent. Attempts to isolate the singly oxidized product by using only one equivalent of the ferrocenium salt were unsuccessful. Failure to generate the monocation of **1** may be ascribed to the low thermodynamic stability of the mixed–valence complex as indicated by the small comproportionation constant Kc (27) derived from $\Delta E_{1/2}$ (85 mV), as shown below.

Solid State and Solution Structures. Crystallographic data for **1**·3CH₂Cl₂, **3**·4CH₂Cl₂ and **4**·4CH₂Cl₂ are given in Table 1, and selected bond distances in Table 2. Compound **1** crystallized in space group $P\bar{1}$ with $Z = 1$, which requires the molecule to reside on an inversion center. As shown in Figure 4, the core consists of two essentially parallel dimolybdenum units linked by the terephthaloyldiamidate ligand. This structure is closely related to those in compounds with a diarylterephthaloyldiamidate linker. The Mo−Mo bond distance, 2.090(1) Å (Table 2), is characteristic for a quadruply bonded dimolybdenum unit supported by four three–atom bridging groups. The separation between the midpoints of the metal–metal bonds is 11.4 Å. The bridging p–phenylene group shows appreciable deviation (48.3°) from the plane defined by the two Mo₂ units.

Figure 4. Core structure of **1** with displacement ellipsoids drawn at the 40% probability level. All *p*–anisyl groups and hydrogen atoms have been omitted for clarity.

Table 1. X–ray Crystallographic Data for **1**, **3** and **4**.

	1·2.2CH$_2$Cl$_2$	**3**·4CH$_2$Cl$_2$	**4**·4CH$_2$Cl$_2$
empirical formula	C$_{104.2}$H$_{108.4}$Cl$_{4.4}$Mo$_4$N$_{14}$O$_{14}$	C$_{166}$H$_{161}$Cl$_8$Mo$_6$N$_{21}$O$_{19}$	C$_{106}$H$_{112}$B$_2$Cl$_8$F$_8$Mo$_4$N$_{14}$O$_{14}$
Fw	2320.59	3613.4	2647.08
space group	$P\bar{1}$ (No. 2)	$P\bar{1}$ (No. 2)	$P\bar{1}$ (No. 2)
a, Å	9.7891(9)	18.707(2)	13.694(2)
b, Å	14.024(1)	21.027(2)	14.231(2)
c, Å	20.359(1)	22.939(2)	17.720(3)
A, deg	96.806(2)	109.850(2)	106.745(2)
B, deg	99.006(2)	91.064(2)	93.660(3)
Γ, deg	106.116(2)	98.470(2)	117.810(2)
V, Å^3	2613.1(4)	8372(2)	2843.7(7)
Z	1	2	1
T, K	213	213	213
Λ, Å	0.71073	0.71073	0.71073
d$_{calcd}$, g/cm^3	1.475	1.433	1.546
M, mm^{-1}	0.65	0.632	0.699
R1^a (wR2^b)	0.0797(0.1566)	0.1090(0.2319)	0.0659(0.1347)

[a] R1 = Σ||F_o|–|F_c||/ Σ|F_o|. [b] wR2 = [Σ[$w(F_o^2–F_c^2)^2$]/Σ[$w(F_o^2)^2$]]$^{1/2}$

Table 2. Selected Bond Lengths (Å) and Angles (º) for **1**, **3** and **4**.

	1·2.2CH$_2$Cl$_2$	**3**·4CH$_2$Cl$_2$	**4**·4CH$_2$Cl$_2$
Mo(1)–Mo(2)	2.090(1)	2.091(2)	2.1237(6)
Mo(3)–Mo(4)		2.092(1)	
Mo(5)–Mo(6)		2.091(1)	
Mo(1)–O(1)	2.112(4)		2.082(3)
Mo(2)–O(1)		2.120(7)	
Mo(1)–N(2)	2.147(5)	2.162(9)	2.129(4)
Mo(1)–N(4)	2.162(5)	2.163(10)	2.093(4)
Mo(1)–N(6)	2.153(5)	2.176(10)	2.123(4)
Mo(1)–N(1)		2.187(9)	
Mo(2)–N(1)	2.177(5)		2.169(4)
Mo(2)–N(3)	2.172(5)	2.166(10)	2.104(4)
Mo(2)–N(5)	2.142(5)	2.136(10)	2.147(3)
Mo(2)–N(7)	2.190(5)	2.143(10)	2.135(4)

Complex **2**, where the linker is 1,3–diphenylterephthaloyldiamidate is an isomer of a compound reported earlier having the 1,4–diphenylterephthaloyldiamidate linker.[18] Unfortunately, crystals of this complex do not diffract adequately for a full crystallographic characterization, although the identity of the compound is unambiguous. Crystallographic data for $[Mo_2(DAniF)_3]_2\{PhNH(O)CC_6H_4[C(O)NPh]_2\}\cdot2CH_2Cl_2$: space group $P\bar{1}$, $a = 10.561(2)$ Å, $b = 18.427(3)$ Å, $c = 33.767(6)$ Å, $\alpha = 81.092(3)°$, $\beta = 89.433(3)°$, $\gamma = 75.063(3)°$, $V = 6270(2)$ Å^3, $Z = 2$. The Mo–Mo distances are 2.093(3) and 2.092(3) Å.

The ^{1}H NMR spectra of both **1** and **2** show that the compounds are diamagnetic as expected for species containing quadruply bonded Mo_2^{4+} units. The spectra are also consistent with the molecules maintaining in solution the structures from their crystals. For example, the two signals for the methine protons appear as singlets in a ratio of 4:2, while there are four singlets for the methoxy groups of the anisyl groups that appear in a ratio of 12:12:6:6. Transitions in the electronic spectra at 442 and 436 nm for **1** and **2**, respectively, correspond to those found for the $\delta \rightarrow \delta*$ transition in similar species with Mo–Mo quadruple bonds. For **3**, the ^{1}H NMR spectrum is again consistent with the presence of a symmetrical species with two singlets in a ratio of 2:1 (6:3) for the methine protons. The ratio of 1:18 (3:54) for the central C_6H_3 unit (7.49 ppm) in the linker to the total methoxy groups of the anisyl groups in the DAniF ligand is consistent with the presence of three Mo_2^{4+} unit for each linker. This corresponds with the X–ray structure that shows three $Mo_2(DAniF)_3$ units attached to a triamidate ligand giving the molecule a propeller–shape as shown in Figure 5. Because this compound crystallized in the space

group $P\bar{1}$ with $Z = 2$, the two enantiomers are related by an inversion center. The three crystallographically independent Mo−Mo bonds are essentially equivalent and typical of quadruply bonded species (2.091(2) Å, 2.092(2) Å and 2.091(1) Å) in a similar coordination environment. The midpoints of the three Mo−Mo bonds define an essentially equilateral triangle with edges of 9.79 Å. The Mo−Mo axes are not in the same plane as the central aryl group of the linker, nor are they perpendicular to it but all three [Mo$_2$] units are tilted in the same direction. So also are the three phenyl groups on the nitrogen atoms of the linker, which reside on the same side of the plane of the central aryl group, and the molecule possesses idealized C_3 symmetry. The overall structure of **3** resembles that of the carboxylate analogue [Mo$_2$(DAniF)$_3$]$_3$\{1,3,5−C$_6$H$_3$(CO$_2$)$_3$\}, with the important difference that the additional three phenyl groups in **3** create a cavity or pocket, as shown in Figure 5(b).

Oxidation of **1** produces **4**. As shown in Figure 6, the overall cores of **1** and **4** are similar, with only one notable change in the structural parameters upon oxidation. The Mo−Mo distances are lengthened from 2.090(1) Å in **1** to 2.1237(6) Å in **4**, a change of 0.0337 Å that is caused by removing one electron from the δ orbital of a quadruply bonded Mo$_2^{4+}$ unit, thus lowering the bond order from 4.0 to 3.5.[30] The distance between linked [Mo$_2$] units, 11.3 Å, does not change relative to that in the neutral precursor, implying that the electrostatic interaction between the two positively charged Mo$_2^{5+}$ units is weak. In the dication in **4** the torsion angle between the central benzene group and the plane containing the two Mo−Mo (55°) is about 7° larger than that in **1**.

(a)
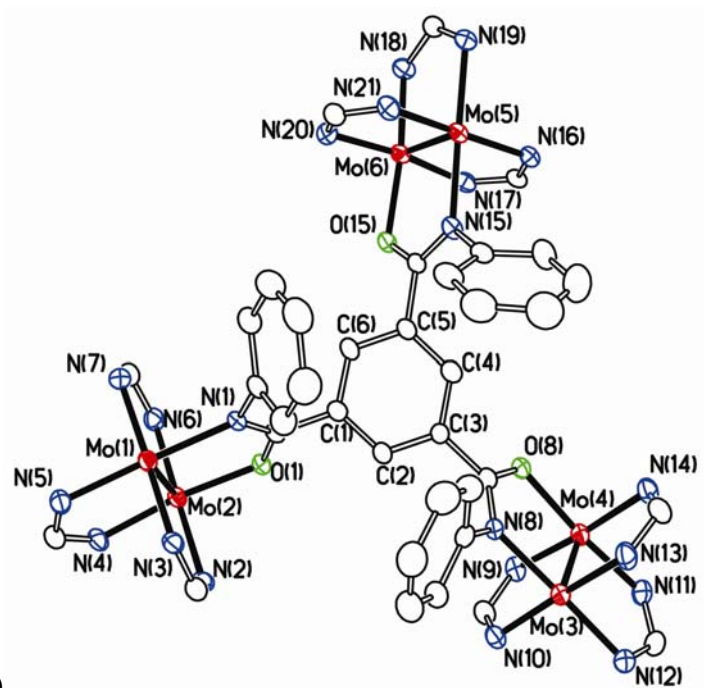
(b)
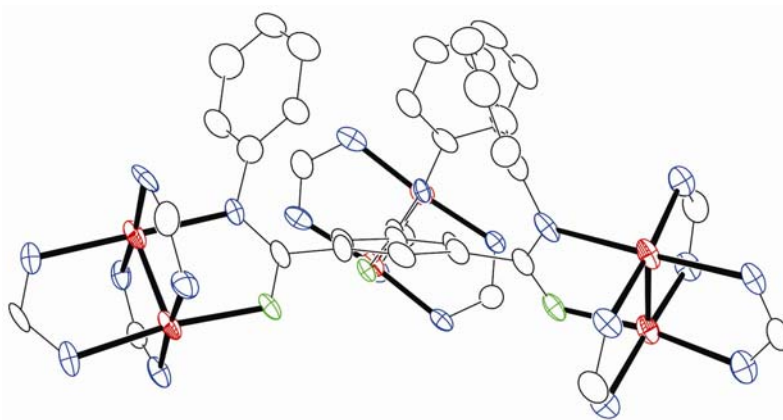
Figure 5. (a) Core of **3** with displacement ellipsoids drawn at the 40% probability level. (b) A side view of the core of the molecular propeller **3**. All *p*–anisyl groups and hydrogen atoms have been omitted for clarity.
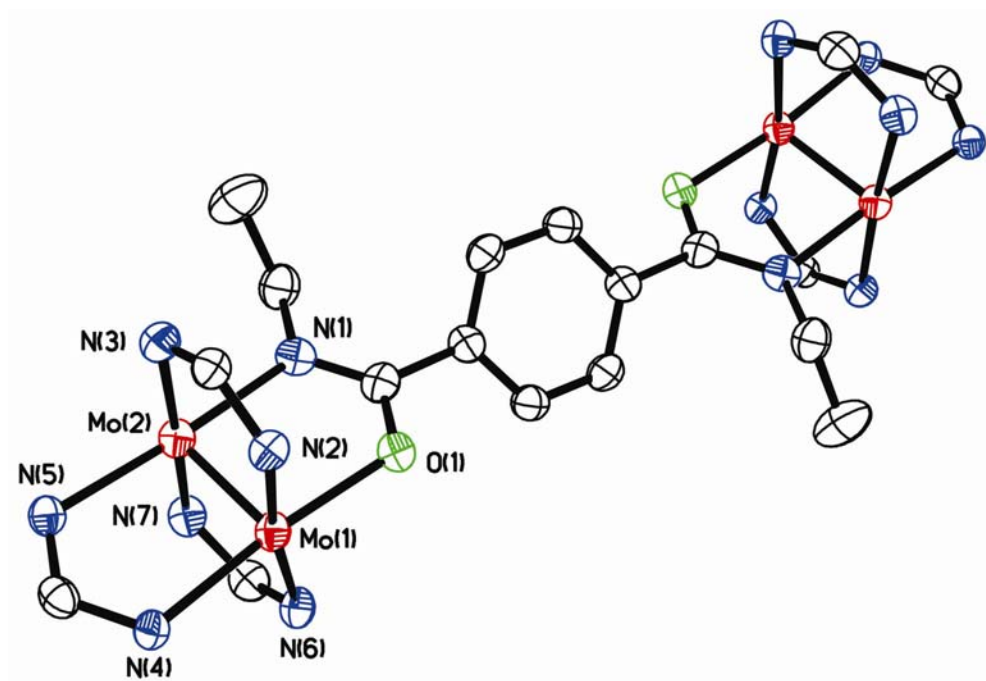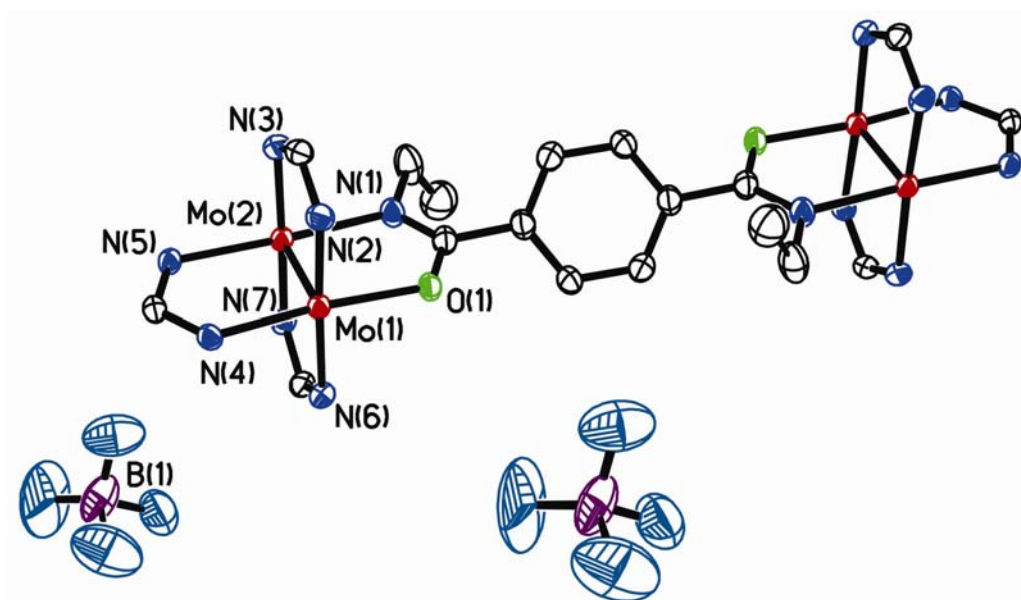
Figure 6. Core structure of **4** with displacement ellipsoids drawn at the 40% probability level. All *p*–anisyl groups and hydrogen atoms have been omitted for clarity.

Electrochemistry. The cyclic voltammograms (CV) and differential pulse voltammograms (DPV) for **1**–**3** are shown in Figure 7. The small $\Delta E_{1/2}$ values for the pairs (85 mV for **1** and 105 mV for **2**) indicate that the electronic coupling between the two dimetal centers is weak.

In general, the main contributions to electronic coupling between two linked metal centers are electrostatic interactions and electron delocalization.[31] While the former depends heavily on the length of the linker, the later depends greatly on orbital interactions of the metal units and the linker. Because the two [Mo$_2$] units are separated by about 11 Å in **1**, weak electronic interactions might be expected. Additionally, since the central aryl group from the linker is not co–planar with the Mo–Mo vectors, and there is a torsion angle of 48°, the possibility of δ–π conjugation is significantly diminished. Therefore, one [Mo$_2$] unit hardly "senses" the presence of the other unit. This contrasts with the strong electronic communication in the β–form of the *N,N'*–dimethyloxamidate linked compound, where the [Mo$_2$]···[Mo$_2$] separation is only 6.25 Å and there is good δ–π conjugation that leads to the formation of a heteronaphthalene stucture.[20] For **2** the $\Delta E_{1/2}$ of 105 mV is slightly larger than that of **1** because of the shorter [Mo$_2$]···[Mo$_2$] separation (about 10 Å) relative to that in **1**. For the molecular propeller **3**, the redox waves for the three one–electron oxidations strongly overlap, indicating that the three dimolybdenum centers are weakly coupled, and in this respect it resembles the tricarboxylate analogue.
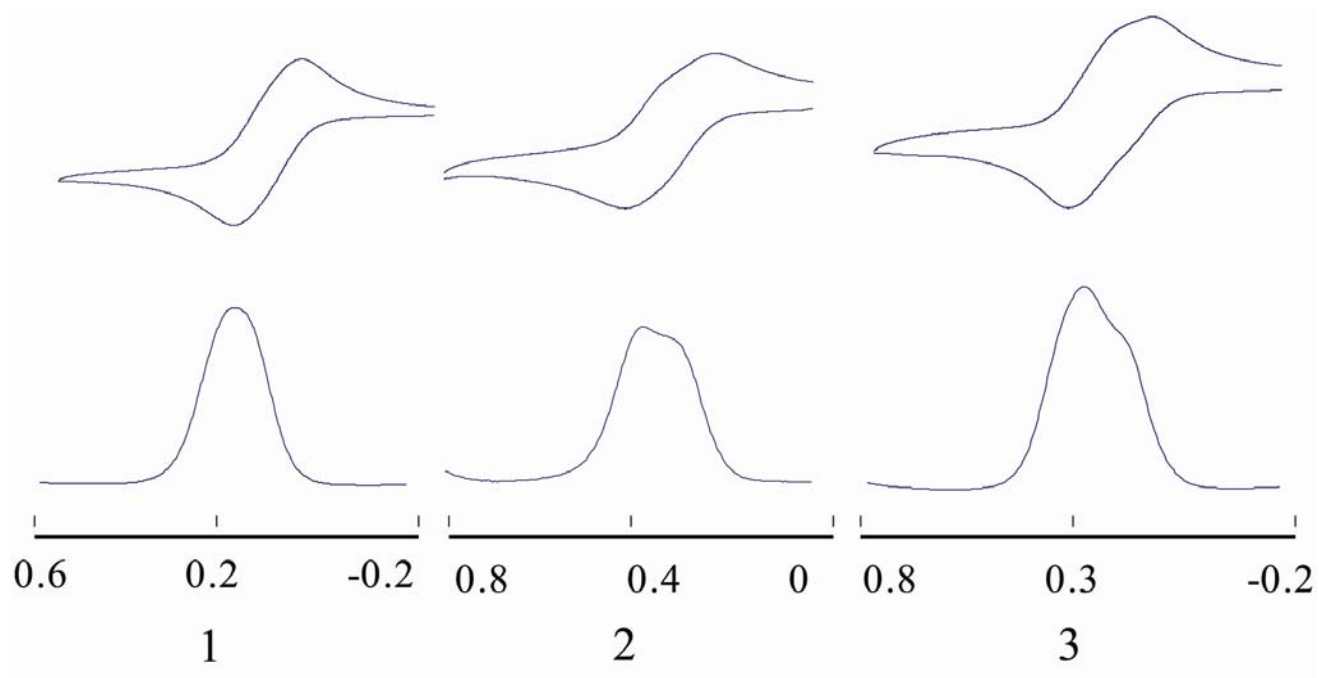
Figure 7. Cyclic voltammograms (with potentials in volts vs Ag/AgCl) and differential pulse voltammograms (DPV) for **1**, **2** and **3** in CH$_2$Cl$_2$ solution.

Magnetism of 4. Compound **4** is paramagnetic and its X–band EPR spectrum was measured at room temperature in CH_2Cl_2 solution. The spectrum, top image in Figure 8, shows a prominent symmetric peak at g = 1.94 that corresponds to the metal based unit (^{96}Mo (I = 0)). The smaller peaks on the both sides of the strong signal are the hyperfine structure from the ^{95,97}Mo (I =5/2) isotopes.[32,33] A simulation of the spectrum with one odd electron residing on each of the two Mo_2 units and using the parameters g = 1.94 and A = 22 × 10^{-4} cm^{-1} shows satisfactory agreement with the experimental data. These magnetic parameters are very similar to those in the parent paddlewheel cation $[Mo_2(DAniF)_4]^{+}$.[34] Previous work has also shown that hyperfine coupling constant for $[Mo_2]$ linked compounds provide reliable information on the nature of the electronic interactions. For example, small hyperfine coupling constants are characteristic of highly delocalized systems, e. g., 11.5 × 10^{-4} cm^{-1} for $\{[Mo_2(DAniF)_3](\mu–H)_2[Mo_2(DAniF)_3]\}^{+}$ and 12.2 × 10^{-4} cm^{-1} for the oxidized species of $\{[Mo_2(DAniF)_3](C_6H_4O_2)[Mo_2(DAniF)_3]\}$,[35] while larger hyperfine coupling constants are typical in localized systems, e. g., A$_{\parallel}$ of 37.7 G and A$_{\perp}$ of 15.6 G were observed for the compounds $\{[Mo_2(DAniF)_3]_2M(OCH_3)_4^{+}$ (M = Zn and Co).[11] Similar results were also observed by Chisholm and co–workers in their work on dimolybdenum pairs linked by oxalate (A = 14.8 G) and perfluoroterephthalate (A = 27.2 G). [14]

The variable–temperature magnetic measurements of **4** show a χT (emu K mol^{-1}) of 0.75 at 300 K, a value corresponding to two non–interacting unpaired electrons (g = 2.0 and S = 1/2). The χT value decreases very slowly with the lowering of temperature, but much rapidly below 20 K. This sharper decrease, which extrapolates to χT = 0 at 0 K

is indicative of either weak antiferromagnetic interactions or weak intramolecular interactions. Therefore, the doubly oxidized **4** is an electron–trapped species with one unpaired electron residing on each of the two Mo_2^{5+} units as suggested also by electrochemical measurements.
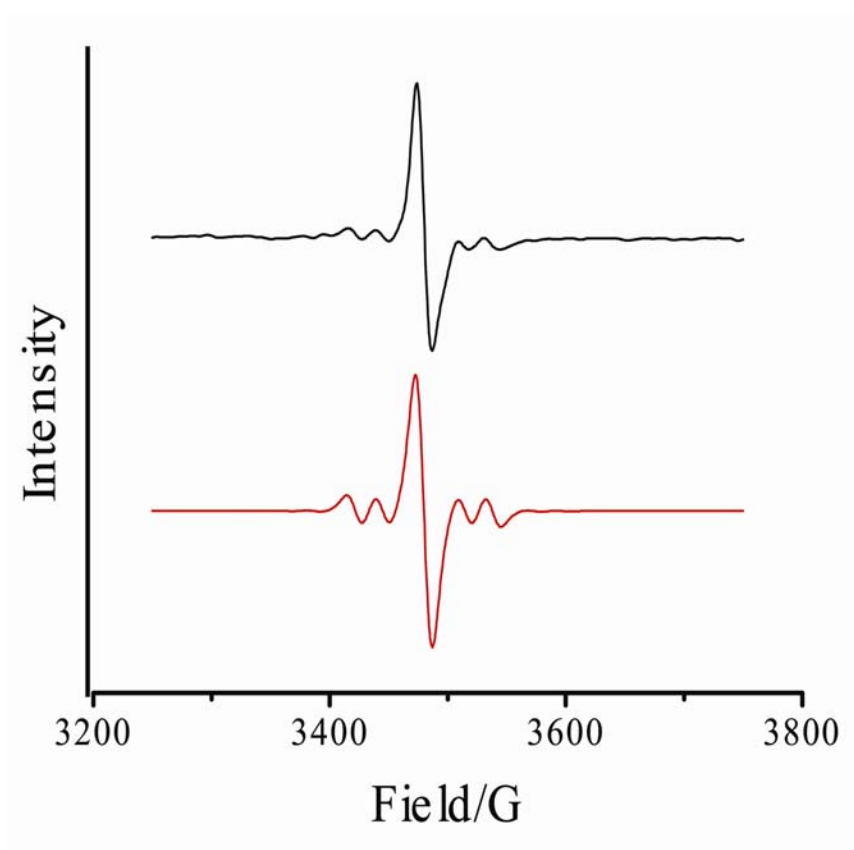
Figure 8. X–band EPR spectrum of **4** in CH_2Cl_2 solution at room temperature (top). The simulated spectrum is shown in red at the bottom.

CHAPTER III

STRONG ELECTRONIC INTERACTION BETWEEN TWO DIMOLYBDENUM UNITS LINKED BY A TETRAAZATERACENE[*]

INTRODUCTION

Dicarboxylate anions ($O_2C-X-CO_2^{2-}$) were the first ligands used as linkers between metal–metal bonded [Mo_2] units. In our efforts to gain insight into the factors that lower the energy barrier and increase the electron transfer rate, we have replaced half of the O–donor atoms by N to diamidates. The idea for the next step is to utilize all–N–donor bridges.

In this chapter, the fluoflavinate anion (the dianion of 5,11–dihydroquinoxalino[2,3–b]quinoxaline, $C_{14}H_8N_4^{2-}$, Scheme 8) is used to link two [Mo_2] subunits. This linker features unusual structural, electronic and chemical properties, attributable to the rigidity of a large planar aromatic π system that extends throughout the four fused six–membered rings. This is the only all–nitrogen donor–linker that has so far been used to bind two dimetal centers. It should be noted that as the number of oxygen donor atoms diminishes by changing from dicarboxylate to fluoflavinate via diamidate groups, the basicity of the linkers significantly increases.

In contrast to all other dimolybdenum systems studied thus far that show a maximum of two redox waves, the [Mo$_2$](fluoflavinate)[Mo$_2$] compound shows three reversible one–electron redox couples. Because of the "non–innocent" redox nature of the fluoflavinate linker, interesting questions are raised concerning the appearance of the three rather than only two redox processes. To aid in the interpretation, three members of an electron–transfer series have been synthesized. These are the neutral compound, [Mo$_2$(DAniF)$_3$]$_2$(C$_{14}$H$_8$N$_4$) (**5**), the mixed–valence ion, {[Mo$_2$(DAniF)$_3$]$_2$(C$_{14}$H$_8$N$_4$)}$^+$ in two crystalline forms (**6a** or **6b**), and the doubly oxidized cation, {Mo$_2$(DAniF)$_3$}$_2$(C$_{14}$H$_8$N$_4$)}$^{2+}$ (**7**). Two additional compounds are also reported. One contains only one dimolybdenum unit with a monoanionic fluoflavinate ligand, [Mo$_2$(DAniF)$_3$](HC$_{14}$H$_8$N$_4$) (**8**). The other one, **9**, is similar to **5** but it has *trans*–Mo$_2$(DAniF)$_2$(O$_2$CCH$_3$) units instead of Mo$_2$(DAniF)$_3$. All compounds have been characterized using various techniques, including X–ray structure analyses, electrochemical measurements, spectroscopic and magnetic studies that suggest that the MV species are electronically delocalized in the time scale of the experimental measurements. This conclusion is supported by DFT calculation.

Scheme 8
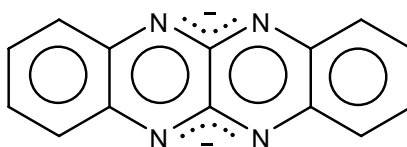
fluoflavinate

EXPERIMENTAL SECTION

Materials and Methods. The starting materials, fluoflavine, and its 2–methyl derivative (5,12–dihydro–2–methylquinoxalino[2,3–*b*]quinoxaline) were prepared following reported procedures.[36]

Physical Measurements. The near–IR spectrum was measured on a Bruker TEASOR 27 spectrometer using a KBr pellet. Magnetic susceptibility measurements were performed on a Quantum Design SQUID MPMS–XL magnetometer, and the EPR spectra were recorded using a Bruker ESP300 spectrometer.

Computational Details. Density functional theory (DFT)[37] calculations were performed with three different functionals. The hybrid functionals B3LYP[38] and mPW1PW91[39] and the gradient–corrected BP86[40] were used as implemented in the Gaussian 03 (Revision C.02) program suite.[41] Double–ζ quality basis sets (D95)[42] were used on carbon, nitrogen, and hydrogen atoms. A small effective core potential (ECP) by Hay and Wadt, representing the 1s2s2p3s3p3d core was used for the molybdenum atoms, along with its corresponding double–ζ basis set (LANL2DZ).[43] TD–DFT[44] calculations were performed to ascertain the identity of the lowest energy transitions in the UV–vis and NIR regions for **5** and **6**. All calculations were performed on either an Origin 3800 64–processor SGI, an Origin 2000 32–processor SGI computers, located at the Texas A&M supercomputing facility, or an Origin 300 8–processor SGI, located at the Department of Chemistry at Texas A&M University.

Preparation of [Mo$_2$(DAniF)$_3$]$_2$(C$_{14}$H$_8$N$_4$), 5. To a mixture of Mo$_2$(DAniF)$_3$(O$_2$CCH$_3$) (812 mg, 0.800 mmol) and fluoflavine (94 mg, 0.40 mmol) in 40 mL of THF was added slowly, and with stirring, 2 mL of a 0.5 M solution of NaOCH$_3$ in methanol. The yellow color turned to orange and then to dark brown. The reaction mixture was stirred overnight at ambient temperature. The solvent was removed under reduced pressure, and the residue was extracted with 15 mL of dichloromethane. After filtration, the volume of the solution was reduced under vacuum to ca. 5 mL. Ethanol (50 mL) was stirred into the solution, whereupon an orange precipitate formed. The supernatant solution was decanted, and the solid was washed with ethanol (2 × 15 mL) followed by hexanes (2 × 15 mL). The solid was dissolved in 15 mL of dichloromethane and the solution was layered with hexanes. Orange needle crystals formed in 5 days. Yield: 580 mg (68%). ^{1}H NMR (δ, ppm in CDCl$_3$): 8.65(s, 2H, –NC*H*N–), 8.323 (s, 4H, –NC*H*N–), 6.62 (d, 8H, aromatic C–*H*), 6.54 (d, 16H, aromatic C–*H*), 6.50 (d, 16H, aromatic C–*H*), 6.27 (d, 8H, aromatic C–*H*), 5.69 (m, 4H, fluoflavinate C–*H*), 3.78 (s, 12H, –C*H*$_3$), 3.69 (s, 24H, –C*H*$_3$), 3.52 (m, 4H, fluoflavinate C–*H*). UV–vis, λ_{max} nm (ε, M^{-1} mol^{-1}): 412 (2.4 × 10^3), 432 (3.0 × 10^2), 460 (8.0 × 10^2), 482 (2.0 × 10^2), 512 (1.0 × 10^3). Anal. Calcd. for C$_{104}$H$_{98}$Mo$_4$N$_{16}$O$_{12}$: C, 58.15; H, 4.57; N, 10.43. Found: C, 58.53; H, 4.67; N, 10.38.

Preparation of {[Mo$_2$(DAniF)$_3$]$_2$(C$_{14}$H$_8$N$_4$)}PF$_6$, 6a. Solutions of **5** (215 mg, 0.100 mmol in 10 mL of CH$_2$Cl$_2$) and ferrocenium hexafluorophosphate (36 mg, 0.11 mmol in 10 mL of CH$_2$Cl$_2$) were prepared separately and cooled to −78 °C. The solution of Cp$_2$FePF$_6$ was transferred to the solution of **5**, and the mixture turned dark brown

immediately. The mixture was allowed to warm to room temperature with stirring over the course of 1 h. Then 40 mL of hexanes was added to precipitate a very dark brown solid. After the yellow supernatant solution was decanted, the solid was washed with hexanes (2 × 15 mL) and dried under vacuum. The dry solid was dissolved in 15 mL of dichloromethane and the solution was layered with hexanes. Large block–crystals formed in 3 days. Yield: 190 mg (83.0%). UV–vis, λ_{max} nm (ε, M^{-1} mol^{-1}): 420 (2.2 × 10^3), 454 (3.0 × 10^2), 550 (2.0 × 10^3), 622 (3.0 × 10^2). Anal. Calcd. for $C_{104}H_{98}PF_6Mo_4N_{16}O_{12}$: C, 54.50; H, 4.28; N, 9.77. Found: C, 54.83; H, 4.12; N, 9.89.

Preparation of {[Mo₂(DAniF)₃]₂(C₁₄H₈N₄)}SO₃CF₃, 6b. Solutions of **5** (107 mg, 0.050 mmol in 10 mL of CH_2Cl_2) and $AgSO_3CF_3$ (13 mg, 0.050 mmol in 10 mL of CH_2Cl_2) were prepared separately and cooled to −78 °C. The solution of $AgSO_3CF_3$ was transferred to the solution of **5**, and the mixture turned very dark brown immediately. The mixture was allowed to warm to ambient temperature with stirring over the course of 1 h and was then filtered through a filter frit packed with Celite. The filtrate was layered with hexanes and black crystals formed in 3 days. Yield: 60 mg (53%). UV–vis, λ_{max} nm (ε, M^{-1} mol^{-1}): 410 (1.0 × 10^2), 436 (1.3 × 10^3), 454 (2.0 × 10^2), 550 (1.3 × 10^3), 620 (1.6 × 10^2).

Preparation of {[Mo₂(DAniF)₃]₂(C₁₄H₈N₄)}(PF₆)₂, 7. Solutions of **5** (274 mg, 0.128 mmol in 10 mL of CH_2Cl_2) and $AgPF_6$ (65 mg, 0.26 mmol in 20 mL of CH_2Cl_2) were prepared separately and cooled to −78 °C. The solution of $AgPF_6$ was transferred to the solution of **5** and the color of the mixture became black immediately. The mixture was allowed to warm to room temperature with stirring over the course of 1 h and was

then filtered through a filter frit packed with Celite. The filtrate was layered with hexanes and black crystals formed in 3 days. Yield: 80 mg (33%). Anal. Calcd for $C_{105}H_{100}P_2F_{12}Mo_4N_{16}O_{12}Cl_2$ (**7·CH$_2$Cl$_2$**): C, 49.98; H, 3.97; N, 8.89. Found: C, 49.91; H, 4.26; N, 8.54. UV–vis, λ_{max} nm (ε, M^{-1} mol^{-1}): 434 (1.2×10^3), 462 (3.3×10^2), 548 (4.7×10^2), 636 (1.1×10^2).

Preparation of Mo$_2$(DAniF)$_3$(HC$_{14}$H$_8$N$_4$), 8. To a mixture of Mo$_2$(DAniF)$_3$(O$_2$CCH$_3$) (203 mg, 0.200 mmol) and fluoflavine (55 mg, 0.23 mmol) was added 30 mL of THF, giving a yellow suspension. With stirring, 2 mL of a 0.5 M solution of NaOCH$_3$ in methanol was added slowly, and the reaction mixture was stirred overnight at ambient temperature. After removal of the solvent under reduced pressure, the yellow residue was extracted with 15 mL of dichloromethane and filtered through a Celite–packed frit. To the filtrate, ethanol (ca. 40 mL) was added, yielding a yellow solid. After the supernatant solution was decanted, the solid was washed with 15 mL of hexanes and then, redissolved in 10 mL of dichloromethane. The resulting solution was then layered with 40 mL of hexanes. Orange needle crystals formed in 5 days. Yield: 80 mg (36%). ^{1}H NMR (δ, ppm in CDCl$_3$): 8.60 (s, 1H, –NC*H*N–), 8.20 (s, 2H, –NC*H*N–), 6.70 (d, 2H, fluoflavinate C–*H*), 6.61 (d, 4H, aromatic C–*H*), 6.56 (t, 2H, fluoflavinate C–*H*), 6.45 (s, 16H, aromatic C–*H*), 6.24 (d, 4H, aromatic C–*H*), 6.96 (t, 2H, fluoflavinate C–*H*), 3.74 (s, 6H, –C*H*$_3$), 3.65 (s, 12H, –C*H*$_3$), 3.62 (t, 2H, fluoflavinate C–*H*). UV–vis, λ_{max} nm (ε, M^{-1} mol^{-1}): 410 (2.3×10^3), 451 (1.2×10^3), 512 (6.0×10^2).

Preparation of [*trans*–Mo$_2$(DAniF)$_2$(O$_2$CCH$_3$)]$_2$(C$_{14}$H$_8$N$_4$), 9. A suspension of fluoflavine (47 mg, 0.20 mmol) in 15 mL of THF was cooled to −20 °C and 0.25 mL of

a 1.6 M methyllithium solution in diethyl ether was added. The suspension of lithium fluoflavinate salt that formed upon warming the mixture to room temperature was transferred to a flask containing a solution of *trans*–$Mo_2(DAniF)_2(O_2CCH_3)_2$ (328 mg, 0.400 mmol) in 15 mL of THF. The reaction mixture was stirred overnight and an orange precipitate formed. After the solvent was removed under reduced pressure, 20 mL dichloromethane was added to the orange residue and the resulting solution was filtered. The volume of the filtrate was reduced to about 5 mL under vacuum and 40 mL hexanes were added to precipitate an orange solid. After the solvent was decanted, the solid was washed with ethanol (2 × 15 mL) followed by hexanes (2 × 15 mL), and dried under vacuum. The solid was dissolved in 15 mL of dichloromethane and the solution was then layered with hexanes. Orange crystals formed in 2 days. Yield: 90 mg (26%) ^{1}H NMR (δ, ppm in $CDCl_3$): 8.45 (s, 4H, –NC*H*N–), 6.80 (d, 16H, aromatic C–*H*), 6.66 (d, 16H, aromatic C–*H*), 5.68 (m, 4H, aromatic C–*H*), 3.71 (s, 24H, –C*H*$_3$), 3.62 (m, 4H, aromatic C–*H*), 2.75 (s, 6H, –O_2CC*H*$_3$). UV–vis, λ_{max} nm (ε, M^{-1} mol^{-1}): 412 (2.5 × 10^3), 446 (9.0 × 10^2), 482 (1.0 × 10^2), 514 (2.4 × 10^2). Anal. Calcd for $C_{82}H_{78}Mo_4N_{12}O_{12}Cl_8$ (**9**·$4CH_2Cl_2$): C, 47.06 H, 3.90; N, 8.36. Found: C, 47.01; H, 3.97; N, 8.09.

RESULTS AND DISCUSSION

Synthesis. In prior work, we developed two general procedures for the preparation of the "dimer–of–dimers" type molecules, which may be described by the general formula [$Mo_2(DAniF)_3$]L[$Mo_2(DAniF)_3$], where L represents a linker. The source of dimolybdenum units can be either the [$Mo_2(DAniF)_3(NCCH_3)_4$]$^{2+}$ dication or $Mo_2(DAniF)_3(O_2CCH_3)$, the choice of which depends on the basicity of the linker. For example, when the linker is a strong Lewis base which may nucleophilically attack the coordinated acetonitrile molecules, $Mo_2(DAniF)_3(O_2CCH_3)$ is the appropriate starting material. For the very weak acid fluoflavine ($H_2C_{14}H_8N_4$), the conjugate base ($C_{14}H_8N_4{}^{2-}$) is a strong Lewis base, and therefore, $Mo_2(DAniF)_3(O_2CCH_3)$, rather than [$Mo_2(DAniF)_3(NCCH_3)_4$]$^{2+}$, was used in the synthesis of [$Mo_2(DAniF)_3$]$_2$($C_{14}H_8N_4$). The overall reaction that led to synthesis of **5** is given below:

$$2Mo_2(DAniF)_3(O_2CCH_3) \quad + \quad H_2(C_{14}H_8N_4) \quad + \quad 2NaOCH_3 \quad \rightarrow$$

$$[Mo_2(DAniF)_3]_2(C_{14}H_8N_4) \quad + \quad 2CH_3OH \quad + \quad 2NaO_2CCH_3$$
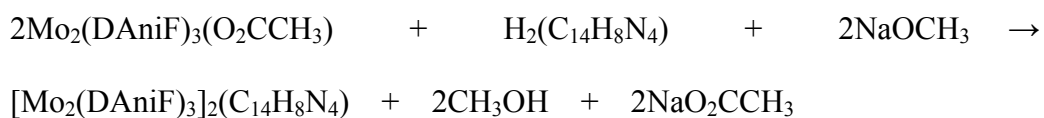
Compound **5** is soluble in common organic solvents, such as tetrahydrofuran and dichloromethane, even though fluoflavine is highly insoluble in these solvents. After routine treatment, the reaction produces crystalline material in useful yield.

Chemical oxidation of **5** was guided by electrochemical data. The cyclic voltammogram (CV) and differential pulse voltammogram (DPV) show three reversible redox waves. This contrasts with all known [Mo_2]L[Mo_2] analogues, such as those with dicarboxylate and diamidate linkers in which only two waves were observed. The three

successive one–electron oxidations occur at potentials of 79, 495, 941 mV (vs. Ag/AgCl). Ferrocenium hexafluorophosphate was chosen to remove one electron from the neutral molecule **5** and the stronger oxidant AgPF$_6$ was used for the synthesis of the doubly oxidized cation. The advantage of using Cp$_2$FePF$_6$ for the preparation of the mono–charged complex is that the reaction gives **6a** in high yield without contamination by the doubly oxidized species, even when the oxidizing reagent is present in excess. However, when silver trifluoromethanesulfonate was used for the preparation of the singly oxidized complex **6b**, it was very important to carefully control the reaction stoichiometry to avoid further oxidation.

The dication in **7** was prepared using AgPF$_6$ as the oxidizing agent. In practice, more than 2 equiv of the oxidizing reagent must be used to obtain a product of acceptable purity for elemental analysis. This compound is not stable in solution at ambient temperature, and even in the solid state there are signs of decomposition after a few hours.

It is clear from the electrochemistry that the third oxidation of **5** would require a very strong oxidizing reagent, and all attempts to isolate such highly charged species have so far been unproductive.

The paddlewheel compound Mo$_2$(DAniF)$_3$(HC$_{14}$H$_8$N$_4$), **8**, was prepared using a modification of the procedure described above for **5**. The strategy used to avoid the possibility of obtaining the dimer–of–dimers was to control the amount of the methoxide base. The ratio of base to Mo$_2$ species was 1:1 to form the intermediate Mo$_2$(DAniF)$_3$(OCH$_3$)(CH$_3$OH) but fluoflavine was used in excess. Because in **8** the free

N−C−N group of the fluoflavinate ligand is protonated, it is capable of binding another [Mo$_2$] unit if additional base were to be added. Such molecules are usually active or unstable and formation of [Mo$_2$]L[Mo$_2$] species may occur even in the absence of strong base. For example, a reaction of dicarboxylic acid with Mo$_2$(DAniF)$_3$(O$_2$CCH$_3$) produces only [Mo$_2$](dicarboxylate])[Mo$_2$] compounds, regardless of the stoichiometry of the reactants added. An amidate analogue of **8** has been isolated but it immediately dimerizes in basic solution. Interestingly, **8** is stable and there is no evidence of dimerization occurring in solution. The unusual stability of **8** may be attributed to the very weak acidity of the fluoflavine ligand.

Compound **9** may be viewed as a derivative of **5** by replacement of one DAniF group on each [Mo$_2$] unit with an acetate anion. It was prepared in a one–pot reaction by mixing *trans*–Mo(DAniF)$_2$(O$_2$CCH$_3$)$_2$ with lithium fluoflavinate. The doubly deprotonated ligand displaces only one acetate group from each of two *trans*–Mo(DAniF)$_2$(O$_2$CCH$_3$)$_2$ molecules, giving **9**. It is plausible that since the precursor *trans*–Mo(DAniF)$_2$(O$_2$CCH$_3$)$_2$ has two labile acetate groups t*rans* to each other, there is also a possibility of obtaining a polymer with alternating bridging ligands and dimolybdenum units, but so far we have not been able to isolate such a compound. We are also investigating the possibility of coupling **8** and **9** in a ratio of 2:1 with the idea of creating a tetrad of dimolybdenum units.

Structural Results. Crystallographic data for **5**·4CH$_2$Cl$_2$, **6b**·7.5CH$_2$Cl$_2$, **7**·4CH$_2$Cl$_2$, **8** and **9**·4CH$_2$Cl$_2$ are in Table 3, and selected bond distances are in Table 4. Compound **5** crystallized in space group $P\bar{1}$ with the molecule residing on an inversion

Table 3. X–ray Crystallographic Data for **5**, **6b**, **7**, **8** and **9**.

	5·4CH$_2$Cl$_2$	**6b**·7.5CH$_2$Cl$_2$	**7**·4CH$_2$Cl$_2$	**8**	**9**·4CH$_2$Cl$_2$
empirical formula	C$_{108}$H$_{106}$Cl$_8$Mo$_4$N$_{16}$O$_{12}$	C$_{112.5}$H$_{113}$Cl$_{15}$F$_3$Mo$_4$N$_{16}$O$_{15}$S	C$_{108}$H$_{106}$C$_{18}$F$_{12}$Mo$_4$N$_{16}$O$_{12}$P$_2$	C$_{59}$H$_{54}$Mo$_2$N$_{10}$O$_6$	C$_{82}$H$_{82}$Cl$_8$Mo$_4$N$_{12}$O$_{12}$
Fw	2487.45	2933.76	2777.39	1191	2094.96
Space group	$P\bar{1}$ (No. 2)	$P2_1/n$ (No. 14)	$P\bar{1}$ (No. 2)	$P2_1/c$ (No.14)	$P\bar{1}$ (No. 2)
a, Å	12.3728(8)	17.881(5)	12.336(1)	14.6700(9)	10.533(2)
b, Å	15.864(1)	23.811(6)	16.948(2)	17.894(1)	14.862(3)
c, Å	15.948(1)	29.914(8)	17.203(2)	20.725(1)	15.070(3)
α, deg	60.320(1)	90	60.865(2)	90	89.761(4)
β, deg	89.858(1)	93.715(5)	81.414(2)	95.358(1)	73.296(4)
γ, deg	84.897(1)	90	70.215(2)	90	75.536(4)
V, Å^3	2705.9(3)	12710(6)	2955.7(6)	5416.9(6)	2182.0(9)
Z	1	4	1	4	1
T, K	213	213	213	213	213
λ, Å	0.71073	0.71073	0.71073	0.71073	0.71073
d$_{calcd}$, g/cm^3	1.526	1.533	1.56	1.46	1.594
μ, mm^{-1}	0.718	0.787	0.706	0.525	0.873
R1[a] (wR2[b])	0.0463(0.1043)	0.0937(0.1786)	0.0626(0.1069)	0.0426(0.0888)	0.0922(0.1653)

[a] R1 = $\Sigma||F_o|-|F_c||/\Sigma|F_o|$. [b] wR2 = $[\Sigma[w(F_o^2-F_c^2)^2]/\Sigma[w(F_o^2)^2]]^{1/2}$

Table 4. Selected Bond Lengths (Å) for **5**, **6b**, **7**, **8** and **9**

	5·4CH$_2$Cl$_2$	**6b**·7.5CH$_2$Cl$_2$	**7**·4CH$_2$Cl$_2$	**8**	**9**·4CH$_2$Cl$_2$
Mo(1)–Mo(2)	2.0939(4)	2.1084(8)	2.1245(5)	2.0931(3)	2.0818(8)
Mo(3)–Mo(4)		2.1108(8)			
Mo(1)–N(1)	2.156(3)	2.132(5)	2.143(3)	2.171(2)	2.137(5)
Mo(1)–N(3)	2.161(3)	2.132(5)	2.144(3)	2.155(2)	2.141(5)
Mo(1)–N(5)	2.162(3)	2.150(5)	2.128(3)	2.149(2)	
Mo(1)–O(5)					2.132(4)
Mo(1)–N(7)	2.160(3)	2.150(5)	2.111(3)	2.154(2)	2.146(5)
Mo(2)–N(2)	2.169(3)	2.129(5)	2.117(3)	2.144(2)	2.133(5)
Mo(2)–N(4)	2.150(3)	2.144(5)	2.109(3)	2.152(2)	2.138(5)
Mo(2)–N(6)	2.161(3)	2.135(5)	2.117(3)	2.160(2)	
Mo(2)–O(6)					2.139(5)
Mo(2)–N(8)	2.135(3)	2.129(5)	2.137(3)	2.159(2)	2.164(5)
Mo(3)–N(9)		2.128(5)			
Mo(3)–N(11)		2.148(5)			
Mo(3)–N(13)		2.137(5)			
Mo(3)–N(15)		2.136(5)			
Mo(4)–N(10)		2.122(5)			
Mo(4)–N(12)		2.142(5)			
Mo(4)–N(14)		2.154(5)			
Mo(4)–N(16)		2.132(5)			

center. The core, depicted in Figure 9, shows that the two dimolybdenum units, each supported by three DAniF ligands, are linked by a fluoflavinate anion. The two Mo−Mo bonds are co–planar with the fluoflavinate anion and the molecule possesses idealized D_{2h} symmetry. While in compounds of this type with other linkers, conformational variation occurs (for example, for dicarboxylate–linked complexes, a rotation about a C−C single bond[45] is observed and in the β–diamidate–linked compounds, the dimetal–linker chelate ring is twisted.[19]), the molecules in **5** are conformationally rigid. This unique structural feature has an important impact on electronic communication between the two [Mo$_2$] units. The neutral molecule **5** has a typical quadruple bond length, 2.0939(4) Å, for the two crystallographically equivalent dimolybdenum units. The two [Mo$_2$] units are separated by 7.174 Å, which is slightly greater than 6.95 Å found in the oxalate analogue.

As shown by the ^{1}H NMR spectrum, the structure of **5** remains unchanged in solution. All the signals for the supporting DAniF ligands are divided into two sets in a ratio of 2:1 for the ligands that are *cis* and *trans* to the fluoflavinate bridge. An example is that of the signals for the methine protons which appear at 8.33 and 8.65 ppm in a ratio of 2:1 in CDCl$_3$. The signals for the fluoflavinate anion appear at 5.69 and 3.52 ppm and show a significant upfield shift from the range (6–7.5) in which aromatic proton signals usually occur. This shift is caused by the high magnetic anisotropy of the dimolybdenum quadruple bond.[46] Since the protons on the fluoflavinate anion are located in the shielding cones of the magnetic anisotropy, the signals are displaced

Figure 9. Core structure of **5** with displacement ellipsoids drawn at the 40% probability level. All *p*–anisyl groups and hydrogen atoms have been omitted for clarity.

toward high field. It should also be noted that the downfield shift of the methine proton signals can also be attributed to the anisotropy of the Mo−Mo quadruple bond. The change in the direction of the shift is due to the location of each group relative to that of the Mo_2^{4+} unit.

The structures of two singly oxidized compounds have been determined. In **6a**, the counter anion is the symmetrical PF_6^- group. The cation in **6a** resides on a special position of monoclinic space group $C2/m$, and the two $[Mo_2]$ units are crystallographically equivalent. Crystallographic data for **6a**•4CH$_2$Cl$_2$: space group $C2/m$; $a = 18.432(3)$, $b = 23.183 (4)$, $c = 17.4429(3)$, $\beta = 121.227 (3)$, $V = 6368.8(1)$, $Z = 2$, Mo−Mo distance $=2.113(3)$ Å. Because these crystals show considerable crystallographic disorder, crystals of the cation with the unsymmetrical trifluoromethanesulfonate (triflate) anion were also prepared and this structure refined smoothly. The cation of **6b** (Figure 10) occupies a general position in the monoclinic space group $P2_1/n$ where the two Mo$_2$ units are crystallographically independent. The Mo−Mo bond distances for the two $[Mo_2]$ units, 2.1084(8) Å and 2.1108(8) Å, are essentially the same, and they are longer than those in the precursor **5** by 0.015Å but significantly shorter than those found in compounds with similar coordination environment having units where the Mo_2^{5+} is localized on only one dimolybdenum unit. The similarity of the crystallographically independent Mo−Mo distances supports a symmetrical electronic structure where the unpaired electron is delocalized over both Mo$_2$ units via the bridging fluoflavinate anion.
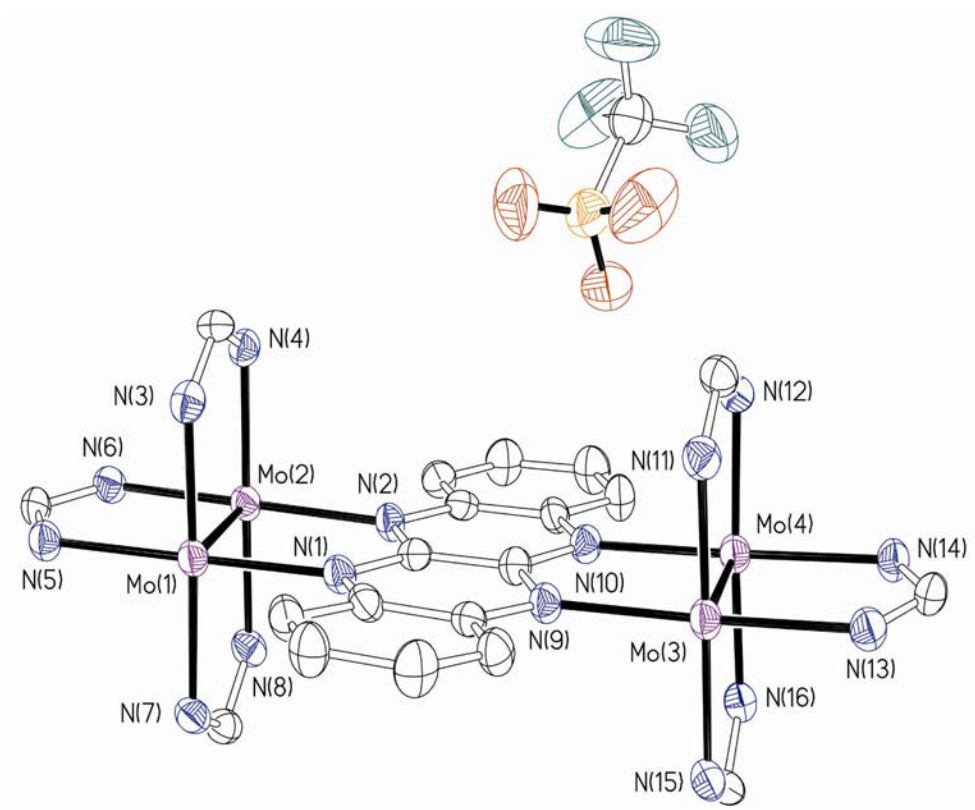
Figure 10. Core structure of **6b** with displacement ellipsoids drawn at the 40% probability level. All *p*–anisyl groups and hydrogen atoms have been omitted for clarity.

The doubly oxidized compound **7** crystallized in triclinic space group $P\bar{1}$ with $Z = 1$. The dication (Figure 11) resides on an inversion center while the PF_6^- ions reside on general positions. Removal of two electrons from **5** to give **7** increases the Mo−Mo distances from 2.0939(4) to 2.1245(5) Å. The increase of 0.030 Å, is twice as large as that observed for the one–electron oxidation product **6b**. The magnitude of the change is also compatible with that observed in the β–oxamidate–linked analogues, where the lengthening of the Mo−Mo bond resulting from double oxidation is 0.04 Å.

Even though the oxidation states for the Mo atoms in **5**, **6(a** and **b)** and **7** are different, the core structures of the three complexes are essentially the same. However, for the three compounds of the electron–transfer series, the average $Mo-N_{DAniF}$ distances are shortened from 2.155 to 2.141 to 2.124 Å as the charge increases on the dimetal units from 0 to 1 to 2. The variation of these metal–ligand distances as well as the changes in the metal–metal distances provides strong evidence that the first two of the three one–electron oxidation processes that appear on the CV correspond to metal–based oxidations.

Compound **8** crystallizes in monoclinic space group $P2_1/c$ with $Z = 4$. The core structure, shown in Figure 12, consists of a quadruply bonded dimolybdenum unit bridged by three DAniF groups and a monoanionic fluoflavinate anion. The metal−metal bond distance, 2.0931(3) Å, is similar to those in **5**. The molecule has idealized C_{2v} symmetry. This symmetry does not change in solution as shown by its ^1H NMR spectrum. There are four groups of signals of the same intensity assigned to fluoflavinate
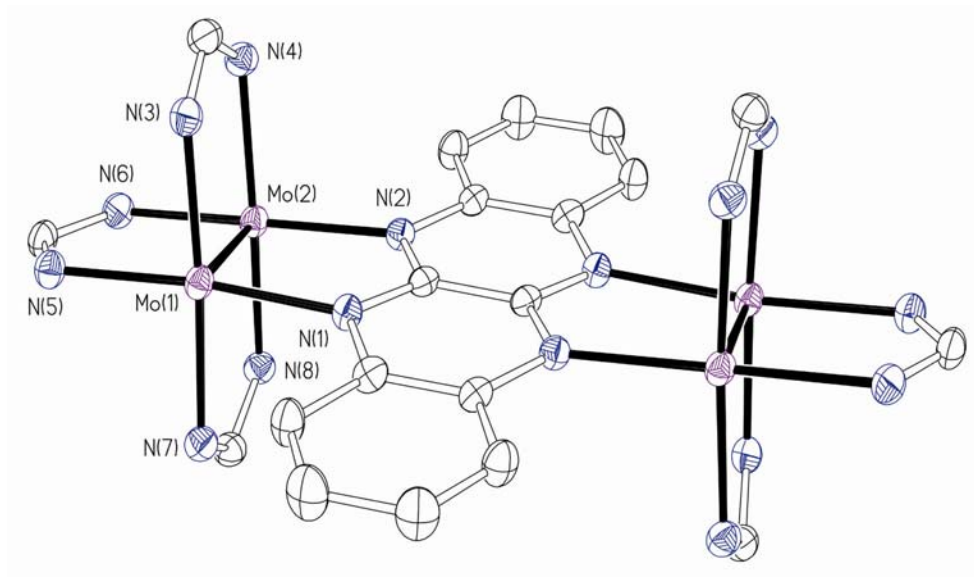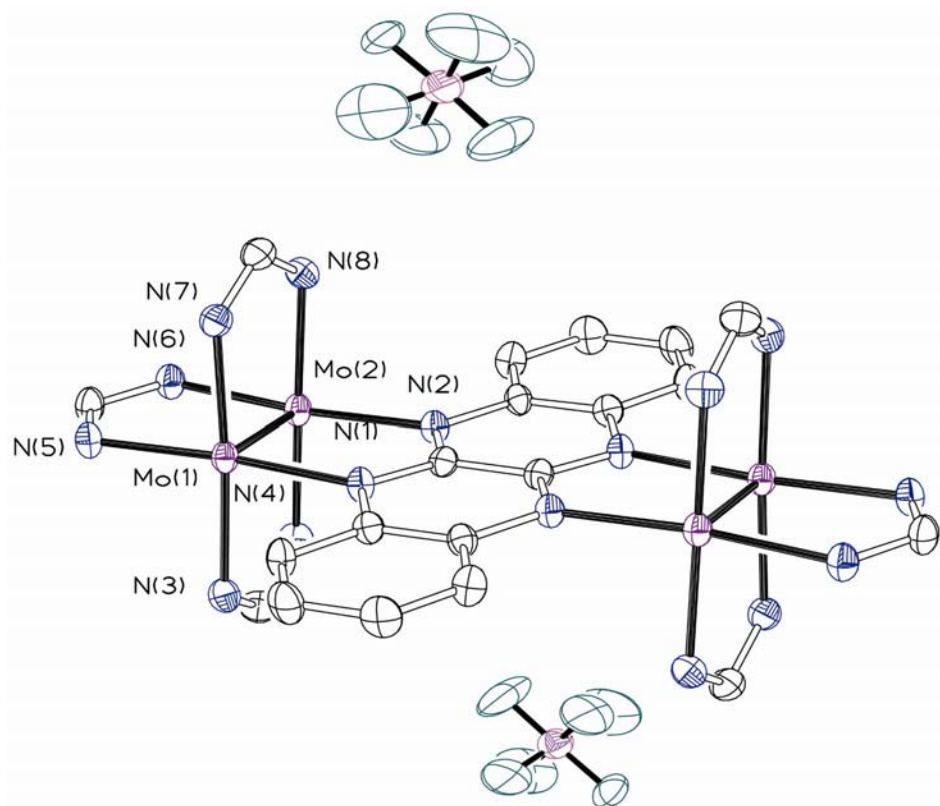
Figure 11. Core structure of **7** with displacement ellipsoids drawn at the 40% probability

level. All *p*–anisyl groups and hydrogen atoms have been omitted for clarity.
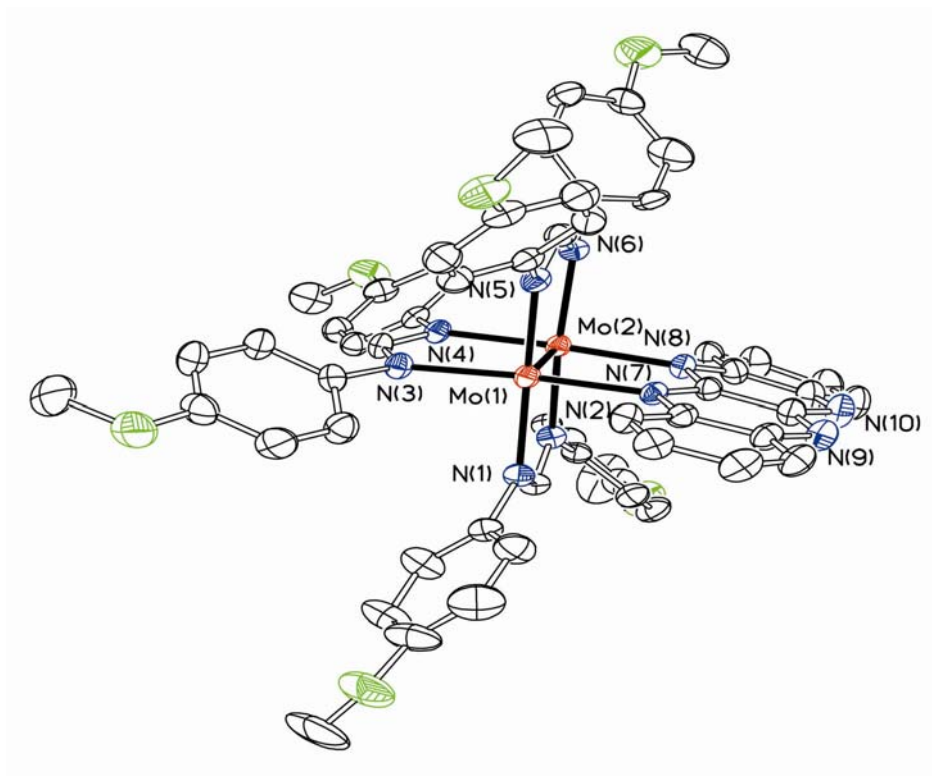
Figure 12. Core of **8** displacement ellipsoids drawn at the 40% probability level.

protons. The signals are scattered in a wide range from 6.56 to 3.62 ppm because of the variable influences of the magnetic anisotropy of the Mo−Mo quadruple bond.

The core structure of **9** is shown in Figure 13 and the structural parameters in Table 4. This compound has the same fluoflavinate linker as **5,** but has slightly different metal subunits. Each dimolybdenum unit is supported by two DAniF units *cis* to the fluoflavinate and an acetate group that is *trans*. The molecule crystallizes in the space group of $P\bar{1}$ with $Z = 1$. The bond distances are very similar to those of **5**. In the ^{1}H NMR spectrum of **9**, signals from the fluoflavinate protons are shifted to high field just as they are in **5**, because of the anisotropy of the Mo_2 quadruple bond. With a labile acetate group on each end, compound **9** has the potential to be used to construct an equatorially linked dimolybdenum chain spaced by conjugated fluoflavinate groups.

Electrochemistry. The prominent electrochemical feature for **5** is the existence of three reversible one–electron waves (Figure 14). Compound **9** also shows three reversible redox couples at 199, 619 and 1004 mV (Table 5). As mentioned earlier, structural data support the assignment of the first two waves as being metal–based oxidations but it offers no clues for the assignment of the third one, at the highest potential. Since no compound could be isolated from our attempts to prepare a triply oxidized species, the electrochemistry of the paddlewheel compound $Mo_2(DAniF)_3(HC_{14}H_8N)$, **8**, was studied. Compound **8** shows two reversible one–electron oxidation processes at 390 and 795 mV. These potentials are much lower than those in **5**. The appearance of two redox processes is rather unusual in dimolybdenum systems and very few examples are known where this
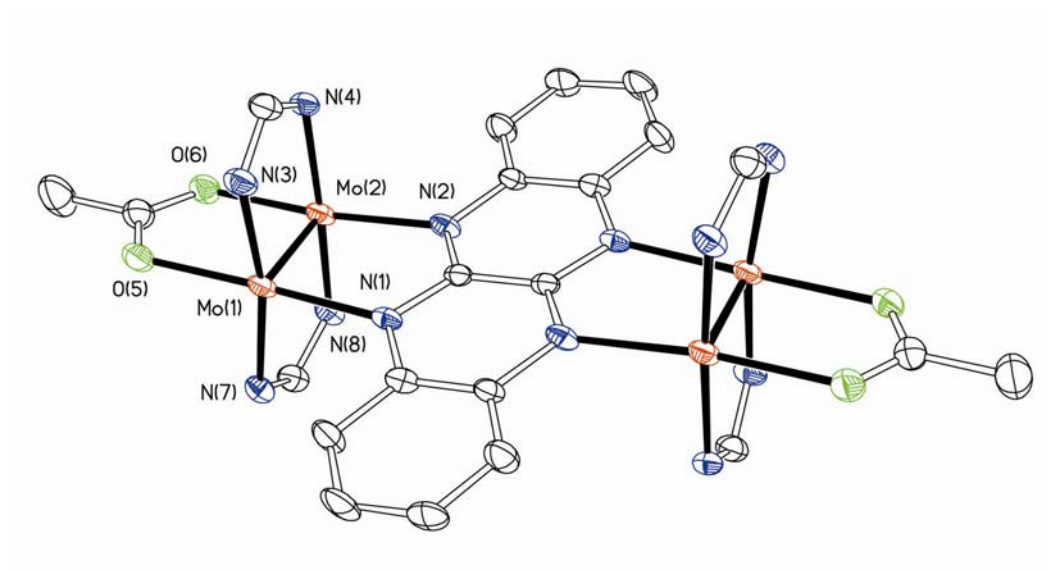
Figure 13. Core of **9** in **9**·4CH$_2$Cl$_2$ displacement ellipsoids drawn at the 40% probability

level. All *p*–anisyl groups and hydrogen atoms have been omitted for clarity.
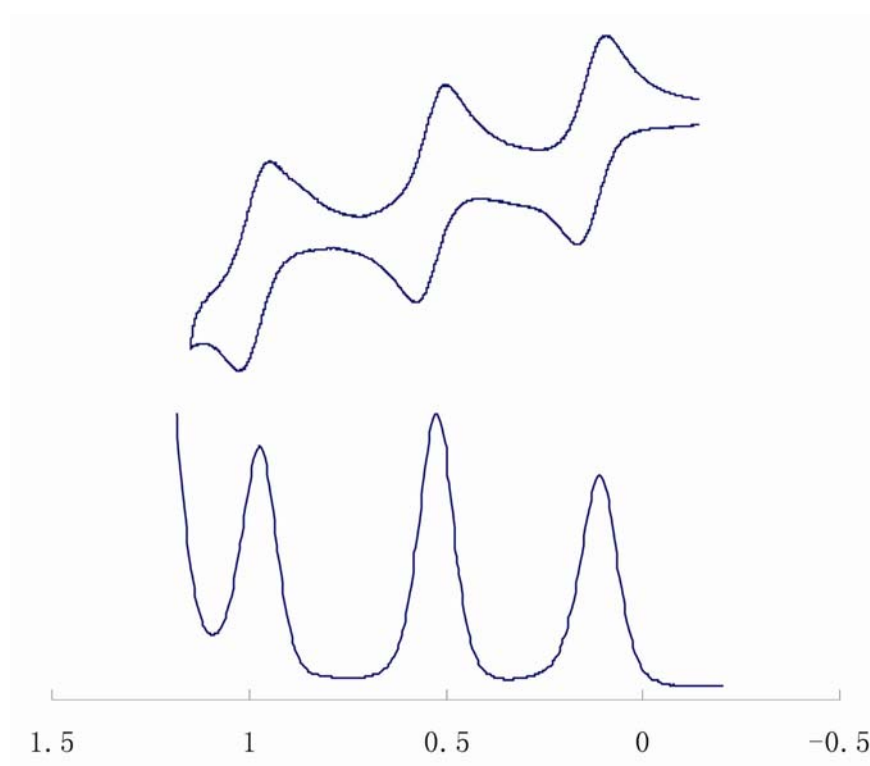
Figure 14. Cyclic voltammogram and differential pulse voltammogram (DPV) for **5** in CH$_2$Cl$_2$ solution (with potentials vs Ag/AgCl).

Table 5. Influence of Linker, L, on $\Delta E_{1/2}$ and Kc in Some $[Mo_2]L[Mo_2]$ Species.

Linker	Relative orientation of [Mo$_2$] units	$[Mo_2]\cdots[Mo_2]$ (Å)	$E_{1/2}^{+/0}$ (mV)	$E_{1/2}^{2+/+}$ (mV)	$\Delta E_{1/2}$ (mV)	Kc
fluoflavinate (in **5**)	∥	7.174	79	495	416	1.1×10^7
fluoflavinate (in **9**)	∥	7.108	199	619	420	1.3×10^7
α–diphenyloxamidate	⊥	7.096	176	367	191	1.7×10^3
α–di–*p*–anisyloxamidate	⊥	7.081	183	373	190	1.6×10^3
Oxalate	∥	6.953	294	506	212	3.8×10^3

occurs.[47] Calculations at the DFT level (vide infra) suggest that the redox process at 795 mV is associated with the linker fluoflavinate which is "non–innocent" under the electrochemical conditions of the experiment. By comparison, the third redox process in **5** may be assigned to the fluoflavinate anion. In the radical cation, the additional unpaired electron is expected to reside on a ligand–based orbital. This assignment is also consistent with the high instability of triply oxidized product of **5**.

Attempts to conduct electrochemical measurements on fluoflavine itself were unrewarding because of its very low solubility in organic solvents. To circumvent this problem, we have made the 2–methyl derivative, which has enough solubility to allow measurement of its electrochemistry. It shows a redox process at $E_{1/2}$ = 920 mV. This value is between the high potential in **8** (795 mV) and that for **5** (1004 mV) and it has been assigned to the oxidation of the amine.

Following the preceding assignment of the redox potentials to the corresponding redox sites, one can evaluate the degree of the electronic communication in the MV species **6**. The CV and DPV of **5** show that the oxidation potentials for the two [Mo$_2$] units are separated by 416 mV, or $\Delta E_{1/2}\,(1) = E_{1/2}^{(2+/1+)} - E_{1/2}^{(1+/0)}$. From this value of $\Delta E_{1/2}$, a comproportionation constant Kc of 1.1×10^7 can be derived. This magnitude of Kc indicates that the two [Mo$_2$] units in **5** are strongly electronically coupled by the fluoflavinate linker and the mixed–valence species, **6a** and **6b**, are thermodynamically stable with respect to the neutral compound **5** and doubly oxidized compound **7**. The large Kc value (1.1×10^7) is similar to those in the β–isomers of the oxamidate analogue in which the Kc is 9.5×10^8. These oxamidate analogues have been classified as a Class

III according to Robin and Day's classification because of the large electron delocalization.[6(b)]

In contrast, in the α–oxamidate linked compound which has two orthogonal [Mo_2] units, the possibility of metal–ligand orbital overlap is eliminated, and the mixed–valence species has been spectroscopically and structurally characterized to be electron localized, Class I. For the oxalate anion linked compound, whose conformation may change as a rotation about the C−C single bond takes place, only weak coupling between the two [Mo_2] units is observed. Although the metal–metal separations in all compounds in Table 5 are similar, for the fluoflavinate compounds there is an increase of over 200 mV in ΔE. It should also be noted that the potentials in **9** are shifted to higher values relative to those in **5**, in keeping with the lower basicity of the acetate bridge but the $\Delta E_{1/2}$ values are similar.

It is clear that the fluoflavinate linker plays a critical role in enhancing the electronic communication and this is due to the rigid conjugated π system of the anion and robust structure of the molecule. The rigidity and planar conformation of the linker allows continuous orbital overlap to be established between the metal δ orbitals and the linker π orbitals. Thus, the linker in the doubly oxidized **7** can be thought of as a tetraazatetracene which is analogous to the well known aromatic tetracene, often called naphthacene.

Near–IR Spectrum. The spectrum of a solid sample of **6a** in a KBr pellet, measured in the 1600–6000 cm^{-1} region, shows a relatively intense band, somewhat unsymmetric, peaking at about 3400 cm^{-1} and centered at about 3800 cm^{-1} (Figure 15). The observed bandwidth, $\Delta\nu_{1/2}$ of about 2100 cm^{-1}, is significantly smaller than the 2820 cm^{-1} calculated using the Hush formula $\Delta\nu_{1/2} = (2310\ \nu_{max})^{1/2}\ cm^{-1}$. [48] Since the value from the Hush model is the prediction for a Class II compound, a narrower band is generally considered to be an indication that the electronic communication is better than that in a Class II compound. This band is similar to that in the $\{[Bu^tCO_2)_3Mo_2]_2(\mu\text{–oxalate})\}^+$ ion. [49] Thus, the near–IR spectrum is consistent with structural results in suggesting that the fluoflavinate linker mediates strong electronic coupling between the two linked $[Mo_2]$ units, and resemble the previously reported Class III β–oxamidate–bridged analogues.
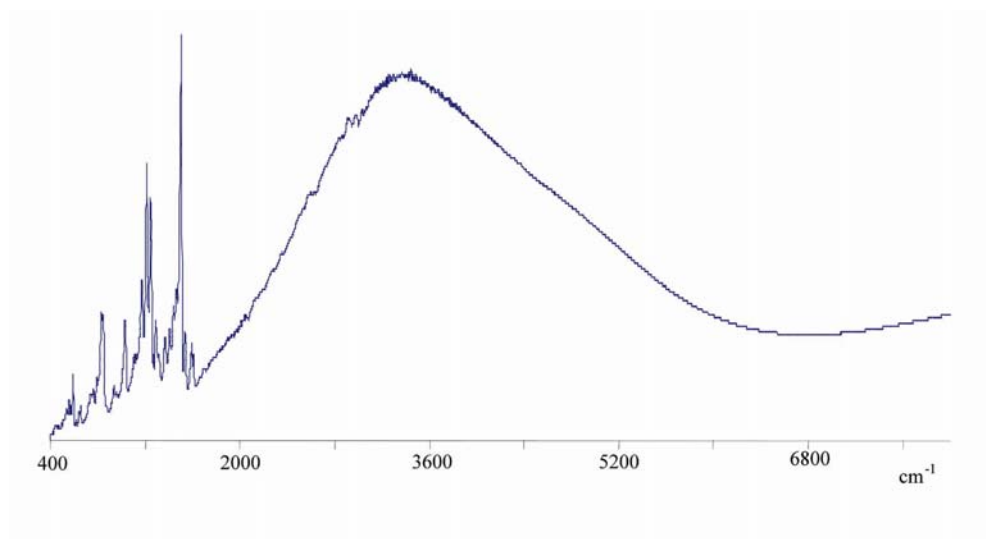
Figure 15. Near–IR spectrum of the mixed–valence species **6a** using a KBr pellet.

EPR Spectrum and Magnetism. The X–band electron paramagnetic resonance spectrum of the singly oxidized **6a** in frozen CH_2Cl_2 solution exhibits a symmetric signal devoid of hyperfine structure. The g_{iso} value of 1.943 is significantly lower than that for a free organic radical, indicating that the odd electron resides in a metal–based orbital.[34,50] Such an assignment is also consistent with the structural data discussed before. In the absence of observed hyperfine structure, the EPR spectrum provides no evidence concerning the extent of delocalization of the unpaired electron.

Magnetic susceptibility measurements on a crystalline sample of **6a**, from 5 to 300 K, show that χT in this temperature range has an essentially constant value of ca. 0.38 emu K mol^{-1}. This value is within the range expected for a system with one unpaired electron, and it is consistent with the EPR spectrum and crystal structure of the singly oxidized species.

The magnetism for compound **7**, measured in the same temperature range (5 to 300 K), shows a small residual value of χT. The value changed from sample to sample but it was always temperature–independent for any one sample. This is consistent with the presence of a compound that is essentially diamagnetic but always contaminated with a small, but variable, amount of the singly oxidized species **6**. The source of **6** is not certain but presumably it is produced because of the instability, already mentioned, of **7**. The diamagnetism is consistent with strong electronic coupling between the $[Mo_2]$ units, as observed in the β–oxamidate system, which gives a singlet ground state.

DFT Calculations and Electronic Structure. Based on symmetry considerations, a qualitative description of the bonding and MO interactions that arise between the frontier

[Mo$_2$] δ orbitals and the π orbitals of the fluoflavinate linker can be obtained, as shown in Figure 16. On the right of the figure are the two highest–occupied [Mo$_2$]–based orbitals which are composed of the in–phase (b_{1u}) and out–of–phase (b_{2g}) combinations of the δ orbitals, δ+δ and δ–δ, respectively, and two unoccupied [Mo$_2$]–based orbitals composed of in–phase (b_{3g}) and out–of–phase (a_u) combinations of the δ* orbitals, δ*+δ* and δ*–δ*, respectively. On the left side of the diagram are orbitals that arise from the ligand π system. The two highest–occupied orbitals of the ligand have b_{2g} and b_{3g} symmetries, and the three lowest unoccupied orbitals have b_{1u}, b_{3g} and a_u symmetries. By combining the ligand and metal–based orbitals, the MO diagram in the central section of Figure 16 is obtained. The metal–based b_{2g} orbital is raised in energy due to the interaction with the filled b_{2g} ligand orbital, whereas the metal–based b_{1u} orbital is stabilized because of a backbonding interaction with the empty b_{1u} ligand orbital. In this diagram the occupied b_{3g} ligand orbital is placed at higher energy than the metal based b_{1u} orbital to be consistent with the experimental observation of a third reversible redox process that has been assigned as being a ligand–based oxidation.

This qualitative picture is useful for the interpretation of the electronic structures of **5**, **6**, **7** and the paddlewheel species **8** which were investigated with Density Functional Theory. For practical reasons, simplified models in which each of the *p*–anisyl groups of the formamidinate ligands was replaced by a hydrogen atom were utilized for all the calculations. For comparison purposes, three different functionals, (B3LYP, mPW1PW91, and BP86) were utilized in this work, and the calculated distances for all models are shown in Table 6.
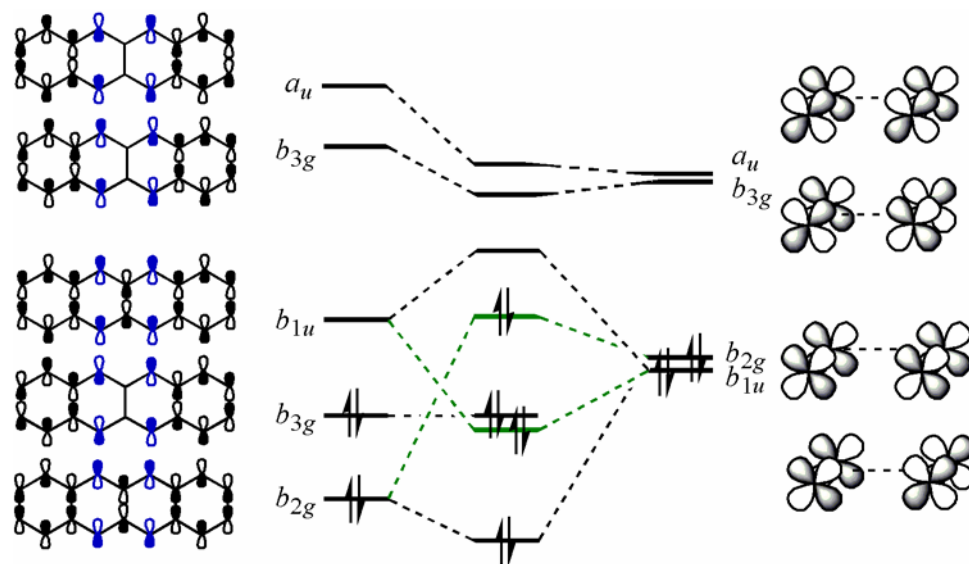
Figure 16. Frontier orbital interactions between the δ orbitals combinations of the [Mo$_2$] units and π orbitals of the fluoflavinate linker. In the left column, the nitrogen p orbitals of the fluoflavinate are shown in blue. In the center, metal δ–based orbitals are shown in green.

Table 6. Calculated Distances for the Models of **5**, **6** and **7**.

Functional	Model	Charge	Spin	Selected Distances (Å)			
				Mo–Mo	C–C^a	Mo–N^b	Mo$_2$···Mo$_2$
B3LYP	**5**	0	0	2.1322	1.4587	2.1804	7.2193
	6	1	½	2.1482	1.4475	2.1492	7.1529
	7	2	0	2.1579	1.4427	2.2198	7.1845
		2	1	2.1630	1.4682	2.1797	7.2034
mPW1PW91	**5**	0	0	2.1158	1.4513	2.1576	7.1595
	6	1	½	2.1333	1.4393	2.1268	7.0942
	7	2	0	2.1488	1.4273	2.0998	7.0390
		2	1	2.1467	1.4616	2.1594	7.1471
BP86	**5**	0	0	2.1554	1.4573	2.1711	7.2235
	6	1	½	2.1682	1.4525	2.1518	7.1782
	7	2	0	2.1742	1.4500	2.2273	7.2258
		2	1	2.1784	1.4672	2.1622	7.2414
Experimental	**5**	0	0	2.0939	1.450	2.163	7.174
	6	1	½	2.1084$^{(b)}$	1.429	2.128	7.100
	7	2	0	2.1245	1.427	2.130	7.090

^{a} The central C−C bond in the fluoflavinate linker. ^{b} Average values for two dimetal

units.

Geometry optimization results for the models of **5**, **6**, and **7** shows that the bond distances calculated using the mPW1PW91 functional are in close agreement with the experimental results obtained by X–ray crystallography. For example, the calculated Mo−Mo bond distances for the model of **5** are only 0.02 Å longer than the experimental distances whereas B3LYP and BP86 overestimates this distance by 0.04 and 0.06 Å, respectively. The mPW1PW91 functional also provides better accuracy than B3LYP and BP86 when the Mo−N bond distances are calculated.

A similar result is obtained in the calculation of the distances in the model of the singly–oxidized compound **6**. Again the mPW1PW91 functional gives the best agreement with the X–ray structural parameters. However, all three functionals were capable of reproducing the magnitude of the experimental increase in Mo−Mo distances (0.015 Å) compared to those observed in their respective neutral models. This increase is consistent with the effect of removing an electron from a bonding metal δ orbital and leaving a positive charge delocalized over two [Mo$_2$] units.

Although experimental data favor a singlet spin state for the doubly oxidized compound **7**, calculations were done on models in two possible spin states having $S = 0$ and $S = 1$. For each spin state, calculations were performed with each of the three functionals mentioned above. In general, the calculated distances from the singlet state calculations are in better agreement to the crystallographic values than those obtained from the triplet state calculations. For instance, the calculated Mo−Mo bond distances for the singlet state for each functional, although generally overestimated, are shorter than those from the triplet state calculations. To summarize, for all calculated models of

different oxidation states, mPW1PW91 consistently provided significantly better structural parameters than B3LYP, and BP86 typically yielded results that differ the most from the experimental values.

Graphic illustrations of the frontier B3LYP MOs of the model of **5** are shown in Figure 17 and energy results of all calculated models are in Table 7. As anticipated from the qualitative depiction in Figure 16, and regardless of the functional utilized, the HOMO consists of the out–of–phase combination of the δ orbitals, of b_{2g} symmetry with some contribution from the b_{2g} ligand orbital. Also, as expected, the HOMO−1 and HOMO−2 are calculated to be very close in energy (0.09 eV according to the B3LYP calculation). For the three functionals, the HOMO−1 is always the in–phase combination of the δ orbital with a significant contribution of the b_{1u} ligand orbital, and the HOMO−2 is the ligand–based b_{3g}. For the model of **6**, the electronic structure is similar to that for the model of **5**. The SOMO is composed of the metal based b_{2g} orbital, δ–δ. This is consistent with the EPR spectrum that shows a low value of g of 1.94, which indicates that the unpaired electron is distributed over a mainly metal–based MO.

The electronic structure of the model of the doubly–oxidized singlet state may be derived from that of the neutral molecule by removal of the b_{2g} electrons (see Figures 16 and 17). For all functionals used in the calculations, the HOMO is the metal–based b_{1u} orbital (δ+ δ), and the HOMO−1 is the ligand based b_{3g}, while the LUMO is the metal–based b_{2g} (δ− δ), which is occupied in the neutral and singly–oxidized models. In the triplet state, $S = 1$, the b_{2g} and b_{1u} metal–based orbitals are both singly occupied.

Table 7. Calculated Energies for the Models of **5**, **6**, **7** and **8**.

Model	Charge	Multiplicity	Spin	Energy (a.u.)		
				B3LYP	mPW1PW91	BP86
5	0	1	0	−1924.1702	−1923.8475	−1924.6304
6	+1	2	½	−1923.9991	−1923.6760	−1924.4586
7	+2	1	0	−1923.7035	−1923.3749	−1924.1680
7	+2	3	1	−1923.7175	−1923.3960	−1924.1631
7	+2	1	B.S.	−1923.7196	NA	NA
7	0	1	0	−1341.2982	−1341.0520	NA

LUMO + 1, b_{3g}

LUMO, b_{1u}

HOMO, b_{2g}

HOMO − 1, b_{1u}

HOMO − 2, b_{3g}
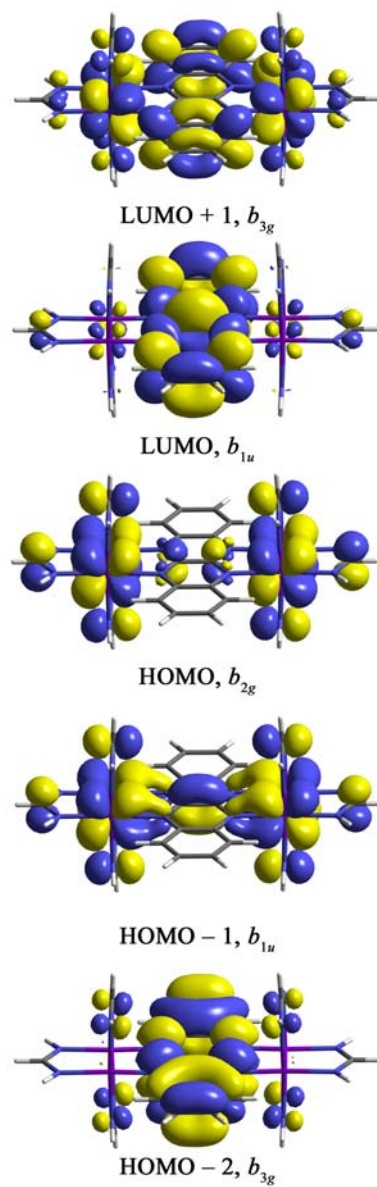
Figure 17. The 0.02 surface contour diagrams for the frontier molecular orbitals for the model of compound **5**, calculated by DFT.

It should be noted that the bond distances of the singlet state are in better agreement with the experimental results than those from the triplet state. However, the total energy of the triplet state calculated with both hybrid functionals was lower than that of the singlet state (0.38 and 0.57 eV for B3LYP and mPW1PW91, respectively), and only slightly higher (0.13 eV) for BP86. Because the amount of Hartree–Fock exchange in the hybrid functionals B3LYP and mPW1PW91 tends to favor higher multiplicity states, the energy difference between the singlet and triplet states is likely to be underestimated. Previous work on compounds of the type [Mo$_2$]L[Mo$_2$] has also shown that the broken–symmetry (BS)[51] method is useful for modeling partially delocalized systems utilizing unrestricted DFT, and that this approach can be coupled with Yamaguchi's relationship[52] to compute an accurate estimate of the Heisenberg magnetic exchange coupling constant, 2J. As shown in Table 7, applying the BS approach indeed provides a lower energy than the triplet state, and by utilizing Yamaguchi's relationship the estimated 2J value is –923 cm^{-1}, which is consistent with the magnetic susceptibility results that show that **7** is a diamagnetic system at and below 300 K.

It is also worth noting that for the singlet state of the doubly oxidized model of **7**, the calculated energy difference between the HOMO, b_{1u}, and HOMO−1, b_{3g}, is very small. Thus, it is possible that, in solution, the ligand based b_{3g} orbital may be the HOMO, and this may account for the third oxidation wave observed in the cyclic voltammogram. Similarly, the electronic structure of a model of the paddlewheel compound **8**, obtained with B3LYP, shows that while the HOMO is primarily metal δ, the HOMO−1 is ligand based. This supports the assignment of the second oxidation

wave in **8** as being ligand–based and suggests that the assignment of the third wave in the CV of **5** to a ligand redox process is correct.

Finally, TD–DFT calculations were also performed on all three models of **5** and **6** in order to help assign the lowest energy transitions in their UV–vis electronic spectra, and the NIR of **6**. The results indicate that for **5** the band at 512 nm may be assigned to a δ–δ → π–ligand (HOMO→LUMO) transition, which is allowed in x polarization and calculated at 534 nm. The band at 482 nm may be assigned to a δ+δ → δ*+δ* transition, allowed in y polarization, and calculated at 490 nm. The band at 460 nm may be assigned to a δ–δ → δ*–δ* transition, calculated at 472 nm and which is also allowed in y polarization. For **6**, the intense NIR band at 3800 cm^{-1} is mainly a δ–δ → δ+δ (HOMO−1 → SOMO) transition calculated at 5618 cm^{-1} (f = 0.168). This is the so–called *intervalence* band that is typically observed for compounds near the Class II/Class III border. The bands observed in the visible region for **6** at 622 and 550 nm may be assigned to the δ+δ → δ*+δ* and δ–δ → δ*–δ* transitions and they are calculated at 815 and 578 nm, respectively.

CHAPTER IV

THE UNSUBSTITUTED OXAMIDATE AND DITHIOOXAMIDATE IONS AS BRIDGES BETWEEN TWO DIMOLYBDENUM UNITS

INTRODUCTION

A previous study[19] showed that dioxamidate dianions, $^-$RN(O)C–C(O)NR$^-$, in which the R groups are C_6H_5, p–$CH_3OC_6H_4$ give two isomeric structures of dimers of $Mo_2(DAniF)_3^+$ (DAniF = N,N'–di–p–anisylformamidinate). Each showed very different properties and electronic communication. In the α form, the amidate linkers is non planar, with the two RN(O)C planes being approximately perpendicular while the β form has a planar heteronaphthalene–like structure. When R = CH_3 groups, only the β form has been obtained. The results just summarized raised the question of what effects other N–substituents would have on the relative stability of the α and β isomers. In this work, we decided to use the unsubstituted oxamidate dianion, $^-$HN(O)C–C(O)NH$^-$, which could lead to a planar arrangement through hydrogen bonding.

Recent processes in protein crystallography revealed that many molybdenum enzymes contain terminal sulfur donor ligands.[53] These sulfur atoms appear to be crucial to enzyme reactivity, particular for the possibility that Mo–S orbital overlap provides an effective low-energy pathway for electron transfer to and from the metal.[54] However, the electron transfer process through S–donor ligand has barely been studied. Therefore, the oxamidate analogue with S–donor atoms instead of O, dithiooxamidate

$^-$HN(S)C–C(S)NH$^-$ was also used to bridge the Mo$_2$ units to see how the S atoms influence the electronic communication between the dimetal units.

EXPERIMENTAL SECTION

Preparation of [Mo$_2$(DAniF)$_3$]$_2$(oxamidate), 10. To a solution of Mo$_2$(DAniF)$_3$(OCCH$_3$) (508 mg, 0.50 mmol) and oxamide (22.0 mg, 0.25 mmol) in 15 mL THF was added, slowly and with stirring, a sodium methoxide solution of 1.0 mL (0.5 M in CH$_3$OH). An orange solid formed in about 20 min. After one hour, the solvent was evaporated under reduced pressure. The solid residue was extracted using CH$_2$Cl$_2$ (ca.15 mL). The mixture was filtered using a Celite–packed frit and the volume of the filtrate was reduced under vacuum to ca. 5 mL. Then, 30 mL of hexanes was added, producing an orange precipitate. The solid product was collected by filtration and dried under vacuum. Yield: 325 mg (82%). Single crystals for X–ray analysis was obtained by diffusion of hexanes into a dichloromethane solution of the orange product. ^{1}H NMR (δ, ppm in CD$_2$Cl$_2$): 10.27 (s, 2H, –NH), 8.50 (s, 2H, –NCHN$^-$), 8.42 (s, 4H, –NCHN$^-$), 6.60 ~ 6.54 (m, 24H, aromatic C–H), 6.48 ~ 6.43 (m, 8H, aromatic C–H), 6.41 ~ 6.38 (d, 8H, aromatic C–H), 6.24 ~ 6.21 (d, 8H, aromatic C–H), 3.70 (s, 12H, –OCH_3), 3.68 (s, 12H, –OCH_3), 3.66 (s, 6H, –OCH_3), 3.65 (s, 6H, –OCH_3). UV–vis, λ_{max} nm (ε, M^{-1}·mol^{-1}): 460 (2.0 × 10^3), 412 (1.1 × 10^3). Anal. Calcd. for C$_{95}$H$_{98}$Cl$_6$Mo$_4$N$_{14}$O$_{14}$ (**10**·3CH$_2$Cl$_2$): C, 50.56; H, 4.38; N, 8.69. Found: C, 50.55; H, 4.67; N, 8.79.

Preparation of [Mo₂(DAniF)₃]₂(dithiooxamidate), 11. To a solution of $Mo_2(DAniF)_3(OCCH_3)$ (406 mg, 0.40 mmol) and dithiooxamide (24.0 mg, 0.20 mmol) in 25 mL THF was added, slowly and with stirring, 0.8 mL of a sodium methoxide solution (0.5 M in CH_3OH). The color of the mixture turned dark blue. The reaction mixture was stirred at ambient temperature for 2 h. After removing the solvents under reduced pressure, the solid residue was extracted using CH_2Cl_2 (ca. 15 mL). The mixture was filtered using a Celite–packed frit and the volume of the filtrate was reduced under vacuum to ca. 5 mL. Then, 40 mL of ethanol was added, producing a blue precipitate, which was washed by ethanol (2 × 20 mL) and hexanes (20 mL). This solid was dried under vacuum, then redissolved in 15 mL of CH_2Cl_2 and layered with hexanes. Blue crystals formed within 3 days. Yield: 345 mg (85%). ^1H NMR (δ, ppm in $CDCl_3$): 11.75 (s, 2H, –N*H*), 8.47 (s, 2H, –NC*H*N–), 8.35 (s, 4H, –NC*H*N–), 6.50 ~ 6.65 (m, 40H, aromatic C–*H*), 6.18 (d, 8H, aromatic C–*H*), 3.73 (s, 12H, –OC*H₃*), 3.71 (s, 6H, –OC*H₃*), 3.69 (s, 12H, –OC*H₃*), 3.68 (s, 6H, –OC*H₃*). UV–vis, λ_{max} nm (ε, $M^{-1} \cdot mol^{-1}$): 600 (8.0 × 10^3), 450 (1.1 × 10^3). Anal. Calcd. for $C_{92}H_{92}Mo_4N_{14}O_{12}S_2$: C, 54.33; H, 4.56; N, 9.64. Found: C, 54.03; H, 4.62; N, 9.56.

Preparation of [Mo₂(DAniF)₃]₂[Li(THF)₂]₂(C₂N₂S₂), 12. A solution of **11** (163 mg, 0.08 mmol) in 15 mL of THF was cooled to −78°C. To this blue solution was added slowly, with stirring, 0.15 mL of 1.6 M Bu^{t}Li in hexanes. The reaction mixture was allowed to warm to room temperature over a period of 1 h. The color of the mixture changed from blue to red. The mixture was filtered through a Celite packed frit and the

filtrate was layered with hexanes and keep at –20 °C. Red crystals formed within 10 days. Yield: 72 mg (39%).

Computational Details. Density functional theory (DFT) calculations were performed with the hybrid Becke's three–parameter exchange functional and the Lee–Yang–Parr nonlocal correlation functional (B3LYP)[38] in the Gaussian 03 program. Double–ζ quality basis sets (D95) were used on C, N and H atoms as implemented in Gaussian. For O and S atoms, correlation consistent double–zeta basis sets (CC–PVDZ)[55] were applied. A small effective core potential (ECP) representing the 1s2s2p3s3p3d core was used for the molybdenum atoms along with its corresponding double–ζ basis set (LANL2DZ).[43] Time–dependent density functional (TD–DFT)[44] calculations were performed to assign the electronic spectra of these compounds. All calculations were performed on either Origin 3800 64–processor SGI or Origin 2000 32–processor SGI supercomputers located at the Texas A&M supercomputing facility.

RESULTS AND DISCUSSION

Syntheses. Previously we have reported the syntheses of dimers of dimolybdenum linked by aryl–substituted oxamidate ligands starting from $Mo_2(DAniF)_3(O_2CCH_3)$ in THF with the presence of $NaOCH_3$. Two isomers were isolated by different treatment of the reaction solutions. Here, the unsubstituted oxamidate $^-HN(O)C–C(O)NH^-$ was used and a yellow precipitate was formed under the same reaction conditions. The product **10** does not dissolve in THF giving an extra driving force for the clean reaction. The analogous ligand containing S donor atoms instead of O, dithiooxamidate was also used

as a linker to form compound **11**. Compound **11** is very soluble in THF and dichloromethane than compound **10**. In both cases, the ^{1}H NMR spectra show that only one species was produced. The reaction is illustrated by the following equations:

$$Mo_2(DAniF)_3(O_2CCH_3) + NaOCH_3 \xrightarrow{THF} Mo_2(DAniF)_3(OCH_3)(HOCH_3) + NaO_2CCH_3$$

$$2Mo_2(DAniF)_3(OCH_3)(HOCH_3) + H_2N(L)CC(L)NH_2 \longrightarrow [Mo_2(DAniF)_3]_2[HN(L)CC(L)N(H)]$$

$$L = O \text{ or } S$$
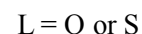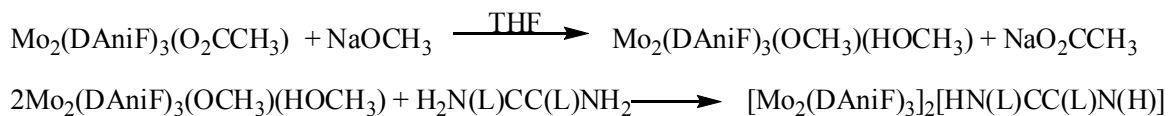
The two linkers, $^-$HN(O)C–C(O)NH$^-$ and $^-$HN(S)C–C(S)NH$^-$, are different from all the other diamidate and dicarboxylate ligands because they have additional H atoms (N–H), which can be further deprotonated. Upon addition of methyllithium to the suspension of **10** in THF at -70ºC, compound **10** did not show any change, while at the same conditions, the solution of compound **11** changed from dark blue to orange immediately. The isolated compound from the reaction of **11** with LiMe shows that the H atoms (N–H) are removed and two Li$^+$ were coordinated to the ligand. This is consistent with the fact that $^-$HN(S)C–C(S)NH$^-$ is more acidic than $^-$HN(O)C–C(O)NH$^-$. Compound **12** is very unstable even in the solid state, and quickly decomposes at room temperature.

Structural Results. Crystallographic data for **10·**4CH$_2$Cl$_2$, **11·**4CH$_2$Cl$_2$ and **12·**2THF are given in Table 8, and selected bond distances in Table 9. Compound **10** crystallized with the space group $P\bar{1}$ with the molecule residing on an inversion center. The core structure is shown in Figure 18. The relative geometry and conformation is similar to that linked by oxalate anion, but different from either α or β forms linked by the substituted oxamidates. Two groups of Mo$_2$ units are coordinated to the bridge in the way to form $\overset{\displaystyle\ulcorner\urcorner}{O-Mo-Mo-N-C}$ five–membered rings, which is the same in the α

Table 8. X–ray Crystallographic Data for **10**, **11** and **12**.

	10·4CH₂Cl₂	**11·4CH₂Cl₂**	**12·2THF**
empirical formula	$C_{96}H_{100}Cl_8Mo_4N_{14}O_{14}$	$C_{96}H_{100}Cl_8Mo_4N_{14}O_{12}S_2$	$C_{116}H_{138}Li_2S_2Mo_4N_{14}O_{18}$
Fw	2341.26	2373.38	2478.16
Space group	$P\bar{1}$ (No. 2)	$P\bar{1}$ (No. 2)	$P\bar{1}$ (No. 2)
a, Å	12.443(4)	12.386(5)	14.082(4)
b, Å	14.608(5)	14.562(6)	15.332(5)
c, Å	15.179(5)	15.500(6)	16.125(5)
α, deg	72.118(5)	71.826(7)	115.267(5)
β, deg	83.062(6)	83.923(7)	106.596(5)
γ, deg	71.362(5)	71.386(6)	99.045(7)
V, Å³	2487.3(13)	2517.3(17)	2856.4(16)
Z	1	1	1
T, K	213	213	213
λ, Å	0.71073	0.71073	0.71073
d_{calcd}, g/cm³	1.563	1.566	1.441
μ, mm⁻¹	0.777	0.807	0.537
R1[a] (wR2[b])	0.0638(0.1286)	0.0920(0.1675)	0.1245(0.1835)

[a] $R1 = \Sigma||F_o|-|F_c||/ \Sigma|F_o|$. [b] $wR2 = [\Sigma[w(F_o^2-F_c^2)^2]/\Sigma[w(F_o^2)^2]]^{1/2}$

Table 9. Selected Bond Lengths (Å) and Angles (º) for **10**, **11** and **12**.

	10·4CH₂Cl₂	**11·4CH₂Cl₂**	**12·4THF**
Mo(1)–Mo(2)	2.0903(7)	2.0894(13)	2.0948(13)
Mo(2)–O(1)	2.137(3)		
Mo(2)–S(1)		2.465(3)	2.435(3)
Mo(1)–N(1)	2.127(3)	2.193(11)	2.072(8)
Mo(1)–N(2)	2.159(4)	2.141(6)	2.133(8)
Mo(1)–N(4)	2.129(4)	2.157(6)	2.189(7)
Mo(1)–N(6)	2.157(4)	2.128(6)	2.172(9)
Mo(2)–N(3)	2.139(3)	2.158(7)	2.159(8)
Mo(2)–N(5)	2.145(4)	2.136(6)	2.172(8)
Mo(2)–N(7)	2.130(3)	2.174(6)	2.142(9)
C(1)–O(1)	1.317(6)		
C(1)–S(1)		1.865(19),	1.798(10)
C(1)–N(1)	1.297(6)	1.17(2)	1.293(11)
Li(1)–S(1)			2.37(2)
Li(1)–N(1)			1.977(18)
N(1)–C(1)–O(1)	124.4(4)		
N(1)–C(1)–S(1)		115.2(16)	121.2(8)
N(1)–Li(1)–S(1A)			87.2(7)

form, while in the β form, the Mo_2 coordinated differently forming a six–membered

ring C—O—Mo——Mo—N—C .[19] However, the two Mo_2 units are essentially

parallel to each other in compound **10**, which is similar to that in the case of β form,

while in the α form, the two Mo_2 units are almost perpendicular. The molecule is flat and

it has a pseudo C_{2h} geometry. The Mo–Mo distance of 2.0903(7) Å is a typical quadruple

bond distance for dimolybdenum embraced by four, three–atom bridging ligands, such

as $Mo_2(DAniF)_4$ and $Mo_2(OCCH_3)_4$. For comparison, the Mo–Mo distances for α or β

forms linked by *N,N'*–di–*p*–anisyloxamidate are 2.0927(8) Å and 2.0944(4) Å. The

distance between the centers of the two Mo–Mo bond is 6.978 Å, close to the values in

the α form. The central C–C bond distance of 1.502(9) Å is close to the C–C single bond

in neutral ligand.[56] The oxygen to the H atom (N–H) is 2.412 Å and intramolecular

hydrogen bond O···H–N was formed. This hydrogen bond gives extra energy to stabilize

the planar conformation of compound **1**. DFT calculations on model compounds

(discussed later) show that the energy for planar conformation is about 48 Kcal/mol

lower than the perpendicular conformation. This high barrier to the rotation along the

C–C single bond implies that the compound will remain planar in solution.

Compounds **11** and **10** are isostructural and they have similar cell dimensions.

Compound **11** also crystallized in the space group $P\bar{1}$ with the molecule residing on an

inversion center. The structure is shown in Figure 19. The Mo–Mo bond distance of

2.0894(13) Å is similar to that in **10**. The Mo–S distance of 2.4565(3) Å is about 0.33 Å

longer than Mo–O distance due to larger size of S atoms compared to O atoms and

consequently the nonbonding separation between the two Mo_2 units measured by the

midpoints of the Mo_2 axis increases from 6.978 Å to 7.471 Å. All the other distances and angle are as expected.

Compound **12** also crystallized in the space group $P\bar{1}$ with Z = 1. As shown in Figure 20, the H atoms (N–H) have been replaced by two Li atoms coordinated. Two THF molecules coordinated to each Li to form tetrahedral geometry. The Mo–Mo distance is 2.0948(13) Å. The Mo–N(bridge) distances decrease from 2.193(11) Å in **10** to 2.072(8) Å in **11**, and consequently the N(1)–C(1)–S(1) angle increases from 115.2(16)° to 121.2(8)°. All the other bond lengths did not show much change from the corresponding values in compound **11**. The Li–N and Li–S distances are 1.293(11) Å and 1.798(10) Å, respectively.
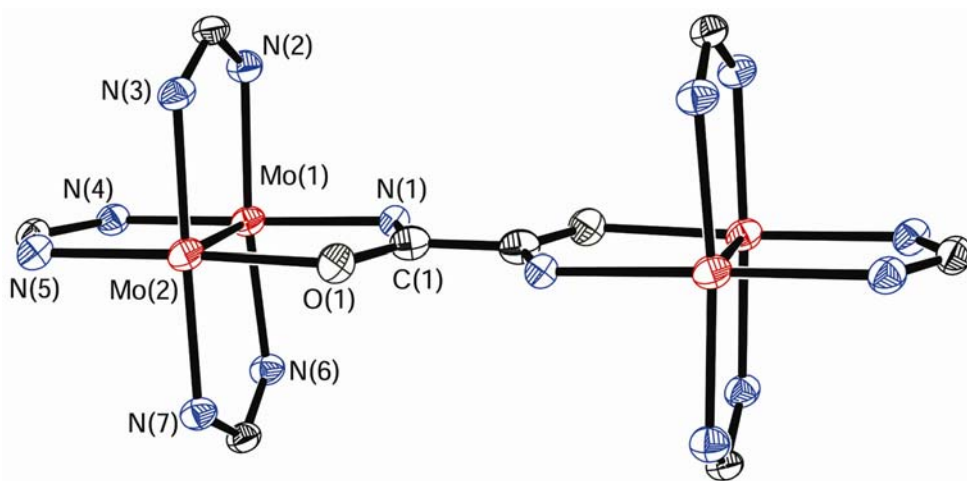
Figure 18. Core structure of **10** with displacement ellipsoids drawn at the 40% probability level. All *p*–anisyl groups and hydrogen atoms have been omitted for clarity.
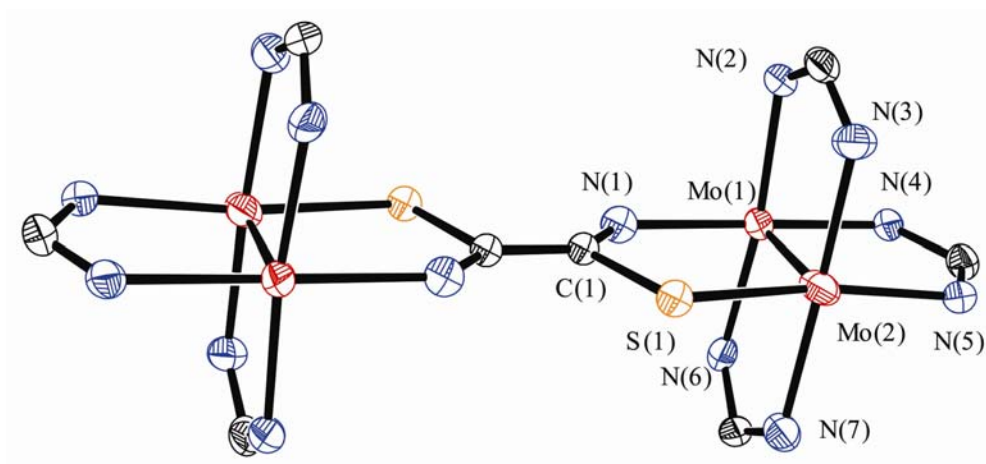
Figure 19. Core structure of **11** with displacement ellipsoids drawn at the 40% probability level. All *p*–anisyl groups and hydrogen atoms have been omitted for clarity.
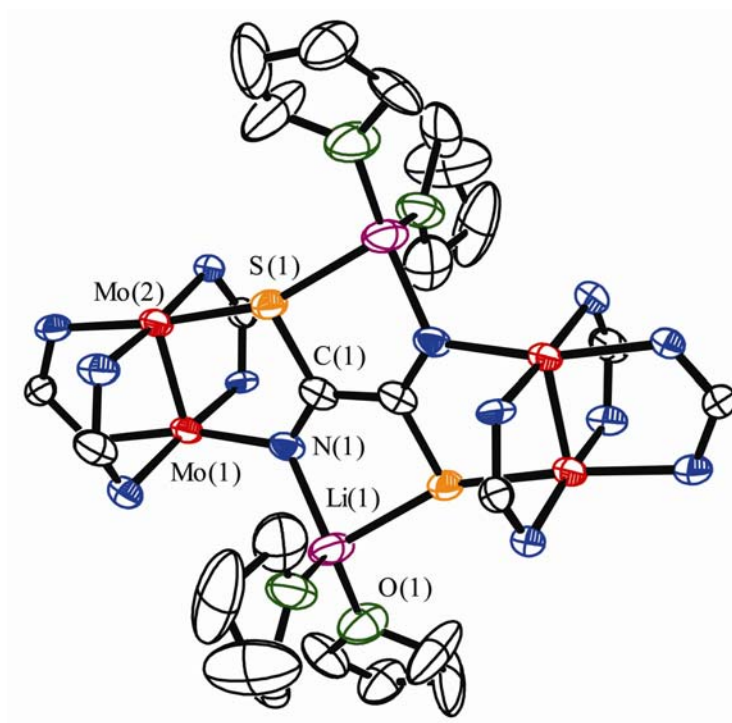
Figure 20. Core structure of **12** with displacement ellipsoids drawn at the 40% probability level. All *p*–anisyl groups and hydrogen atoms have been omitted for clarity.

Electrochemistry. The electrochemistry has been used as an important technique to evaluate the electronic communication effect between redox–active metal centers. The CV of compound **10** and **11** both show reversible oxidation processes (Figure 21). The difference between the two waves $\Delta E_{1/2}$ are 204 mV ($E_{1/2}(1) = 280$, $E_{1/2}(1) = 484$) and 407 mV ($E_{1/2}(1) = 294$, $E_{1/2}(1) = 701$), corresponding to the comportionation constant K_c of 2.8×10^3 and 7.6×10^6, respectively. Thus by changing the O donor atoms in the oxamidate bridge to S, the electronic coupling between the metal centers is greatly enhanced. Similar trends were observed for the successive substitution of oxygen by sulfur in dicarboxylates for the compounds $[(Bu^tCO_2)_3M_2]_2(X_2CC_6H_4CX_2)$ (M = Mo and W, X = O or S).[12(a), 57] A summary of the electrochemistry data for these closely related systems is shown in Table 10. Previous studies show that the distance between the Mo_2 units and the metal to ligand back bonding play significant role in modifying the electronic coupling. Here the two compounds, **10** and **11**, share a common core structure and the distance between the metal centers in **11** is about 0.5 Å longer than that in **10**, but the $\Delta E_{1/2}$ value for **11** is twice as large as that for **10**. So the low–energy metal to S back bonding pathway is the main reason for the enhanced electronic communication by changing O to S atoms from **10** to **11**. Calculations on DFT level helped in the understanding of the electronic structure and UV–vis spectra and a 'hole hopping' mechanism for the strong communication in compound **11** is suggested.
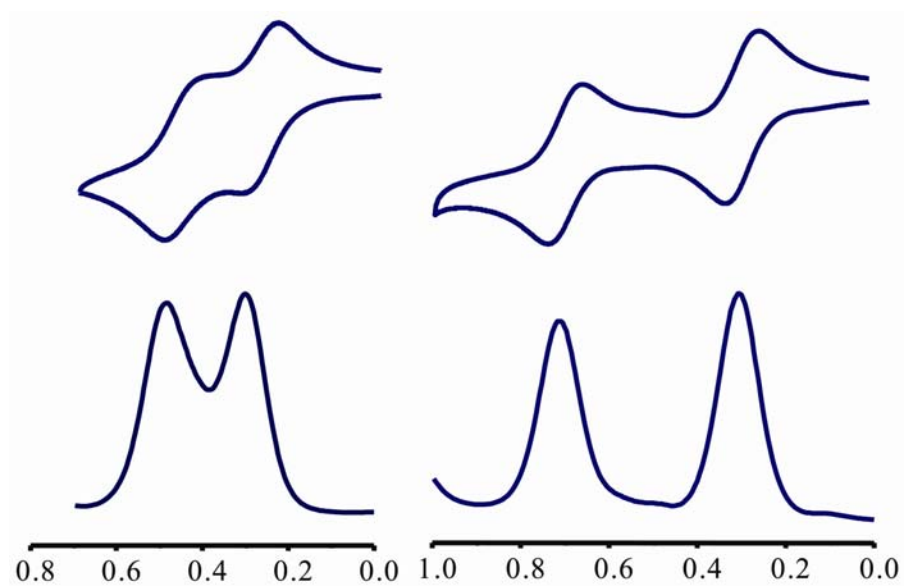
Figure 21. Cyclic voltammogram (with potentials vs Ag/AgCl) and differential pulse voltammogram (DPV) for **10** (left) and **11** (right) in CH_2Cl_2 solution.

Table 10. Comparison of electrochemistry data for compounds with two M_2 units (M = Mo and W) linked by related O and S donor containing bridges.

Compounds	$E_{1/2}(1)$ (mV)	$E_{1/2}(2)$ (mV)	$\Delta E_{1/2}$ (mV)	$K\text{c}$	Ref
$[(Bu^tCO_2)_3Mo_2]_2$ $(O_2CC_6H_4CO_2)$	0	NA	0	4	12(a)
$[(Bu^tCO_2)_3Mo_2]_2$ $(OSCC_6H_4CSO)$	0	184	184	1.3×10^3	14
$[(Bu^tCO_2)_3W_2]_2$ $(O_2CC_6H_4CO_2)$	−340	−180	160	5.1×10^2	12(a)
$[(Bu^tCO_2)_3W_2]_2$ $(OSCC_6H_4CSO)$	−78	−260	518	5.7×10^8	14
$[Mo_2(DAniF)_2]_2$ (oxamidate)	280	484	204	2.8×10^3	this work
$[Mo_2DAniF)_2]_2$ (dithiooxamidate)	294	701	407	7.6×10^6	this work

Electronic Structure and UV–vis Spectra. To gain an understanding of the electronic structure and different level of electronic interaction between the Mo_2 units in compounds **10** and **11**, a series of DFT calculations were performed on model compounds **10′** and **11′** with the anisyl groups replaced by H atoms.

Previous study on the substituted oxamidate linked compounds show that both steric and electronic interactions have influence on the stability of the α forms and it predicted that the unsubstituted oxamidate would prefer the planar conformation due to the minimal steric interactions. The optimized geometry for **10′** and **11′** is shown schematically in (a) compared to that of α form (b) (Scheme 9).

Scheme 9
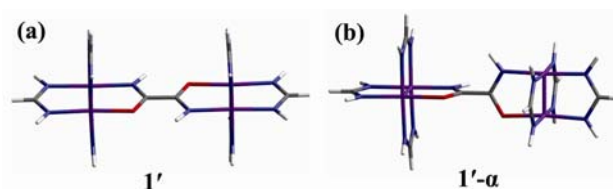
This is consistent with the crystal structures, which shows a planar conformation. Vibrational frequency analysis with the optimized geometry indicated that they were true minimum on the potential energy surface. The selected optimized geometry is summarized in Table 11. Although the calculated distances are generally slightly longer than those in crystal structures because of simplification that replaces the *p*–anisyl groups by less basic hydrogen atoms, there is close consistent between that observed experimentally and those calculated for the model compounds. For example, the calculated Mo–S distance 2.550 Å in **11′** is 0.046 Å longer than 2.154 Å of Mo–O bond

distance in **10′**, and the crystal structure shows a difference of 0.048 Å. The calculated

difference in the nonbonding distance between the dimetal units is 0.507 Å (7.609 Å for

10′ and 7.102 Å for **11′**), compared with 0.493 Å difference in crystal structures.

Molecular orbital analysis from DFT calculations provides valuable information on

the electronic structure of the two compounds. In both of the two models, the HOMO

and HOMO–1 are the in–phase ($\delta+\delta$) and out–of–phase ($\delta-\delta$) combinations of the δ

orbtials in Mo_2 units (Figure 22) and they are similar in shape. The splitting of the

HOMO and HOMO–1 to some extend is a measurement of the electronic coupling

between the Mo_2 units, the larger energy gap between the HOMO and HOMO–1, the

stronger the electronic communication (and vise versa). For example, the dimers of

dimolybdenum linked by dioxalene dianions have the strongest electronic

communication found so far ($Kc \sim 10^{12-13}$) and the energy difference between HOMO

and HOMO–1 is 0.98 eV, which is also the biggest number from DFT calculations. Here

the energy difference ΔE is 0.34 eV for model **10′** and 0.45 eV for model **11′**. The larger

energy gap between HOMO and HOMO–1 for model **11′** is consistent with the fact the

electrochemistry of compound **11** shows larger separation between the two redox–waves

than that of **10**. It is also found that similar to the $[(HCO_2)_3Mo]_2(X_2CC_6H_4CX_2)$

compounds (X = O or S), the energy of the HOMO decreases from –3.47 eV from **10′** to

–3.63 eV for **11′** by changing O atoms to S.[57] There is π–antibonding interaction

between the bridge π orbtal and the Mo_2 δ combination in HOMO. Chisholm and

coworkers have suggested that the π–donation of S $3p$ is less than O $2p$, which accounts

for the downward trend in energy of HOMO.[12(a)]

Table 11. Calculated Energies and Geometries for Models of **10′** and **11′**.

model	energy (a.u.)	HOMO (eV)	HOMO−1 (eV)	ΔE (eV)	Calculated bond lengths (Å) and angles (deg)				
					Mo–Mo	Mo$_2$···Mo$_2$	Mo–N (in DAniF)	Mo–N (in bridge)	Mo−O(S)
10′	−1504.2992	−3.47	−3.81	0.34	2.139	7.102	2.143	2.151	2.154
11′	−2150.2597	−3.63	−4.08	0.45	2.141	7.609	2.145	2.127	2.550

Table 12. Calculated Frontier MO Energies for the Models **10′** and **11′**.

frontier Orbitals	[(HNC(H)NH)$_2$Mo$_2$]$_2$(C$_2$O$_2$N$_2$H$_2$) (**10′**)		[(HNC(H)NH)$_2$Mo$_2$]$_2$(C$_2$S$_2$N$_2$H$_2$) (**11′**)	
	MO energy (ev)	Assignment	MO energy (ev)	Assignment
LUMO+5	0.3034	Mo$_4$ $\pi^*+\pi^*$	0.0726	Mo$_4$ $\pi^*+\pi^*$
LUMO+4	0.0871	Mo$_4$ $\delta^*-\delta^*$	−0.1233	Mo$_4$ $\delta^*-\delta^*$
LUMO+3	−0.0220	Mo$_4$ $\delta^*+\delta^*$	−0.2857	Mo$_4$ $\delta^*+\delta^*$
LUMO+2	−0.1910	Bridge π^*	−0.3494	Mo$_4$ $\sigma^*-\sigma^*$
LUMO+1	−0.2291	Mo$_4$ $\sigma^*-\sigma^*$	−0.3975	Mo$_4$ $\sigma^*+\sigma^*$
LUMO	−0.3020	Mo$_4$ $\sigma^*+\sigma^*$	−1.0374	Bridge π^*
HOMO	−3.4736	Mo$_4$ $\delta-\delta$	−3.6344	Mo$_4$ $\delta-\delta$
HOMO−1	−3.8129	Mo$_4$ $\delta+\delta$	−4.0754	Mo$_4$ $\delta+\delta$
HOMO−2	−5.0780	Ligand	−4.8721	Ligand
HOMO−3	−5.0965	Ligand	−5.0408	Ligand
HOMO−4	−5.5294	Mo$_4$ $\pi-\pi$	−5.4492	Ligand
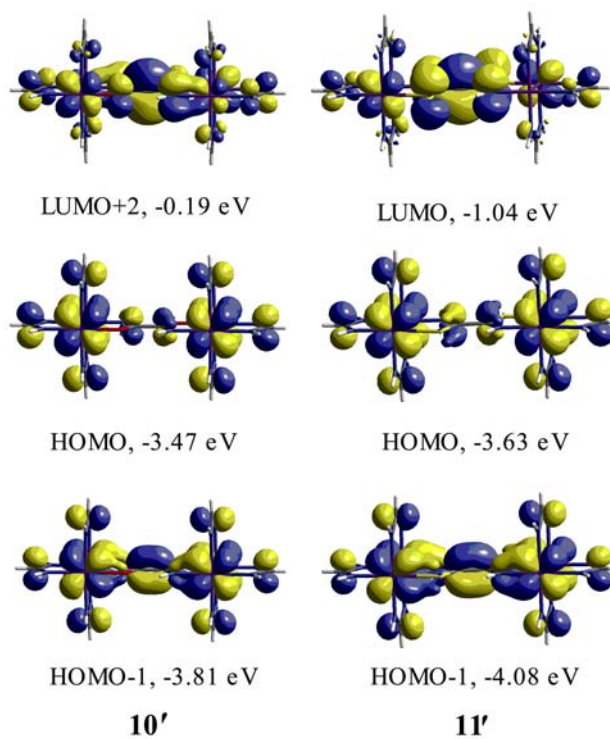
Figure 22. Illustration of the 0.02 contour surface diagrams for selected frontier orbitals of **10′** and **11′**. The HOMO and HOMO–1 for **10′** and **11′** are similar and are in–phase ($\delta+\delta$) and out–of–phase ($\delta-\delta$) combinations of the δ orbtials in Mo_2 units. The bridge π^* is LUMO+2 for **10′** and LUMO for **11′**.
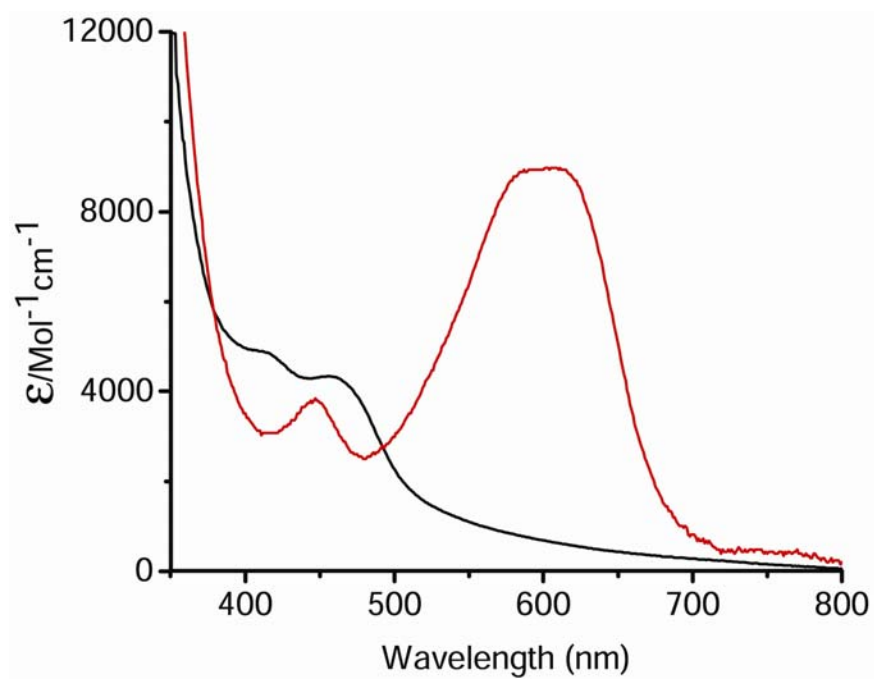
Figure 23. UV–vis spectra for compound **10** (black) and **11** (red) in CH_2Cl_2 solutions.

Although the HOMO and HOMO–1 are similar to each other for models **10′** and **11′**, there are important differences in their electronic structures. Selected energies of frontier MOs of the two models **10′** and **11′**, along with the main contributions are shown in Table 12. Specifically, the bridge π^* orbtal is LUMO+2 at –0.19 eV for **10′** compared to LUMO at –1.04 eV for **11′**. Two mechanisms for the electronic communication, 'electron hopping' and 'hole hopping' (Scheme 10) have been proposed for the dimer of dimers. The relative energy of bridge π^* and π orbtals to the Mo_2 δ combinations are critical in 'electron hopping' and 'hole hopping' pathways, respectively. For both of **10′** and **11′**, the bridge π orbital energies are far below the HOMO–1, and 'hole hopping' contribute very little to the electronic coupling.[58] The energy difference between the HOMO and bridge π^* are 3.28 eV and 2.59 eV for **10′** and **11′** accordingly. The energy for metal–S pathway is much lower than that for metal–O, which is attributed to the enhanced electronic coupling between dimetal centers.

Scheme 10

(a) electron hopping   (b) hole hopping
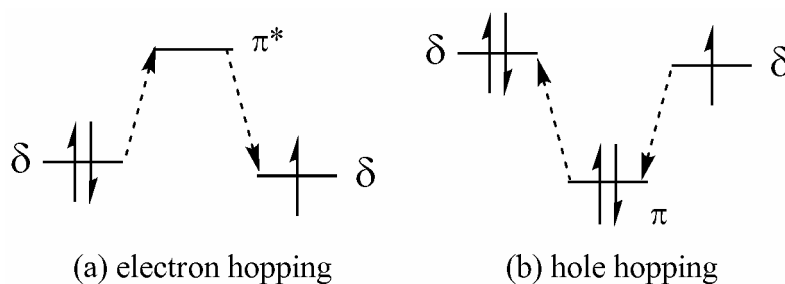
The closer energy gap between Mo_2 δ orbitals and the bridge π^* for **11′** are evidenced by the electronic spectra. The UV–vis spectrum of compound **10** shows two absorption bands at 412 and 460 nm (Figure 23). Time dependent DFT calculation

indicates that the absorption at 412 nm can be assigned to $\delta \rightarrow \delta$ transitions which rises from HOMO-1 to LUMO$+3$ ($\delta+\delta \rightarrow \delta+\delta$) and HOMO to LUMO$+4$ ($\delta-\delta \rightarrow \delta-\delta$), calculated at 459 nm. A similar $\delta \rightarrow \delta$ band was observed for compound **11** at 450 nm and calculated at 444 nm. The second absorption band for compound **10** at 460 nm can be assigned to the metal–to–ligand charge–transfer, which is HOMO$\rightarrow$LUMO$+2$ transition and calculated at 466 nm. For compound **11**, a much more intense band at lower energy, 600 nm, was observed and it is the HOMO$\rightarrow$LUMO or metal $\delta+\delta$ to bridge π^* transition, which is calculated at 571 nm. This intense metal–to–ligand charge–transfer band is attributed to the dark blue color of compound **11**. In both of compounds **11** and **12**, the electronic coupling is mainly through the parthway of 'electron hopping'. The Mo_2 to S electron hopping requires less energy than that for O, and this explains why the $^-HN(S)C–C(S)NH^-$ bridged compound **11** is so strongly coupled relative to the $^-HN(O)C–C(O)NH^-$ bridged compound **10**. A review of the available dimer of dimers suggests that, generally, for the similar systems with closely related structures, the lower the energy for the MLCT bands, the stronger the electronic coupling between the dimetal centers. For example, the compounds with uniquely strong electronic communication between dimetal centers linked by dioxolene dianions are green colored and show even lower energy MLCT bands in 1100 to 1200 nm with large extinction coefficient. The study on a similar system, $[Mo_2(O_2CBu^t))_3]^+$ and $[W_2(O_2CBu^t)_3]^+$ linked by oxalate or 3,6–dioxypyridazine, shows that the molybdenum compounds show the MLCT absorption band in UV–vis at 400–500 nm while the more strongly coupled tungsten compound show the MLCT bands at 700–800 nm.[14,58]

CHAPTER V

A TRANSITION FROM A NON–BONDING TO A BONDING INTERACTION

IN A TETRANUCLEAR [Mo$_2$]$_2$(μ–OR)$_4$ CLUSTER[*]

INTRODUCTION

Three types, **I**, **II** and **III** (Scheme 6)**,** of tetranuclear cluster containing dimolybdenum units have been synthesized, and the bridging groups, X, used in such molecules have been of considerable variety. In compounds of type **I**, two quadruple bonds have undergone [2 + 2] cycloaddition to form a metallocyclobutadiyne ring by cleaving the δ bonds and then forming two σ bonds between the two dimolybdenum pairs. When the separation between the two dimetal units is large, the loss of delta bonding to give two new single bonds does not occur, and a molecule of type **II** is obtained. Recent studies on the type **III** compounds bridged by halides show that the Mo$_2$ units are strongly coupled, although there is no direct bond between them. For example, [Mo$_2$(*cis*–DAniF)$_2$]$_2$(μ–Cl$_4$) has a large $\Delta E_{1/2}$ value of 540 mV, which corresponds to a comproportionation constant of 1.3×10^9.[23] Because of the large comproportionation constant, oxidation of the neutral precursor gives a mixed–valence complex with the unpaired electron delocalized over all four Mo atoms. It should be noted that the metal to

ligand back bonding mechanism proposed for [Mo$_2$]L[Mo$_2$] compounds may not applicable to the halide system. Because of the very short metal to metal separation, direct head to head interaction between the two δ orbitals is the more likely cause of the strong coupling. This hypothesis led us to the two general objectives for the present work: (1) to extend the study on electronic interaction with this unusual coupling system, and (2) to explore approaches other than [2 + 2] cycloaddition to make a transition from non–bonding to bonding interaction in rectangular Mo$_4$ clusters.

Here we report a series of compounds $\{[Mo_2(cis–DAniF)_2]_2(\mu–OCH_3)_4\}^{n+}$, $n = 0$ (**13**), 1 (**14**) and 2 (**15**), as well as an ethoxide analogue of **13** (**16**). All of these compounds have been characterized structurally and by various spectroscopic techniques and by DFT calculations. There is a decrease of the dimetal separation as **13** is oxidized to **14** and then to **15** which suggests bond formation between dimetal centers that reduces the bond order between the species that initially had a quadruple bond.

EXPERIMENTAL SECTION

Materials and Methods. The starting material, $[Mo_2(cis–DAniF)_2(NCCH_3)_4](BF_4)_2$ was prepared following reported procedures.[59] The details of calculation methods have been shown in the previous chapter.

Preparation of $[Mo_2(cis–DAniF)_2]_2(\mu–OCH_3)_4$, 13. To a solution of $[Mo_2(cis–DAniF)_2(NCCH_3)_4](BF_4)_2$ (416 mg, 0.400 mmol) in 20 mL of methanol was added slowly, and with stirring, 2.0 mL of a 0.50 M solution of $NaOCH_3$ in methanol. A brown precipitate formed immediately. This reaction mixture was stirred at ambient temperature for 1 h. After the supernatant solution was decanted, the remaining solid was washed with methanol (2 × 15 mL) and briefly dried under vacuum. The dry solid was dissolved in 15 mL of dichloromethane. After passing the mixture through a Celite–packed frit, the filtrate was layered with methanol. Red–brown needle crystals formed in seven days. Yield: 180 mg (59%). ^{1}H NMR (δ, ppm in CDCl$_3$) at −50 ºC: 8.82(s, 4H, –NCHN–), 6.62 (m, 32H, aromatic C–H), 4.26 (s, 12H, –OCH_3), 3.73 (s, 24H, –CH_3 in DAniF). UV–Vis, λ_{max} nm (ε, $M^{-1}·mol^{-1}$): 500 (1.1×10^3), 420 (6.3×10^2). Anal. Calcd for $C_{64.75}H_{73.5}Mo_4N_8O_{12}Cl_{1.5}$ (13·0.75CH$_2$Cl$_2$): C, 48.75; H, 4.62; N, 7.05. Found: C, 48.88; H, 4.36; N, 7.14.

Preparation of $\{[Mo_2(cis–DAniF)_2]_2(\mu–OCH_3)_4\}PF_6$, 14. Solutions of **13** (204 mg, 0.134 mmol in 10 mL of CH$_2$Cl$_2$) and ferrocenium hexafluorophosphate (44 mg, 0.134 mmol in 10 mL of CH$_2$Cl$_2$) were prepared separately and cooled to −78 º C. The solution of $[FeCp_2]PF_6$ was transferred to the solution of $[Mo_2(cis–DAniF)_2]_2(\mu–OCH_3)_4$ using a cannula. The resulting dark brown mixture was stirred at low temperature for 30 min,

and then 40 mL of pre–cooled hexanes were added to precipitate a dark brown solid. After the yellow supernatant solution was decanted, the solid was washed with cooled hexanes (2 × 15 mL) and then dried under vacuum. The dry solid was dissolved in 15 mL of dichloromethane in a Schlenk tube, and the solution was layered with hexanes. Dark–brown needles formed in about one week. Yield: 182 mg (81%). UV–Vis, λ_{max} nm (ε, $M^{-1}\cdot mol^{-1}$): 490 (2.5 × 10³). Anal. Calcd for $C_{65}H_{74}F_6Mo_4N_8O_{12}PCl$ (**14**·CH_2Cl_2): C, 44.38; H, 4.24; N, 6.37. Found: C, 44.18; H, 3.81; N, 6.31.

Preparation of {[Mo₂(*cis*–DAniF)₂]₂(μ–OCH₃)₄}(BF₄)₂, 15. The preparation was similar to that for **14** but 2 equiv of oxidizing reagent [Cp₂Fe]BF₄ were used. For a reaction starting with **13** (152 mg, 0.100 mmol), the yield of dark crystals was 96 mg (60%). ¹H NMR (δ, ppm in CDCl₃) at −50 ºC: 9.44 (s, 4H, –NC*H*N–), 6.89(d, 16H, aromatic C–*H*), 6.69 (d, 16H, aromatic C–*H*), 4.20 (s, 12H, –OC*H*₃), 3.73 (s, 24H, –C*H*₃ in DAniF). UV–Vis, λ_{max} nm (ε, $M^{-1}\cdot mol^{-1}$): 790 (6.4 × 10²), 580 (1.3 × 10³). Anal. Calcd. for $C_{65.5}H_{75}B_2F_8Mo_4N_8O_{12}Cl_3$ (**15**·1.5CH_2Cl_2): C, 42.99; H, 4.13; N, 6.12. Found: C, 43.39; H, 3.63; N, 5.72.

Preparation of [Mo₂(*cis*–DAniF)₂]₂(μ–OC₂H₅)₄, 16. A procedure similar to the one described for **13**, with the same reaction scale as above, was employed for the preparation of the ethoxide analogue. For this reaction, ethanol was used instead of methanol. Yield: 160 mg (51%). UV–vis, λ_{max} nm (ε, $M^{-1}\cdot mol^{-1}$): 500 (5.9 × 10³), 425 (1.0 × 10²). Anal. Calcd for $C_{69}H_{82}Mo_4N_8O_{12}Cl_2$ (**16**·CH_2Cl_2): C, 49.62; H, 4.95; N, 6.71. Found: C, 49.71; H, 4.85; N, 6.94.

RESULTS AND DISCUSSION

Syntheses. Compounds **13** and **16** have been prepared by direct assembly of the building block precursor $[Mo_2(cis–DAniF)_2(CH_3CN)_4]_2(BF_4)_2$ with the corresponding bridging ligands, as described by the following equation.

$$2[Mo_2(cis–DAniF)_2(NCCH_3)_4](BF_4)_2 + 4NaOCH_3$$

$$\xrightarrow{\text{ROH}} [Mo_2(cis–DAniF)_2]_2(\mu–OR_4) + 4NaBF_4 + 8NCCH_3$$

$$R = CH_3 \text{ for } \textbf{13} \text{ and } C_2H_5 \text{ for } \textbf{16}$$
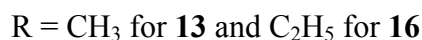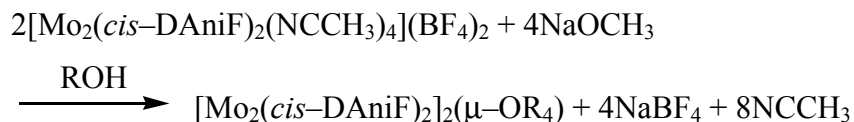
This procedure is straightforward and appears to be applicable to the preparation of analogous compounds simply by changing the bridging ligand. For example, the halide bridged compounds $[Mo_2(cis–DAniF)_2]_2(\mu–X_4)$ (X = Cl and I) were first prepared by a complicated and time–consuming procedure. Using the designed building block $[Mo_2(cis–DAniF)_2(NCCH_3)_4]_2(BF_4)_2$, the neutral compounds of type **III** with varying bridging ligands can be prepared by the direct assembly reaction described in Scheme 11 below.

Scheme 11
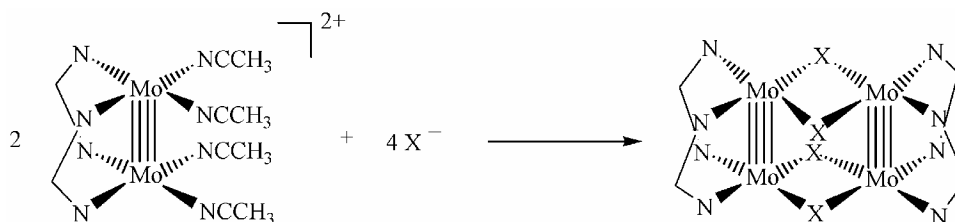
For the preparation of **13** and **16**, the use of alcohol as solvent is very important since it provides an additional driving force for the reaction because of the low solubility of neutral product in such a polar solvent. In the case of **16**, ethanol is the source of the

bridging ligand ethoxide. The use of alcohol consisting of the same R group as the bridging ligands benefits the formation of the product and delays hydrolysis. Therefore, this preparative route provides a general method for the preparation of analogous alkoxide bridged Mo_4 clusters by changing the alcohol used as a solvent. It is very important to maintain rigorously water–free conditions because competition of hydroxide for the bridging positions will result in partially OH^- substituted product. Pure products were obtained only by using freshly distilled alcohols to which sodium metal had been added to form the corresponding sodium alkoxides.

The oxidized compounds **14** and **15** were prepared by oxidation of the neutral compound **13** using salts containing the mild oxidant ferrocenium cation but carefully controlling the reaction stoichiometries. The CV and DPV in CH_2Cl_2 solution for compound **13** show two reversible waves with a large separation $\Delta E_{1/2}$ of 554 mV. For such a strongly coupled system, the mixed–valence complexes $\{[Mo_2(cis–DAniF)_2]_2(\mu–X_4)\}^+$, e. g., **14**, are expected to be thermodynamically stable. For the halide bridged compounds the second redox potential of about 800 mV (vs Ag/AgCl) was far beyond the oxidizing capability of Cp_2Fe^+, but replacement of X by OR lowers the oxidation potentials by about 600 mV so that the doubly oxidized compound **15** can be prepared using the ferrocenium containing reagents. This simplifies the treatment of the reaction mixture because the reduced by–product, ferrocene, can be easily removed by washing with hexanes. Since the precursor **13** is very sensitive to air and moisture, the oxidation reactions were carried out at low temperature and handled with great care.

Structural Results. Compounds **13**, **14**, **15** and **16** have been structurally characterized by single crystal X–ray diffraction. Crystallographic data are given in Table 13.The core structures for these molecules are shown in Figures 24-27. A common structural feature for these compounds is the presence of four oxygen atoms from the four alkoxide anions that bridge two parallel, DAniF–supported Mo_2 units. Such an arrangement produces a rectangular Mo_4 cluster of type **III**. This structural motif is shared by the three halide–bridged compounds $[Mo_2(cis–DAniF)_2]_2(\mu–X_4)$ (X = Cl and I). These structures must not be confused with those previously reported compounds that also contain rectangular molybdenum quartets, but which must be called metallacyclobutadiynes.

The structures of the two neutral molecules **13** and **16** are very similar, and have almost identical Mo−Mo, 2.132(1) Å, and other bond distances, in spite of the differences in the OR groups. These distances are long when compared to those in other compounds containing Mo_2^{4+} units. In paddlewheel compounds, e. g., $Mo_2(O_2CCH_3)_4$ and $Mo_2(DAniF)_4$, the Mo−Mo distances are usually in the range of 2.08 ~ 2.10 Å. The halide bridged dimolybdenum diads $[Mo_2(cis–DAniF)_2]_2(\mu–X_4)$ (X = Cl, Br and I), which are close analogues of these alkoxo compounds, have metal−metal bond distances of about 2.120 Å. Two other species that have an Mo_2^{4+} unit supported by two *cis* bridging ligands and long Mo−Mo quadruple bonds are $[Mo_2(cis–DAniF)_2(CH_3CN_{eq})_4(CH_3CN_{ax})_2]^{2+}$ (2.143 Å) and $[Mo_2(cis–O_2CH_3)_2(CH_3CN_{eq})_4(CH_3CN_{ax})_2]^{2+}$ (2.134 Å).[60] For the latter, axial ligands are probably responsible for the long Mo−Mo bond distances.

Table 13. X–ray Crystallographic Data for **13**, **14**, **15** and **16**.

Compound	$13 \cdot 3CH_2Cl_2$	$14 \cdot 2CH_2Cl_2$	$15 \cdot 2CH_2Cl_2$	$116 \cdot 2CH_2Cl_2$
empirical formula	$C_{67}H_{78}Cl_6Mo_4N_8O_{12}$	$C_{66}H_{76}Cl_4PF_6Mo_4N_8O_{12}$	$C_{66}H_{76}Cl_4B_2F_8Mo_4N_8O_{12}$	$C_{70}H_{84}Cl_4Mo_4N_8O_{12}$
Fw	1783.83	1843.33	1872.53	1755.01
space group	$P\bar{1}$ (No. 2)	$P\bar{1}$ (No. 2)	$P\bar{1}$ (No. 2)	$P\bar{1}$ (No. 2)
a, Å	10.3113(8)	10.067(2)	9.962(1)	10.4659(1)
b, Å	15.031(1)	12.042(3)	18.083(3)	14.7445(2)
c, Å	24.154(2)	15.385(3)	21.830(4)	14.9192(2)
α, deg	86.840(2)	89.052(4)	99.415(3)	104.812(2)
β, deg	86.569(1)	78.797(4)	92.164(3)	106.064(2)
γ, deg	89.542(2)	82.177(4)	103.810(4)	108.693(2)
V, Å^3	3731.2(5)	1812.5(7)	3755.5(1)	1939.9(4)
Z	2	1	2	1
T, K	213	213	213	213
λ, Å	0.71073	0.71073	0.71073	0.71073
d_{calcd}, g/cm^3	1.588	1.689	1.656	1.502
μ, mm^{-1}	0.934	0.926	0.878	0.831
R1^a (wR2^b)	0.0594(0.1430)	0.0395(0.0834)	0.0899(0.1645)	0.0426(0.1120)

^{a} R1 $= \Sigma \|F_o| - |F_c\| / \Sigma |F_o|$. ^{b} wR2 $= [\Sigma[w(F_o^2 - F_c^2)^2]/ \Sigma[w(F_o^2)^2]]^{1/2}$

Table 14. Selected Bond Distances (Å) and Angles (deg) for Some $[Mo_2]_2(\mu-X)_4$ Compounds

Compound	Charge	Mo─Mo	$Mo_2\cdots Mo_2$	Mo─X	Mo─N	Mo─X─Mo
13 (X = OMe)	0	2.1315(7)	3.245	2.142[4]	2.121[5]	98.55[16]
14 (X = OMe)	+1	2.1493(6)	3.100	2.105[1]	2.104[2]	94.81[7]
15 (X = OMe)	+2	2.1779(7)[a]	2.945	2.073[5]	2.106[5]	90.40[16]
16 (X = OEt)	0	2.1317(4)	3.241	2.136[2]	2.120[4]	98.67[9]
X = Cl	0	2.1191(4)	3.601	2.516[2]	2.095[5]	91.42[5]
X = Cl	+1	2.1453(3)	3.374	2.490[6]	2.083[3]	85.28[1]
X = Br	0	2.1181(6)	3.697	2.649[2]	2.093[5]	88.50[2]
X = Br	+1	2.1406(9)	3.488	2.622[2]	2.091[4]	83.38[2]
X = I	0	2.117(1)	3.915	2.845[2]	2.100[6]	87.02[2]
X = I	+1	2.144(1)	3.632	2.812[2]	2.104[9]	80.50[4]
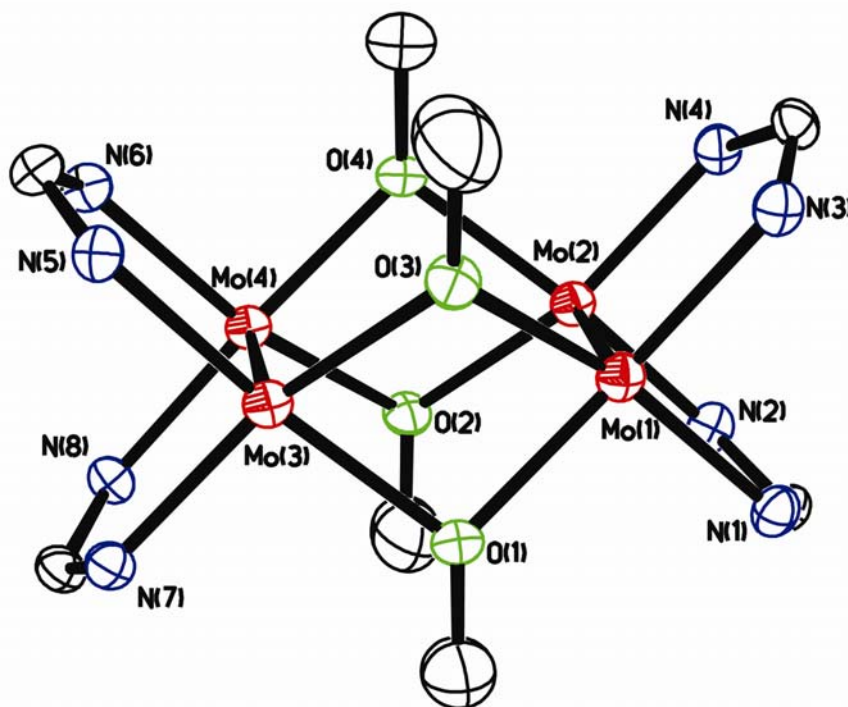
Figure 24. Core structure of **13** with displacement ellipsoids drawn at the 40% probability level. All *p*–anisyl groups and hydrogen atoms have been omitted for clarity.
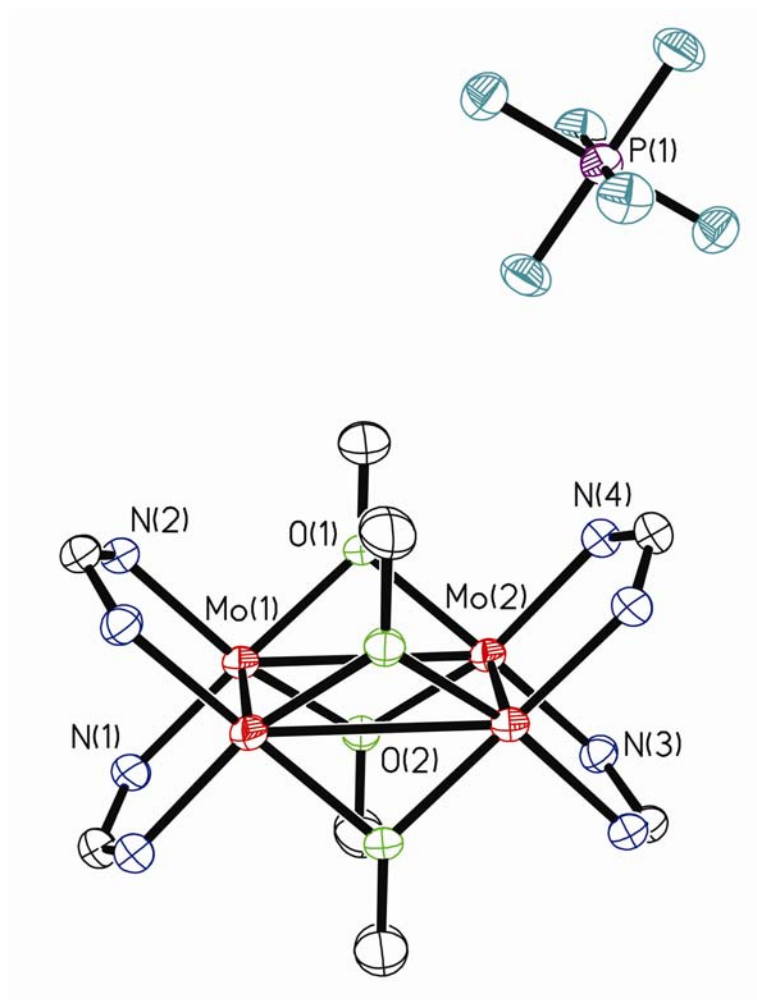
Figure 25. Core structure of **14** with displacement ellipsoids drawn at the 40% probability level. All *p*–anisyl groups and hydrogen atoms have been omitted for clarity.
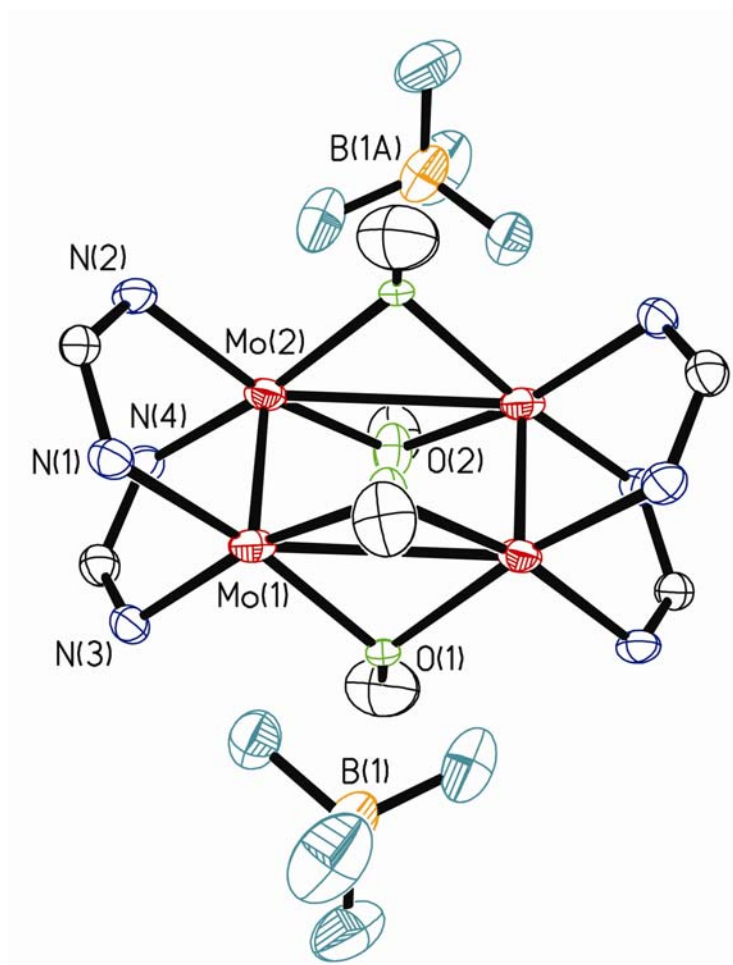
Figure 26. Core structure of **15** with displacement ellipsoids drawn at the 40% probability level. All *p*–anisyl groups and hydrogen atoms have been omitted for clarity.
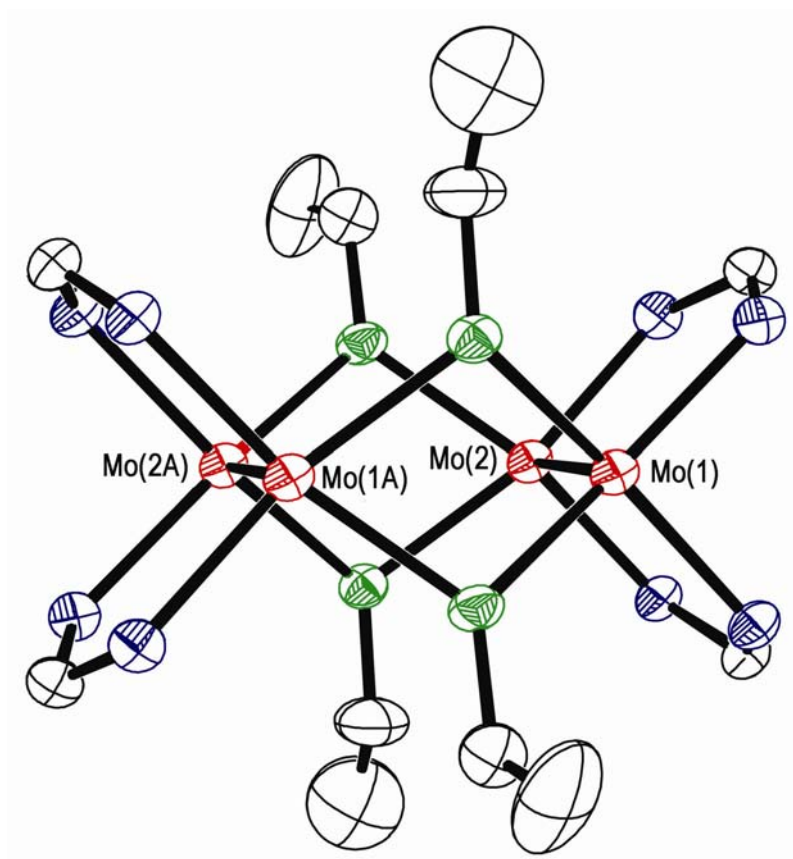
Figure 27. Core structure of **16** with displacement ellipsoids drawn at the 40% probability level. All *p*–anisyl groups and hydrogen atoms have been omitted for clarity.

A striking structural feature of **13** and **16** is the short non–bonding separation between the midpoints of the quadruply bonded units, ca. 3.24 Å, which is the shortest observed among compounds having two linked Mo_2^{4+} units. This separation is even shorter than that in the hydride linked compound $[Mo_2(DAniF)_3]_2(\mu–H)_2$ (3.54 Å), in which a bonding interaction between the dimetal units has been suggested by DFT calculations.[34] As shown in Table 14, in the halide bridged analogues, the two Mo_2^{4+} units are separated by 3.60 ~ 3.92 Å. Structural differences between the alkoxide– and halide–bridged families are also noted in the Mo−X−Mo angles. For **13** and **16**, all Mo−O−Mo angles are obtuse (ca. 98.5 ~ 98.6°); in contrast, the Mo−X−Mo angles (X = Cl, Br and I) are close to a right angle (range from 87.0 to 91.4°). For any given M−X bond distance, the geometric consequence of enlarging the bridging angles should be an increase in the separation between the bridged dimetal units, but the Mo−O bonds are much shorter than the Mo−X bonds.

The ^{1}H MNR spectrum of **13** at −50 °C in CDCl$_3$ shows that the molecular structure of **13** is retained in solution. A "doublet of doublets" at 6.57 ~ 6.66 ppm is attributed to the aromatic protons from the DAniF ligands and the singlet at 8.82 ppm corresponds to the chemically equivalent methine protons. All bridging methoxy groups are equivalent as are the methoxy groups from the anisyl groups. These resonances are consistent with the D_{2h} symmetry of the molecule in solution. At room temperature, the peak for methine protons broadens and essentially disappears, and the signals for the aromatic DAniF protons appear as a broad band at 6.6 ppm. This is consistent with a fluxional process in solution. Similarly, for compound **16** there are sharp signals in the low

temperature spectrum that become broad at ambient temperature but the spectrum is complex in the alkyl region. In **16**, the four ethyl groups are embedded between two $[Mo_2(cis–DAniF)_2]^{2+}$ units and rotations about the O−C bonds are sterically blocked. There are steric repulsions between methyl groups of the two ethoxide groups on the same side of the rectangular plane defined by the four Mo atoms which generate four possible conformational isomers as shown in Scheme 12. Indeed some of the fluxional behavior suggested by the ^1H NMR spectrum in $CDCl_3$ is consistent with the existence of conformational isomers.

Scheme 12

D_{2h}

C_s

C_{2v}

C_{2h}
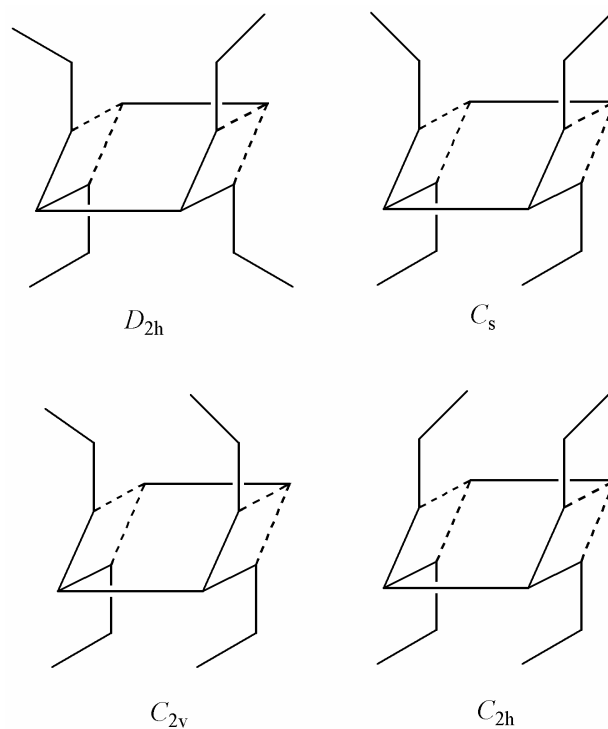
Removal of one electron from **13** gives the complex cation in **14** shown in Figure 25. Upon oxidation, the Mo−Mo bond distances are lengthened from 2.1315(7) Å in the precursor to 2.1493(3) Å (Table 14), which is consistent with an electron being removed from a bonding orbital delocalized over the dimetal units and a decrease of 0.25 in each bond order. The increase of 0.018 Å in the Mo−Mo bond distance in going from **13** to **14** is similar to those observed in other delocalized situations but considerably less than that found in localized mixed–valence complexes $[Mo_2]^{1+}L[Mo_2]^0$. Accompanying the lengthening of the metal─metal bond, the $Mo_2 \cdots Mo_2$ distance is reduced from 3.245 to 3.100 Å and the average bridging angles Mo−O−Mo (ca. 94.81°) become slightly smaller than those in **13** (ca. 98.55°). Similar changes have been observed in $[Mo_2(cis–DAniF)_2]_2(\mu–X_4)$ (X = Cl, Br and I) compounds as one electron is removed from the neutral complexes. The metal─ligand bond distances are shortened, for example, from 2.142[4] to 2.105[1] Å for Mo−$O_{alkoxide}$ and for 2.121[5] to 2.104[2] Å for Mo−N_{DAniF} because of the increase in oxidation number of the dimetal units.

The dication **15** is unique in that it is the first $Mo_4(\mu–X)_4$ cluster that has two Mo_2^{5+} units. There are two crystallographically independent molecules in the unit cell. In one of them, a BF_4 anion is at a distance of 2.547 Å from an Mo atom while in the other species the cation is devoid of close interactions with the anions. However, the Mo−Mo and other bond distances are similar. As shown in Table 14, the Mo−Mo bond distances further increase upon removal of the second electron. The lengthening of the Mo−Mo bond distances, 0.029 Å from 2.1493(6) in **14** to 2.1779(7) Å in **15**, is significantly larger than that from **13** to **14** (0.018 Å). As an additional one electron oxidation occurs,

the two [Mo_2] units get even closer as the $Mo_2 \cdots Mo_2$ separation decreases from 3.100 in

14 to 2.945 Å; the Mo–O–Mo angles are also reduced to 90.40° from 94.81°. Again,

these changes are greater than those observed as one electron is removed from **13**. The

second oxidation appears to have a direct and significant impact on the electronic

configuration of the cluster. It is particularly important to note that shortening of the

$Mo_2 \cdots Mo_2$ separations occurred even though there are two positively charged [Mo_2]

units separated by a very short distance (2.945 Å). Such shortening cannot be attributed

solely to small geometric changes arising from a slight decrease of the Mo–O distances

(0.03 Å) from **14** to **15** (Table 14). In contrast, an increase in electrostatic repulsion

between two linked Mo_2^{5+} units is known to lead to an increase in the dimetal separation

in an electron localized complex system.

It also should be noted that many rectangular Mo_4 clusters characterized as

metallocyclobutadiynes have short distances between two dimolybdenum units (about

2.9 Å), which have been associated with metal–metal single bonds along the long edges

of the rectangle. For **15**, the metal–metal separation, 2.945 Å, is very close to that for the

long edges in such metallacyclobutadiynes. The Mo–Mo bond lengths of 2.1779 Å (i.e.,

the short edges of **15**) are exceptionally long and much longer than those in the

compounds with an Mo_2^{5+} core. The remarkable variations in structural parameters from

13 to **15** are consistent with a bonding interaction between the two Mo_2 units being

formed as the bond order of each Mo_2 unit decreases. A better understanding of the

electronic configuration of **15** from theoretical work will be described below.

The ^{1}H MNR spectrum of **15** at −50 °C in CD$_3$Cl closely resembles that of the neutral precursor **13**. The spectrum shows two "doublets" centered at 6.69 and 6.89 ppm which are attributed to the aromatic protons in the DAniF ligands and a singlet at 9.44 ppm for the chemically equivalent methine protons. The signals for methyl groups from the methoxy linker and those from the DAniF ligands are at 4.20 and 3.73 ppm, respectively. As in **13** the signals for the methine and linker protons coalesce at room temperature because of a dynamic process that takes place in solution. The sharp signals in the low temperature spectra as well as the position of the resonances suggest that **15** has a diamagnetic ground state.

Electrochemistry and Electronic Communication. Because of the short separation between the two bridged dimolybdenum units, a strong metal to metal electronic coupling interaction would be anticipated, and, for **13** and **16** electrochemical measurements (Figure 28) show two successive one–electron oxidations separated by large $\Delta E_{1/2}$ values of 554 and 587 mV, respectively. These electrochemical data along with those for [Mo$_2$(*cis*–DAniF)$_2$]$_2$(µ–X)$_4$ compounds are listed in Table 15, together with the comproportionation constants derived from the formula Kc $= $ e$^{\Delta E_{1/2}/25.69}$. Table 15 shows that the alkoxide bridged compounds exhibit significantly more negative potentials than the halide bridged analogues. The highly basic $^-$OR groups are responsible for such a shift in electrode potentials. A similar effect has been observed when comparing [Mo$_2$]O$_2$EO$_2$[Mo$_2$] compounds (E $=$ S, Mo and W) with their structural analogues [Mo$_2$](OCH$_3$)$_2$M(OCH$_3$)$_2$[Mo$_2$] (M $=$ Zn and Co). The exceptionally large

values of $\Delta E_{1/2}$ and Kc suggest that the mixed–valence species **14** is thermodynamically stable.

For many cases in which the two metal redox sites are bridged by a polydentate ligand, back bonding from metal to ligand is considered to be the major pathway that permits communication between the two metal centers. Our studies on a variety of complexes with two [Mo$_2$] units linked by a conjugated organic ligand have revealed that strong electronic coupling interaction entails an efficient metal (δ)–ligand (π^*) orbital interaction. Such a pathway is not available for [Mo$_2$]X$_4$[Mo$_2$]–type compounds. For **13** and **16** the very short metal–metal separation must be an important factor in the increased coupling effect, most likely by a direct δ to δ orbital interaction between the two dimetal centers (vide infra).
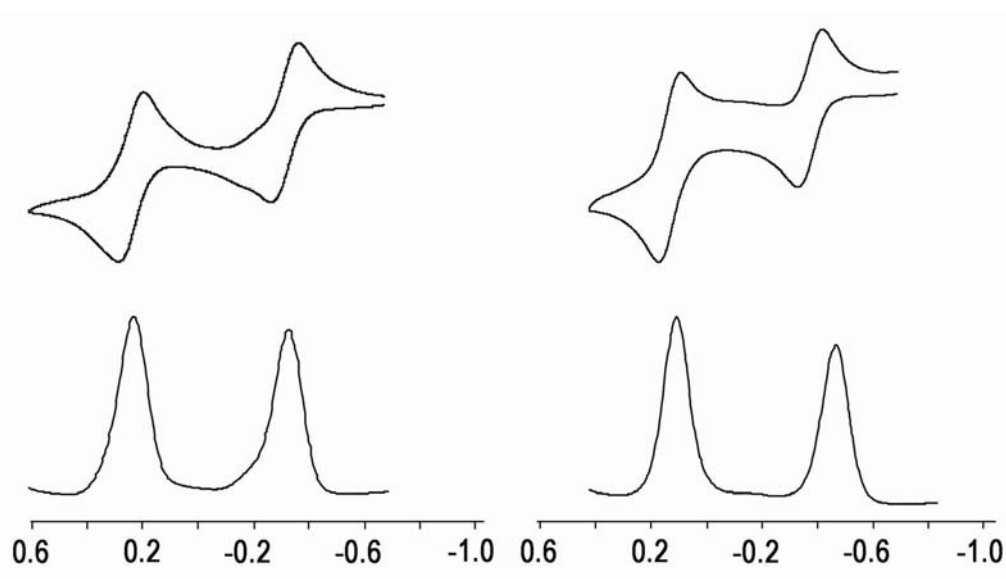
Figure 28. Cyclic voltammogram (with potentials vs Ag/AgCl) and differential pulse voltammogram (DPV) for **13** (left) and **16** (right) in CH$_2$Cl$_2$ solution.

Table 15. Electrochemical Data for $[Mo_2(DAniF)_2]_2(\mu-X_4)$ Compounds.

X	$Mo_2{\cdots}Mo_2$ (Å)	$E_{1/2}(1)$ (mV)	$E_{1/2}(2)$ (mV)	$\Delta E_{1/2}$ (mV)	K_c	Ref
OMe	3.245	−338	216	554	2.3×10^9	this work
OEt	3.241	−418	169	587	8.4×10^9	this work
Cl	3.601	260	800	540	1.3×10^9	23(a)
Br	3.697	314	813	499	2.7×10^8	23(b)
I	3.915	350	790	440	2.7×10^7	23(b)

Magnetism and near–IR Spectra. The X–band EPR spectrum for **14** measured in CH_2Cl_2 at room temperature is shown Figure 29 along with the measurement of the doubly oxidized compound **15**. For the singly oxidized species **14**, the g value of 1.922, which is significantly lower than that for a free radical, indicates that the unpaired electron resides in an orbital that is mainly metal–based. The prominent symmetric peak is due to molecules containing only the ^{96}Mo ($I = 0$) isotope (about 74% in abundance), whereas the small peaks flanking around the main signal are assignable to hyperfine structure from the ^{95,97}Mo ($I = 5/2$) isotopes with natural abundance of about 25%. Compound **15**, which forms upon removal of two electrons from **13**, is diamagnetic as suggested by the sharp ^{1}H NMR signals and is EPR silent. The diamagnetism in **15**, in which there are, formally, two Mo_2^{5+} units, each having an unpaired electron, is caused by antiferromagnetic coupling.

The Near–IR spectrum of **14** in CH_2Cl_2 solution measured in the region from 4000 to 10000 cm^{-1} (Figure 30) shows two intense absorption bands centered at 5900 (v_1) and 7900 cm^{-1} (v_2). Such transitions are often referred to as intervalence charge transfer transitions. However, the spectrum of **14** is qualitatively different from those for the [Mo$_2$]L[Mo$_2$] systems, for which only one band has been observed in the near–IR spectra.[61]   Compounds **13** and **15** do not show bands in the near–IR region.
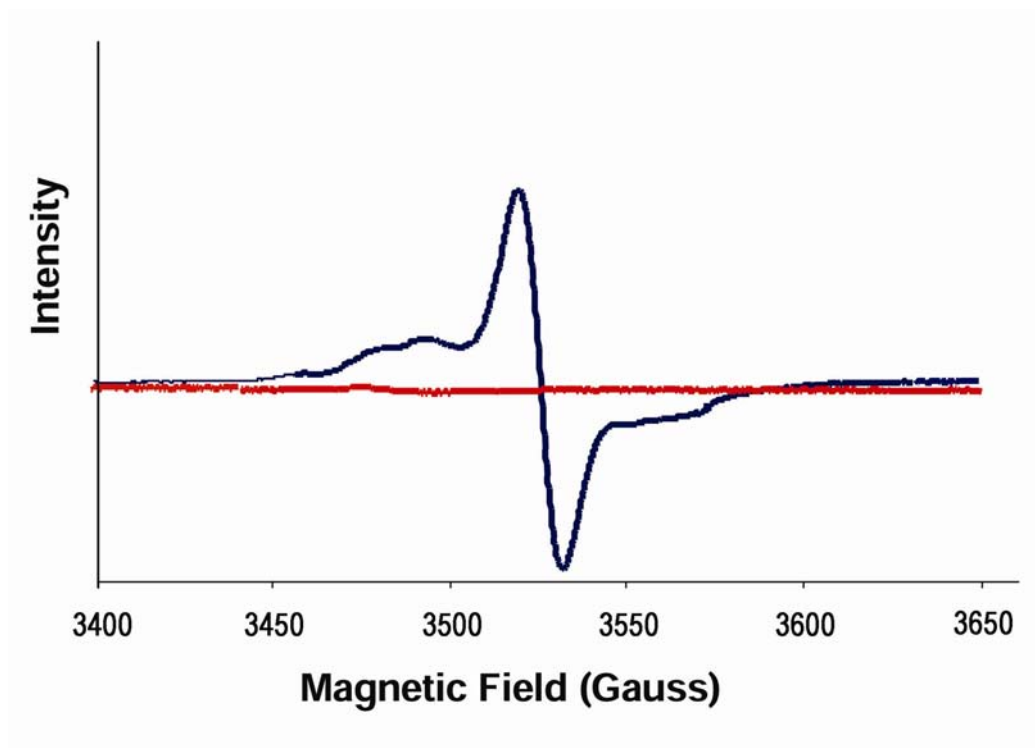
Figure 29. X–band EPR spectra of **14** (blue) and **15** (red) in CH_2Cl_2 solution at room temperature.
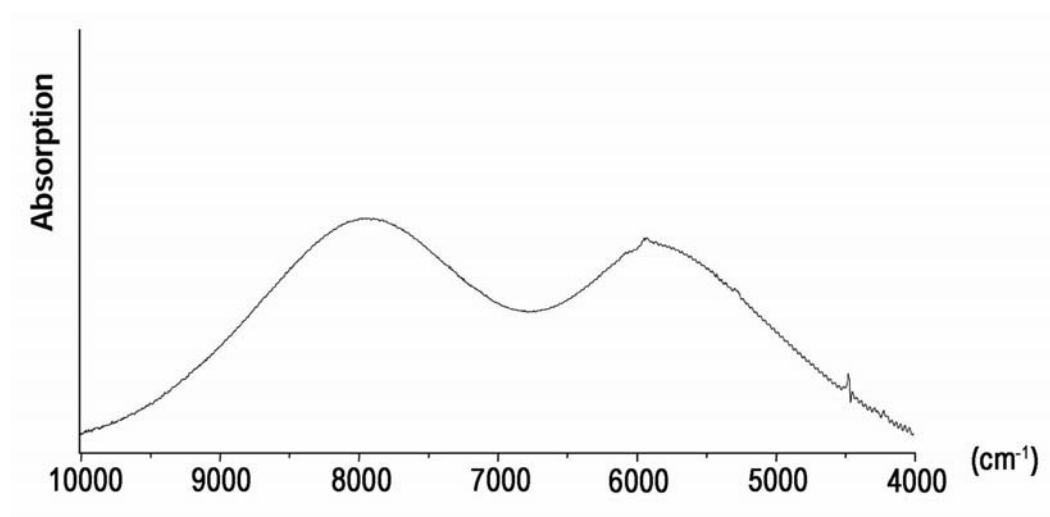
Figure 30. Near–IR spectrum of the mixed–valence species **14** in CH_2Cl_2 solution.

DFT Calculations and Electronic Structure. A series of Density Functional Theory calculations were performed on the models [(HNC(H)NH)$_2$Mo$_2$]$_2$(μ–OCH$_3$)$_4{}^{n+}$ (n = 0, 1, 2), in which the aryl groups of the formamidinate ligands were replaced by hydrogen atoms. This simplified structural model has been used successfully in similar systems.

The geometries from the crystal structures of compounds **13**, **14** and **15** were used as the starting parameters for the geometry optimization of the corresponding models. Relevant geometric and energy data obtained from the calculations are shown in Table 16. In general, the calculated Mo−Mo distances are slightly longer than the experimental values (ca. 0.04 Å), which is reasonable because in the models, the *p*–anisyl groups were replaced by less basic hydrogen atoms. All changes in bonds distances and angles resulting from removal of electrons are in good agreement with those from X–ray crystallography. The calculated distance between the two dimetal units decreases by 0.14 Å from **13** to **14**, and then by 0.17 Å from **13** to **14**; these changes are comparable with the experimental changes which are 0.14 Å and 0.16 Å, respectively.

The frontier orbital interactions between the Mo$_2$ units and the bridging ligands are shown in Figure 31. For the model of **13**, the HOMO results from the interaction of the out–of–phase orbital of the Mo$_2$ units (δ–δ) with the symmetry related combination of ligand orbitals (b_{3u}), and the HOMO−1 results from the interaction of the in–phase orbitals (δ+δ) with the matching combination of ligand orbitals (a_g). These two MOs both have large metal characters: 76.7% for the HOMO and 92.5% for the HOMO−1. As

Table 16. Calculated Data from DFT for Models of **13**, **14** and **15**

model	charge	total spin, S	energy (a.u.)	calculated bond lengths (Å) and angles (deg)			
				Mo–Mo	Mo$_2$···Mo$_2$	Mo–O	Mo−O−Mo
13	0	0	−1328.5858	2.173	3.333	2.169	100.32
14	+1	1/2	−1328.4226	2.191	3.192	2.142	96.26
15	+2	0	−1328.1275	2.210	3.019	2.112	91.10
		1	−1328.1241	2.206	3.313	2.145	101.02
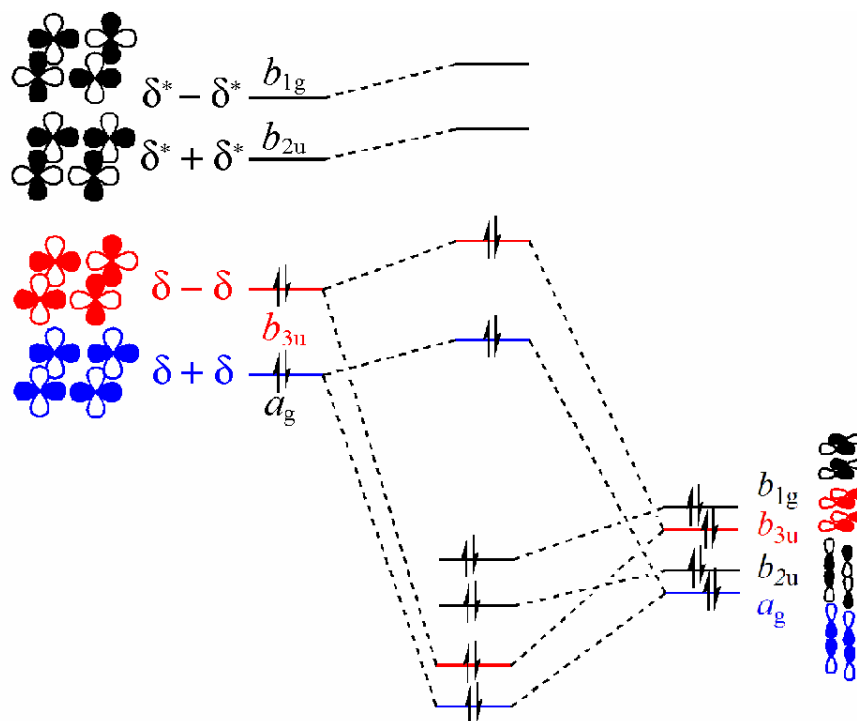
Figure 31. Frontier orbital interactions between the δ orbital combinations of the [Mo_2] units and the *p* orbital combinations of the oxygen atoms in the linkers for model **13** and **16**.

shown in Figure 32, the HOMO shows antibonding character between dimetal units while the HOMO−1 has bonding character, and there is no net bonding between the two dimetal units.

The electronic structure for the model of **14** is similar to that of the precursor except for the existence of an odd electron residing on the metal–based SOMO (77.43% metal character). This is consistent with the EPR spectrum of **2** that shows a low g value of 1.92 and a χT value of 0.375. The spin density of the SOMO (Figure 33) shows that the odd electron is delocalized over the two dimolybdenum units. Because the oxidation of **13** removes one electron from the orbital which results from the metal−metal interaction between the two multiply–bonded Mo_2 units and has antibonding character (δ–δ), compound **14** has a bond order greater than 0 for the σ bonding interaction between the two Mo_2 units. This represents an intermediate for the transition from a non–bonding to a bonding interaction, and explains the shortening of the $Mo_2\cdots Mo_2$ distances in going from **13** to **14**.

For the doubly oxidized compound **15**, calculations were done on models having a singlet ($S = 0$) and a triplet ($S = 1$) state. However, only the model for the singlet state is consistent with the experimental results for **15** in that it gives a contracted $Mo_2\cdots Mo_2$ distance with all other structural parameters being reasonable. The triplet state model increases the $Mo_2\cdots Mo_2$ separation, contrary to experimental observation (Table 16). The singlet state has an energy that is lower by 2.14 Kcal/mol than that of the triplet state. This is again consistent with the experimental observations and further supports the diamagnetism of **15**. Furthermore, a large energy gap ($\Delta E = 2.01$ eV) is found between

the LUMO and HOMO. This value is much higher than that for the singly oxidized **14**, where the model shows that the difference in energy between the SOMO and HOMO−1 is only 0.54 eV. This explains the substantial changes in structural parameters as the second electron is removed from the core of **13** compared with the changes caused by removing the first electron. Thus, on the basis of both experimental results and computational work, it is concluded that a change from a non–bonding to bonding interaction between the two Mo_2 units occurs in the course of removing two electrons from the core of **13**. In compounds of type **I** two single bonds between two dimolybdenum units are generated by a [2 + 2] cycloaddition. For comparison with present results, this could be formally called a 4–electron, 4–center bond, as implied by the upper part of the Scheme 13. In the case of compound **15**, a four–center, two–electron bond is formed in the cyclometallic Mo_4 cluster as illustrated by the lower part of Scheme 13. In a very approximate way, an average bond order of 0.25 may be assigned to the bonding interaction between the two Mo atoms along the long edges of the rectangle.

Scheme 13

HOMO b_{3u} -3.25 eV
76.7% Mo, 2.4% O

SOMO b_{3u} -7.09 eV
74.3% Mo, 5.22% O

LUMO b_{3u} -9.38 eV
74.92% Mo, 8.02% O

HOMO-1 a_g -3.59 ev
92.5% Mo, 0.2% O

HOMO-1 a_g -7.63 eV
71.36% Mo, 7.75% O

HOMO a_g -11.39 eV
71.81% Mo, 9.13% O

13   **14**   **15**
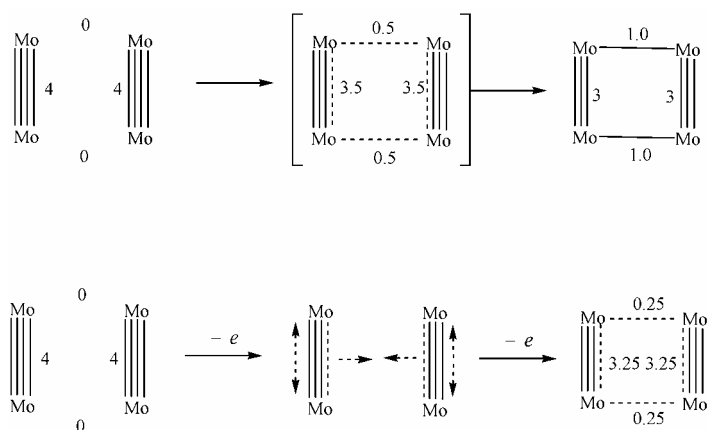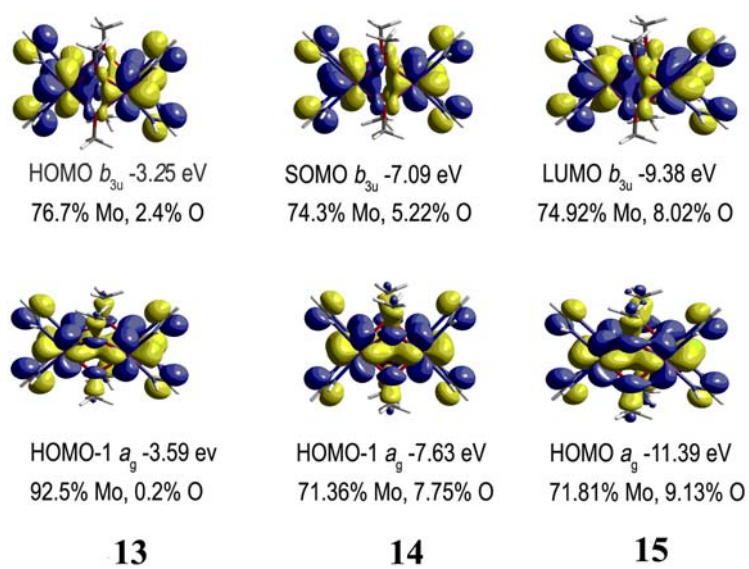
Figure 32. The 0.02 surface contour diagrams for the frontier orbitals for models of **13**, **14** and **15** calculated using DFT.
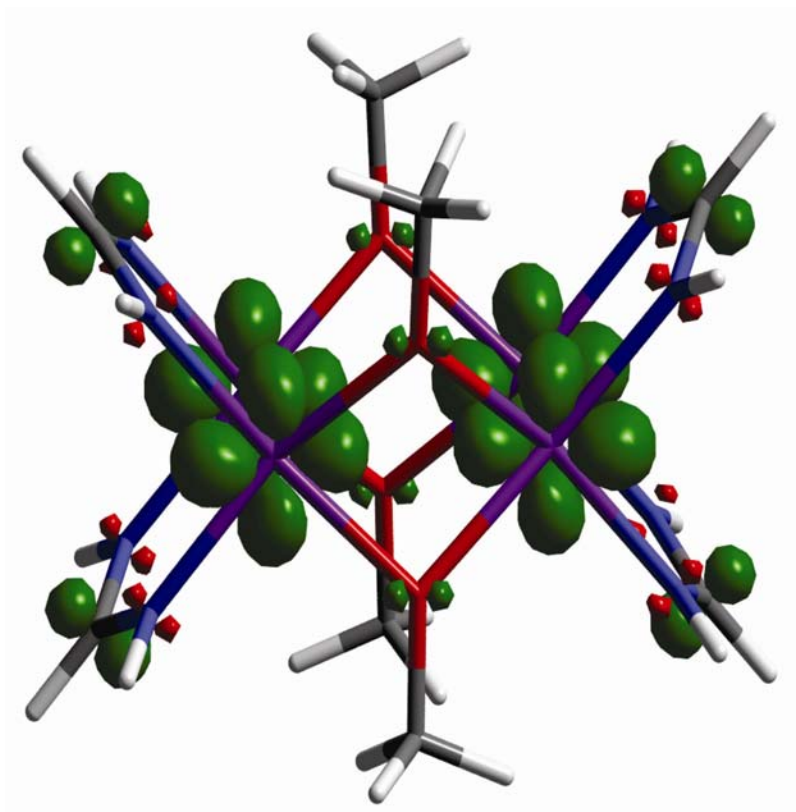
Figure 33. Illustration of the spin density for the SOMO of model **14**.

Finally, TD–DFT calculations were also performed on the models of **13**, **14** and **15** to help with the understanding of the spectroscopic properties of these compounds. Two bands at 586 nm and 546 nm attributed to transitions from the HOMO−1 to LUMO ($\delta+\delta \rightarrow \delta+\delta$) and HOMO to LUMO+1 ($\delta-\delta \rightarrow \delta-\delta$) are calculated for the model of **13**. These calculated bands correspond to experimental absorptions at 500 nm and 420 nm, respectively. For the mixed-valence species **14**, two intense (*f* of ca. 0.046) absorptions resulting from the transitions of HOMO−1 $\rightarrow$ SOMO and HOMO−2 $\rightarrow$ SOMO[62] are predicted. These bands appear in the near-IR spectrum of **14** (Figure 30) at 5900 and 7900 cm^{-1}. A $\delta+\delta \rightarrow \delta+\delta$ transition was calculated at 632 nm and assigned for the absorption band at 487 nm. For the doubly oxidized species **15**, HOMO $\rightarrow$ LUMO and HOMO−1 $\rightarrow$ LUMO transitions are predicted, and these bands appear in the electronic spectrum at 790 and 580 nm, respectively.

CHAPTER VI

ENHANCEMENT IN ELECTRONIC COMMUNICATION UPON RELACEMENT OF Mo–O BY Mo–S BONDS IN TETRANUCLEAR CLUSTERS OF THE TYPE [Mo$_2$]$_2$(μ–X—X)$_2$, X = O or S

INTRODUCTION

Electronic communication in cyclic tetranuclear compounds consisting of two covalently bonded dimolybdenum units joined by four single–atom bridging ligands have been investigated. The compounds of the type [Mo$_2$(cis–DAniF)$_2$]$_2$(μ–X$_4$), where X = Cl, Br and I, and OMe and OEt show two successive one–electron oxidation processes.[23] For the halides (X = Cl, Br and I), the electronic coupling determined from the separation between redox potentials ($\Delta E_{1/2}$) is linearly related to the atomic size of the X, which also controls the metal–metal nonbonding separation. The $\Delta E_{1/2}$ values vary from 540 mV for the chloride bridged compound to 440 mV for the iodide analogue.[23] For these compounds, it was shown that electron removal from the quadruply bonded Mo$_2$ units strengthens the orbital interactions and a transition from nonbonding to bonding interaction has been observed as the oxidation number increases in the compounds $\{$[Mo$_2$(cis–DAniF)$_2$]$_2$(μ–OCH$_3$)$_4\}^{n+}$ (n = 0, 1 and 2). This is possible because of the idealized D_{2h} symmetry of these compounds the orientation of the δ orbitals from the Mo$_2$ units that allow direct metal–metal interactions, when the separation between Mo$_2$ units is short.

Now, we report four new compounds, $[Mo_2(cis-DAniF)_2]_2(\mu-OH)_4$ (**17**),

$[Mo_2(cis-DAniF)_2]_2[\mu-(o-O_2C_6H_4)_2]$ (**18**), $[Mo_2(cis-DAniF)_2]_2[\mu-(o-O_2C_{10}H_6)_2]$ (**19**)

and $[Mo_2(cis-DAniF)_2]_2[\mu-(o-S_2C_6H_4)_2]$ (**20**). While all the previously reported

analogues have the bridging atoms from four isolated groups, three of the present

compounds, **18–20**, have two bidentate ligands that bring two Mo_2 together, and

represent a new subgroup of Mo_4 clusters. In addition, a sulfur–containing linker has

been used to build an Mo_4 cluster (**20**). This compound shows an exceptionally large

potential separation ($\Delta E_{1/2}$ = 776 mV), while for the oxygen bridged analogue (**19**), this

value is only 454 mV, even though the former has a $Mo_2\cdots Mo_2$ distance of 3.724 Å,

considerably larger than 3.267 Å for the latter. Theoretical calculations at the DFT level

suggest that the large difference between **18** and **20** is due to the presence of

superexchange in **20**. The ligand precursors pyrocatechol (a) 2,3-dihydroxynaphthalene

(b) and benzene-1,2-dithiol (c) are shown below in Scheme 14.

Scheme 14

(a)　　　　　　(b)　　　　　　(c)
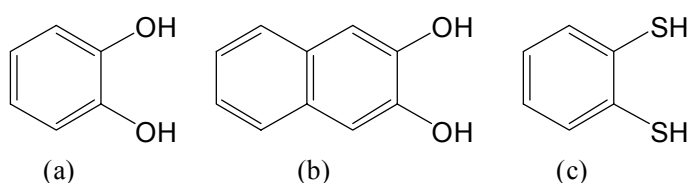
EXPERIMENTAL SECTION

Preparation of $[Mo_2(cis-DAniF)_2]_2(\mu-OH)_4$, 17. To a solution of

$[Mo_2(cis-DAniF)_2(NCCH_3)_4](BF_4)_2$ (208 mg, 0.200 mmol) in 20 mL of THF, was added

slowly, and with stirring, 2.0 mL of a 0.50 M solution of $NaOCH_3$ in methanol. The

color of the mixture changed from red to brown. After the reaction mixture was stirred for 1 h, the solvent was removed under vacuum. The residue was extracted with CH_2Cl_2 (3 × 5 mL) and filtered through a Celite packed frit. After removal of the dichloromethane solvent from the solution, the solid was redissolved in 15 mL of THF. A layer of distilled water was then added to the brown solution. Red block crystals formed in two weeks. Yield: 60 mg (41%). ^1H NMR (δ, ppm in $CDCl_3$): 8.67(s, 4 H, –NC*H*N–), 6.63 (d, 16 H, aromatic C–*H*), 6.49 (d, 16 H, aromatic C–*H*), 3.17 (s, 24 H, –C*H*$_3$ in DAniF), 2.25 (s, 4 H, –O*H*). UV–vis, λ_{max} nm (ε, $M^{-1} \cdot mol^{-1}$): 450 (1.4 × 10^3). Anal. Calcd for $C_{60}H_{70}Mo_4N_8O_{15}$ (**17**·$3H_2O$): C, 46.94; H, 4.56; N, 7.31. Found: C, 46.76; H, 4.12; N, 7.72.

Preparation of [Mo$_2$(*cis*–DAniF)$_2$]$_2$[μ–(*o*–O$_2$C$_6$H$_4$)$_2$], 18. To a Schlenk flask containing a mixture of [Mo$_2$(*cis*–DAniF)$_2$(NCCH$_3$)$_4$](BF$_4$)$_2$ (208 mg, 0.200 mmol) and pyrocatechol (22 mg, 0.20 mmol) was added 20 mL of ethanol. A brown precipitate formed immediately. The reaction mixture was stirred at ambient temperature for 1 h. After the supernatant solution was decanted, the remaining solid was washed with ethanol (2 × 15 mL) and then dried under vacuum. The solid was dissolved in 15 mL of dichloromethane. After passing the mixture through a Celite–packed frit, the filtrate was layered with hexanes. Red–brown crystals were collected after seven days. Yield: 72 mg (45%). ^1H NMR (δ, ppm in $CDCl_3$): 8.70 (s, 2 H, –NC*H*N–), 8.08 (s, 2 H, –NC*H*N–), 6.80 (d, 8 H, aromatic C–*H*), 6.64 (m, 24 H, aromatic C–*H*), 6.38 (d, 8 H, aromatic C–*H*), 3.74 (s, 12 H, –C*H*$_3$ in DAniF), 3.72 (s, 12 H, –C*H*$_3$ in DAniF). UV–vis, λ_{max} nm (ε,

$M^{-1} \cdot mol^{-1}$): 490 (2.0 × 10^3), 440 (1.1 × 10^3). Anal. Calcd for $C_{74}H_{72}Cl_4Mo_4N_8O_{12}$

(**18**·2CH$_2$Cl$_2$): C, 49.62; H, 4.05; N, 6.26. Found: C, 49.52; H, 4.14; N, 6.30.

Preparation of [Mo$_2$(*cis*–DAniF)$_2$]$_2$[μ–(*o*–O$_2$C$_{10}$H$_6$)$_2$], 19. A similar procedure to

that for the preparation of **18** was used starting from [Mo$_2$(*cis*–DAniF)$_2$(NCCH$_3$)$_4$](BF$_4$)$_2$

(208 mg, 0.200 mmol) and 2,3–dihydroxynaphthalene (32 mg, 0.20 mmol) gave brown

crystals. Yield: 80 mg (46%). ^{1}H NMR (δ, ppm in CDCl$_3$): 8.82 (s, 4 H, –NC*H*N–), 7.00

(d, 8 H, aromatic C–*H*), 6.78 (m, 14 H, aromatic C–*H*), 6.50 (m, 14 H, aromatic C–*H*),

6.20 (d, 8 H, aromatic C–*H*), 3.80 (s, 12 H, –C*H$_3$* in DAniF), 3.68 (s, 12 H, –C*H$_3$* in

DAniF). UV–vis, λ$_{max}$ nm (ε, $M^{-1} \cdot mol^{-1}$): 480 (4.0 × 10^3), 440 (1.8 × 10^3). Anal. Calcd

for $C_{81}H_{74}Cl_2Mo_4N_8O_{14}$ (**19**·CH$_2$Cl$_2$): C, 52.92; H, 4.06; N, 6.10. Found: C, 52.86; H,

4.14; N, 6.58.

Preparation of [Mo$_2$(*cis*–DAniF)$_2$]$_2$[μ–(*o*–S$_2$C$_6$H$_4$)$_2$], 20. Benzene–1,2–dithiol (43

mg, 0.30 mmol) was dissolved in 20 mL of ethanol and the solution cooled to 0 ºC. This

solution was transferred using a cannula to a precooled solution of

[Mo$_2$(*cis*–DAniF)$_2$(NCCH$_3$)$_4$](BF$_4$)$_2$ (208 mg, 0.200 mmol) in 10 mL of ethanol. A

brown–orange precipitate formed immediately. The reaction mixture was stirred at 0 ºC

for 1 h. Then a similar procedure to that for **18** gave orange needle–crystals. Yield: 50

mg (30%). ^{1}H NMR (δ, ppm in CDCl$_3$): 8.26(s, 4 H, –NC*H*N–), 7.52 (m, 4 H, aromatic

C–*H*), 7.12 (m, 4 H, aromatic C–*H*), 6.60 (m, 32 H, aromatic C–*H*), 3.73 (s, 24 H, –C*H$_3$*).

UV–vis, λ$_{max}$ nm (ε, $M^{-1} \cdot mol^{-1}$): 645 (1.0 × 10^3), 455 (8.0 × 10^3). Anal. Calcd for

$C_{73.5}H_{71}Cl_3S_4Mo_4N_8O_8$ (**20**·1.5CH$_2$Cl$_2$): C, 48.69; H, 3.94; N, 6.18. Found: C, 48.42; H,

3.75; N, 6.18.

RESULTS AND DISCUSSION

Syntheses. Compounds **18**, **19** and **20** were prepared by mixing dimolybdenum starting material, $[Mo_2(cis\text{–}DAniF)_2(NCCH_3)_4](BF_4)_2$, with the corresponding bridging reagent. Similar procedure has been used for the syntheses of halide and the alkoxide bridged compounds. Compared to the first approach to this type of dimolybdenum pairs, this method is straightforward and convenient, and the yield is generally good. However, small modifications to the reaction are usually necessary according to the bridging reagent used. For the preparation of halide and alkoxide bridged compounds, commercially available tetrabutylamonium halides and sodium methoxide were chosen to be the reactants, respectively. Here, the corresponding neutral ligand was applied directly for the assembly reaction with the Mo_2^{4+} complex as shown in the following equation.

$$2cis\text{-}Mo_2(DAniF)_2(NCCH_3)_4(BF_4)_2 \; + \; 2 \underset{\text{XH}}{\overset{\text{XH}}{\bigcirc}} \xrightarrow{\text{ethanol}}$$

$$[Mo_2(cis\text{-}DAniF)_2]_2[\mu\text{-}(o\text{-}X_2C_6H_4)_2] + 4NCCH_3 + 2HBF_4$$

$$X = O \text{ or } S$$
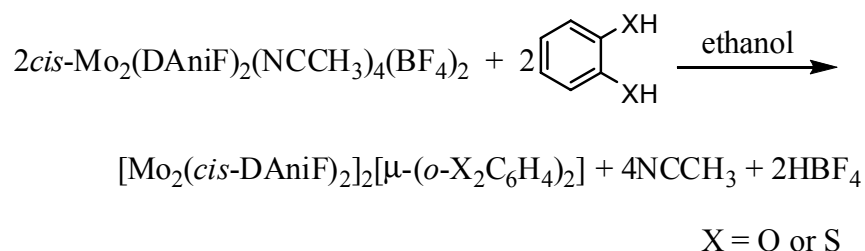
Because they are fairly acidic, spontaneous deprotonation occurs as the complexation takes place. Polar solvent, e.g. ethanol, is used for the reaction to gain extra driving force because the neutral product is less soluble in this solvent. On the other hand, basic conditions, which would result in hydroxide and alkoxide bridged impurities, should be avoided. Benzene–1,2–dithiol for compound **20** is more reactive than pyrocatechol and the reaction was carried out at low temperature.

Compound **17** was synthesized differently. The reaction of NaOH with the dimolybdenum starting material in organic solvent did not afford the target compound. In earlier work, we have noticed that the alkoxide bridged compounds partially hydrolyze if the solvent is not freshly dried. In this work, hydrolysis is intentionally carried out for the preparation of the hydroxide derivative (**17**). Addition of sodium methoxide to the dimolybdenum corner species generates the methoxide bridged compound as described in prior work. Subsequent hydrolysis, in the presence of H_2O, yields **17** as a crystalline product.
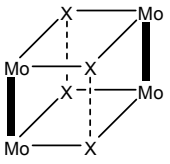
Structural Results. Compounds **17–20** have been structurally characterized by single–crystal X–ray diffraction. The crystallographic data are listed in Table 17 and selected bond distances and angles, along with the structural parameters for other known type **III** compounds, are in Table 18. The core structure of $[Mo_2(cis–DAniF)_2]_2(\mu–OH)_4$ (**17**), shown in Figure 34, resembles that in other Mo_4 clusters having a Mo_4X_4 cubic core and is closely related to that in $[Mo_2(cis–DAniF)_2]_2(\mu–OR)_4$ (R = Me, Et). In **17** there are two crystallographic independent but structurally similar molecules in the unit cell. The nonbonding separation between the two Mo_2 units in **17** of 3.23 Å is similar to that in the methoxide bridged analogue (3.24 Å). The Mo–Mo distances for the two molecules, 2.111(1) and 2.113(1) Å, resemble those in $[Mo_2(cis–DAniF)_2]_2(\mu–X)_4$ but are noticeably shorter than metal–metal bonds in the OR bridged analogues (ca. 2.132 Å). This can be attributed to the lower basicity of the OH groups compared to that of the OR groups that donate more electron density to the metal center.

Table 17. X–ray Crystallographic Data for **17**, **18**, **19** and **20**.

Compound	17·2THF	18·0.5CH₂Cl₂	19·CH₂Cl₂	20·2CH₂Cl₂
Empirical formula	$C_{68}H_{80}Mo_4N_8O_{14}$	$C_{73}H_{70}ClMo_4N_8O_{12}$	$C_{81}H_{74}Cl_2Mo_4N_8O_{12}$	$C_{74}H_{72}Cl_2Mo_4N_8O_8S_4$
Fw	1617.16	1706.03	1806.14	1855.2
space group	$P\bar{1}$ (No. 2)	$P\bar{1}$ (No. 2)	$P\bar{1}$ (No. 2)	$P\bar{1}$ (No. 2)
a, Å	12.740(4)	10.590(3)	10.480(6)	10.365(4)
b, Å	12.859(4)	14.603(4)	14.735(8)	15.036(5)
c, Å	20.917(6)	14.675(4)	14.792(8)	15.210(5)
α, deg	94.484(5)	104.881(5)	104.701(9)	118.909(6)
β, deg	91.957(6)	108.272(4)	105.451(9)	94.175(6)
γ, deg	95.536(5)	106.460(5)	109.507(8)	103.173(6)
V, Å³	3397(2)	1912(1)	1922(2)	1973(1)
Z	2	1	1	1
T, K	213	213	213	213
λ, Å	0.71073	0.71073	0.71073	0.71073
d_{calcd}, g/cm³	1.581	1.482	1.56	1.561
μ, mm⁻¹	0.791	0.773	0.774	0.92
R1^a (wR2^b)	0.1044 (0.1124)	0.0664 (0.1649)	0.0786 (0.1845)	0.1449 (0.1943)

^{a} R1 = $\Sigma||F_o| - |F_c||/\Sigma|F_o|$. ^{b} wR2 = $[\Sigma[w(F_o^2 - F_c^2)^2]/\Sigma[w(F_o^2)^2]]^{1/2}$

Table 18. Selected Bond Distances (Å) and Angles (deg) for $[Mo_2]_2(\mu-X_4)$ Clusters.

Bridges (X)	Mo–Mo	$Mo_2\cdots Mo_2$	Mo–X	Mo–X–Mo	X–Mo–X	X···X (diagonal)	X···X (edge)
Cl[a]	2.1191(4)	3.601	2.516[2]	91.42[5]	81.06[4]	3.273	3.419
Br[b]	2.1181(6)	3.697	2.649[2]	88.50[2]	82.95[3]	3.509	3.564
I[b]	2.117(1)	3.915	2.845[2]	87.02[2]	86.43[3]	3.802	3.768
OMe[c]	2.1315(7)	3.245	2.142[4]	98.6[2]	74.4[2]	2.570	3.206
OEt[c]	2.1317(4)	3.241	2.136[2]	98.67[9]	74.1[1]	2.575	3.190
OH (17)	2.112[2]	3.254	2.127[7]	100.0[3]	74.9[2]	2.581	3.093
O_2 (18)	2.1135[9]	3.266	2.137[5]	99.8[2]	75.2[2]	2.605	2.999
O_2 (19)	2.113[1]	3.290	2.150[7]	99.9[2]	75.4[2]	2.629	2.977
S_2 (20)	2.093[2]	3.724	2.527[5]	95.1[1]	77.7[1]	3.166	3.350

(a) see ref 23(a). (b) see ref 23(b). (c) see Chapter V.

As shown in the Scheme 15, for compounds $[Mo_2(cis–DAniF)_2]_2[\mu–(o–O_2C_6H_4)]_2$, **18**, and $[Mo_2(cis–DAniF)_2]_2[\mu–(o–O_2C_{10}H_6)_2]$, **19**, one could envision the formation of two possible geometric isomers having an idealized $[Mo_2]_2(\mu–O)_4$ cubic core. In structure **A** the two O atoms from each of the bidentate anions bind to all four Mo atoms in such a way that the C–C bond in the O–C–C–O unit is essentially parallel to the two Mo_2 units while in structure **B** the O atoms from each linker bind to only two Mo atoms. As shown in Figure 35, the structure of **18** obtained from crystals that formed in the space group $P\bar{1}$ with the molecule residing on a special position adopts a structure of type **A**. A similar structure is adopted by **19**.

Scheme 15

A   **B**
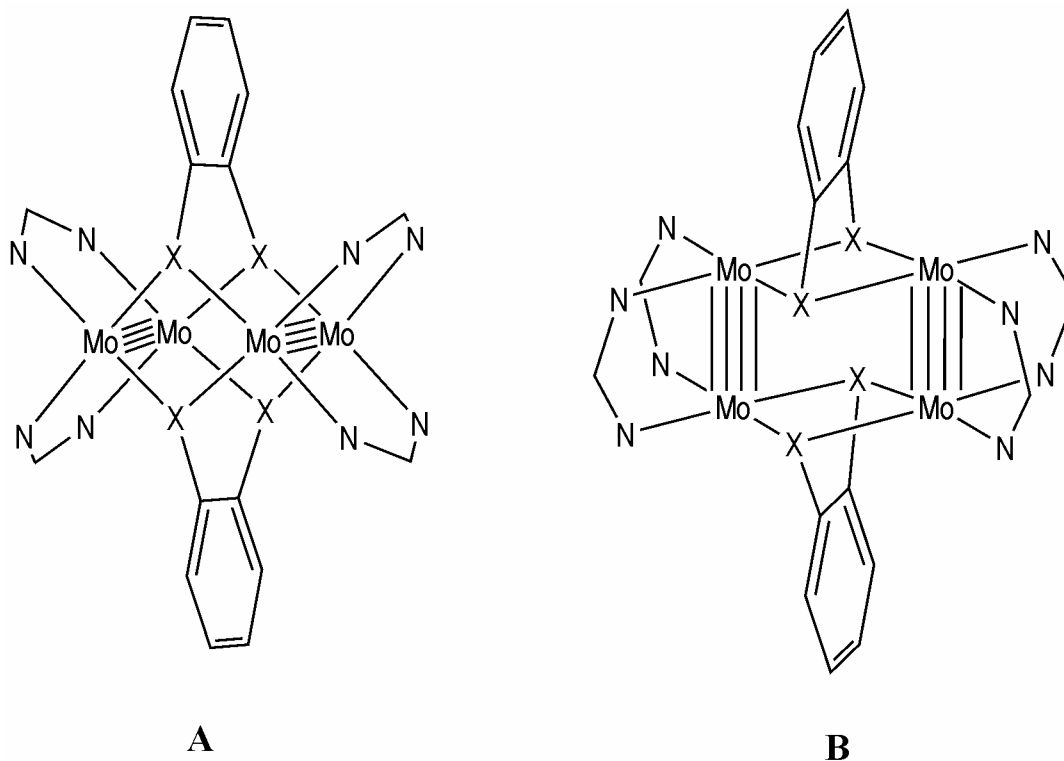
Figure 34. Core structure of **17** with displacement ellipsoids drawn at the 40% probability level. All *p*–anisyl groups and hydrogen atoms in DAniF have been omitted for clarity.

Figure 35. Core structure of **18** with displacement ellipsoids drawn at the 40% probability level. All *p*–anisyl groups and hydrogen atoms in DAniF have been omitted for clarity.

When the structural parameters (Table 18) of **18** are compared to those of **17**, which has four isolated bridging OH groups, it is clear that the chelating linkers do not pose significant strain to the complex core. The Mo–Mo bond lengths in the two compounds, 2.111[2] Å for **17** and 2.1135[9] Å for **18**, are essentially identical. For both compounds, the Mo_2 to Mo_2 nonbonding separations are also essentially the same, ca. 3.27 Å. In **18**, the two bridging oxygen atoms in the aromatic ring are separated by 3.02 Å, a distance similar to the corresponding distances between two isolated oxygen bridging atoms in **17** (ca. 3.09 Å). The O–Mo–O angles in these two compounds are also comparable, that is, 74.8° for **17** and 75.2° for **18**, and the ranges for the Mo–O–Mo angles, 98.9–99.1° for **17** and 99.4–100.1° for **18**, are also similar.

For **19**, which has two deprotonated 2,3–dihydroxynaphthalene anions bridging two $[Mo_2(cis–DAniF)_2]^{2+}$ units, the structure is shown in Figure 36. Similar to **18**, this compound has the structural type **A**. The structural parameters for **19** are generally similar to those in structurally related compounds (Table 18). Compound **20**, the sulfur analogue of **18**, also crystallized in the space group $P\bar{1}$ with $Z = 1$. These compounds are isostructural having a type **A** structural motif, as shown in Figure 37. The Mo–Mo distances, 2.093(2) Å, are significantly shorter than those in **18** by about 0.02 Å, as shown in Table 18. This is the Mo_4 cluster with the shortest metal–metal bonds. When compared to **18**, the change in the bridging donor atoms from O to S increases the X–Mo–X angles from 75.3° (X = O) to 77.8° (X = S), but reduces the X–Mo–X angles from 99.42–100.03° (X = O) to about 95° (X = S). The $Mo_2{\cdots}Mo_2$ separation increases by about 0.46 Å from 3.26 Å to 3.72 Å. For the Mo_4S_4 cubic core, the S to S separations
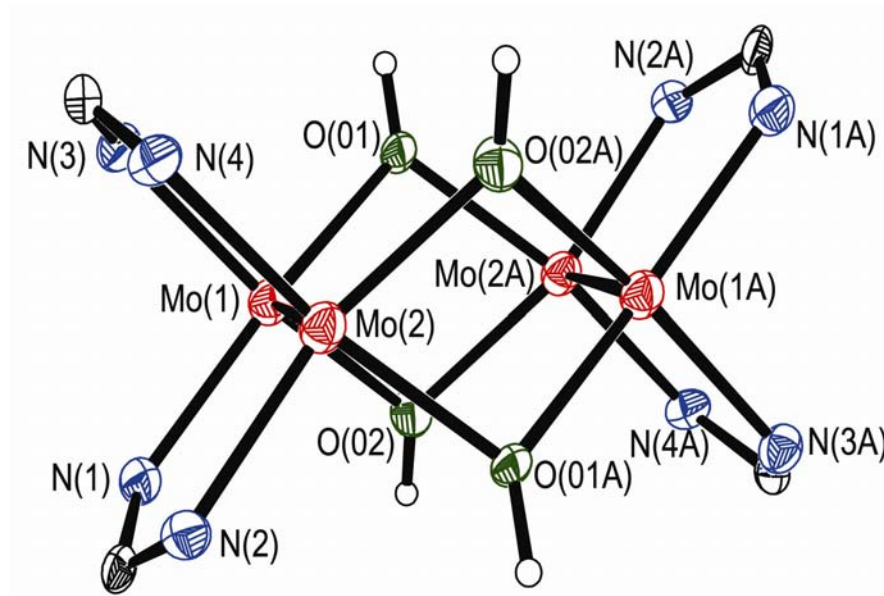
Figure 36. Core structure of **19** with displacement ellipsoids drawn at the 40% probability level. All *p*–anisyl groups and hydrogen atoms in DAniF have been omitted for clarity.
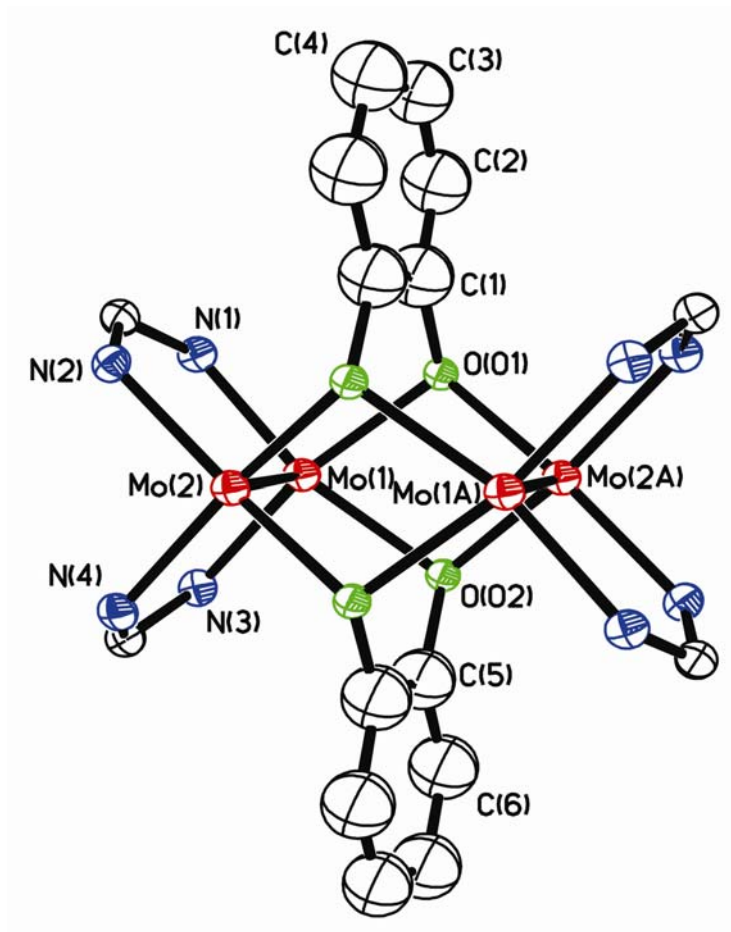
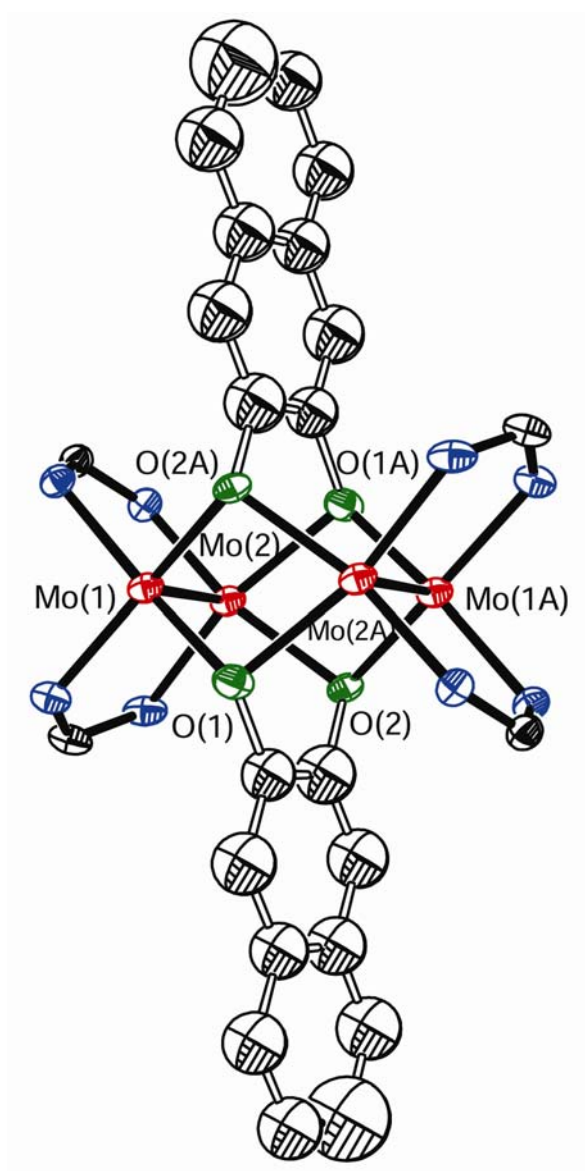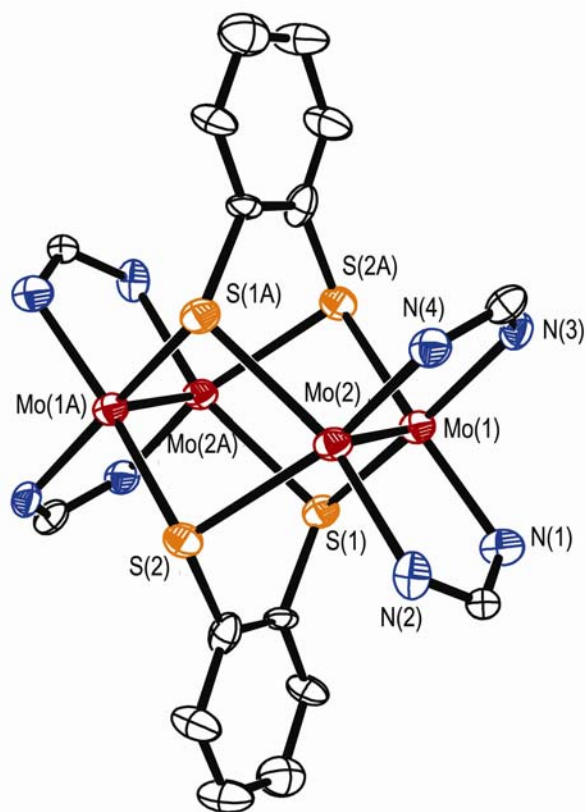**Figure 37**. Core structure of **20** with displacement ellipsoids drawn at the 40% probability level. All *p*–anisyl groups and hydrogen atoms have been omitted for clarity. Note the structural similarity to the cores of **18** and **19**. However, the $Mo_2 \cdots Mo_2$ separation is ca. 0.45 Å longer in **20** than in **18** and **19**.

along the edges are 3.35 Å and diagonal S···S separations are 3.166 Å. It should be noted that the many compounds containing M_4S_4 cubic cores (M = Mo, W and Fe) are important in biological systems such as in nitrogenase enzymes but these have metal units in a tetrahedral geometry.[63]

Electrochemistry. Compounds **18–20** show two reversible one–electron oxidation processes. This is shown for the structurally analogous compounds **18** and **20** in Figure 38. For **18** shows the first oxidation process occurs at about 100 mV and the second at about 550 mV. These potentials are much more positive than the corresponding values for the alkoxide–bridged compounds, −338 and 216 mV for the methoxide analogue, but the $\Delta E_{1/2}$ for the two compounds is relatively small. The shift in electrochemical potential is mainly due to the difference in Lewis basicity of the bridging ligands since the strongly basic alkoxide anions donate more electron density to the dimetal centers than the diphenol anions. As shown in Table 19, the electrochemical oxidations for $[Mo_2(cis–DAniF)_2]_2(\mu–Cl_4)$, which occur at 260 and 800 mV, are shifted by more than 100 mV when compared to **18**, but again these compounds have a similar $\Delta E_{1/2}$. This is because halides are much weaker Lewis bases than the bidentate ligands reported here.

Compound **20**, the first $[Mo_2]_2(\mu–S_4)$ cluster, $E_{1/2}(1)$ is considerably more negative than that in **18** but $E_{1/2}(2)$ is more positive. However, the most striking difference is the very large $\Delta E_{1/2}$ of 776 mV, which is significantly larger than the $\Delta E_{1/2}$ values for any other Mo_4 cluster (see Table 19). The large potential separation is indicative of large electronic communication and this occurs despite the increase in non–bonding separation between the midpoints of the Mo_2 units which changes from 3.266 Å in **18** to 3.72 Å in

20 and the increase of ca. 0.45 Å in M–X distances, X = O and S. Both of the latter factors would be expected to diminish the degree of communication between the dimetal units. Thus, the electrochemical behavior of **20** does not follow the linear relationship of $\Delta E_{1/2}$ vs metal–to–metal separation found for the series of compounds of the type $[Mo_2]_2(\mu-)X_4$ (X = Cl, Br and I). Clearly, the increase in the $\Delta E_{1/2}$ value by more than 300 mV for the sulfur bridged compound, while the two Mo_2 are farther apart, cannot be interpreted solely by direct metal–metal interaction and another pathway should amplify the electron delocalization.
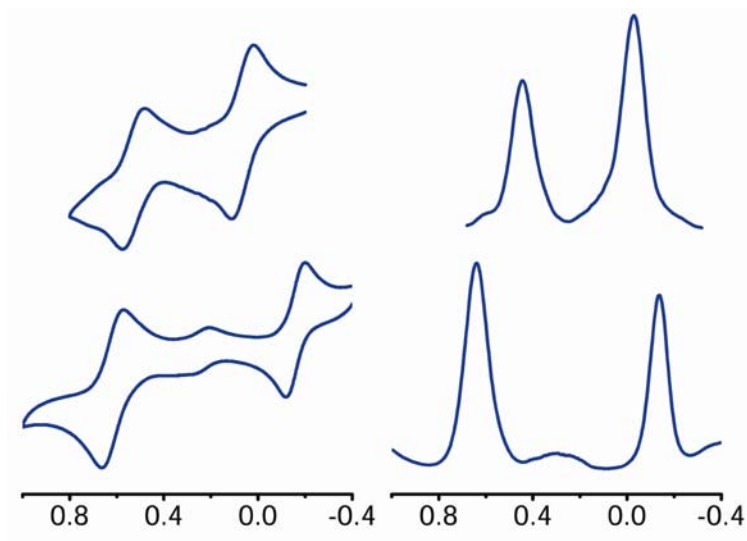
Figure 38. Cyclic voltammograms (with potentials vs Ag/AgCl) and differential pulse voltammograms taken in CH_2Cl_2 solution for the analogous compounds **18** and **20** which contain Mo–O and Mo–S bonds, respectively. Note the large difference in $\Delta E_{1/2}$ values for these compounds which is manifested in a K_C that is five orders of magnitude greater for the S–containing compound than for **18**.

Table 19. Oxidation Potentials and Comproportionation Constants for Some

$[Mo_2]_2(\mu-X_4)$ Tetranuclear Compounds.

Compound	$Mo_2 \cdots Mo_2$	$E_{1/2}(1)$	$E_{1/2}(2)$	$\Delta E_{1/2}$	Kc
$[Mo_2(cis-DaniF)_2]_2(\mu-Cl)_4$ [a]	3.601	260	800	540	1.3×10^9
$[Mo_2(cis-DaniF)_2]_2(\mu-Br)_4$ [b]	3.697	314	813	499	2.7×10^8
$[Mo_2(cis-DaniF)_2]_2(\mu-I)_4$ [b]	3.915	350	790	440	2.7×10^7
$[Mo_2(cis-DaniF)_2]_2(\mu-OMe)_4$ [c]	3.245	−338	216	554	2.3×10^9
$[Mo_2(cis-DaniF)_2]_2(\mu-OEt)_4$ [c]	3.241	−418	169	587	8.4×10^9
$[Mo_2(cis-DaniF)_2]_2(\mu-O_2C_6H_4)_2$	3.266	75	529	474	1.0×10^8
$[Mo_2(cis-DaniF)_2]_2(\mu-S_2C_6H_4)_2$	3.724	−155	621	776	1.3×10^{13}

(a) See ref 23(a). (b) See ref 23(b). (c) See Chapter V.

Electronic Structure. To gain insight into the electronic configurations of these compounds, DFT calculations were performed on the models $[(HNC(H)NH)_2Mo_2]_2(OH)_4$ (**17'**), $[(HNC(H)NH)_2Mo_2]_2(O_2C_6H_4)_2$ (**18'**) and $[(HNC(H)NH)_2Mo_2]_2(S_2C_6H_4)_2$ (**20'**), in which hydrogen atoms replaced the aryl groups in the formamidinate groups. This simplification has been used successfully in calculations for compounds with $Mo_2(DAniF)_3$ or $cis-Mo_2(DAniF)_2$ units linked by various bridges. The calculated energies and selected geometries for the models **17'**, **18'** and **20'** are listed in Table 20.

Because of the idealized D_{2h} symmetry of the Mo_4 clusters, the frontier molecular orbitals are formed mainly through the δ orbital interactions between the two dimetal units. In–phase and out–of–phase combinations of the δ antibonding orbitals generate the LUMO (δ* + δ*) and LUMO+1 (δ* − δ*), respectively, while the HOMO and HOMO−1 are composed of δ + δ and δ − δ (Figure 39). A consequence of δ to δ interactions is the breaking of the degeneracy of these orbitals for the two isolated Mo_2 units. On this basis, it is stated that electron delocalization is invoked through direct metal–metal interactions. The magnitude of energy difference (ΔE) between the HOMO and HOMO−1 reflects, to some extent, the strength of the orbital interactions, and it is used to assess the metal–metal coupling effect. A large calculated energy gap (ΔE from DFT calculation) for a strongly electronically coupled system would be expected to be reflected in the measured value of $\Delta E_{1/2}$. This relationship between ΔE (energy) and $\Delta E_{1/2}$ (potential) have been shown to exist in both strongly and weakly coupled systems having linked Mo_2 units.

LUMO, -0.54 eV
79.6% Mo, 2.6% O

LUMO, -0.80 eV
77.3% Mo, 2.6% O

LUMO, -1.06 eV
68.6% Mo, 6.0% S

HOMO, -3.40 eV
68.3% Mo, 2.4% O

HOMO, -3.78 eV
77.5% Mo, 1.8% O

HOMO, -3.97 eV
79.1% Mo, 3.3% S

HOMO-1, -3.62 eV
71.1% Mo, 5.1% O

HOMO-1, -3.97 eV
65.9% Mo, 6.7% O

HOMO-1, -4.21eV
65.1% Mo, 9.5% S

17'   **18'**   **19'**
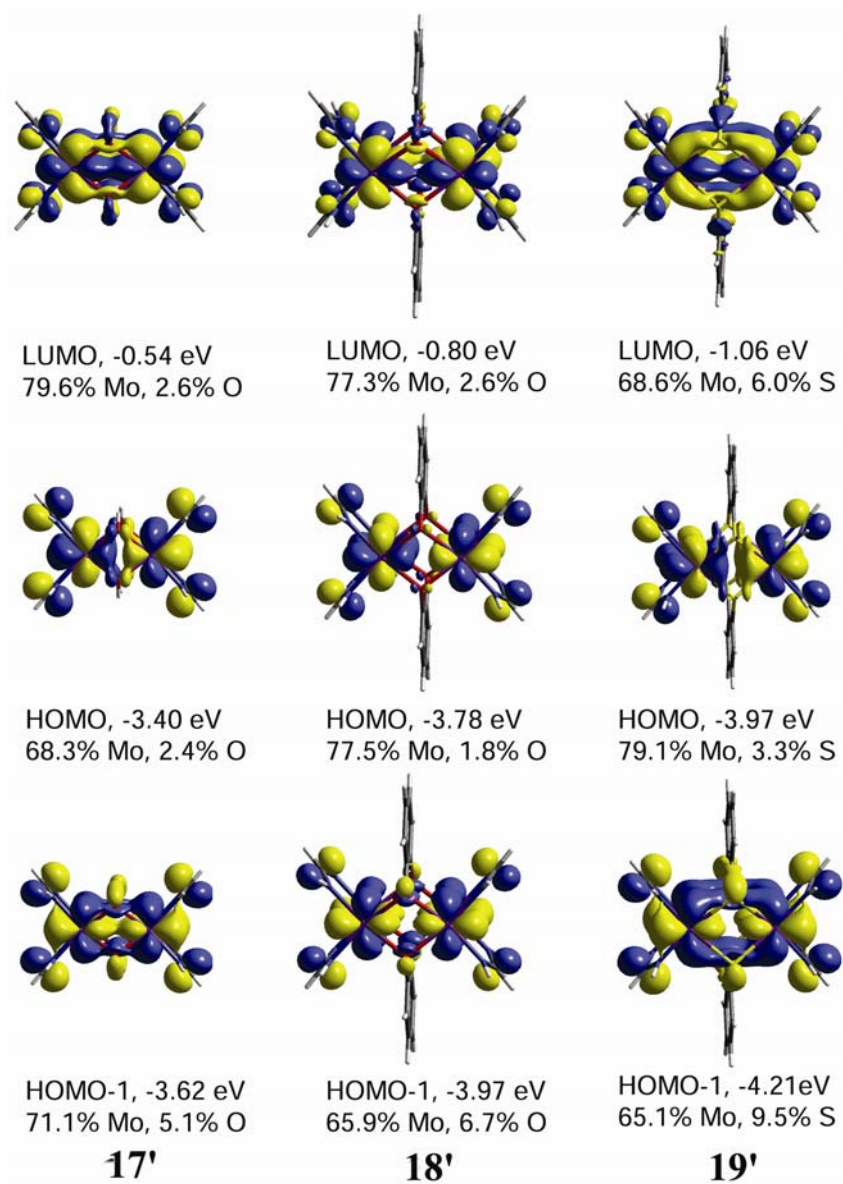
Figure 39. 0.02 surface contour diagrams for the frontier orbitals for models **17'**, **18'** and

20' calculated using DFT.

Table 20. Calculated Data from DFT for Models **17'**, **18'** and **20'**.

Model	Energy (a.u.)	HOMO (eV)	HOMO–1 (eV)	ΔE (eV)	Calculated bond lengths (Å) and angles (deg)			
					Mo–Mo	Mo$_2$···Mo$_2$	Mo–L	Mo−L−Mo
17'	−1171.4486	−3.40	−3.62	0.22	2.168	3.348	2.173	100.79
18'	−1631.0351	−3.78	−3.97	0.19	2.144	3.435	2.214	101.76
20'	−2923.0042	−3.97	−4.21	0.24	2.143	3.861	2.600	95.92

The calculation on the model **20'**, Figure 39 and Table 20, shows the difference in electronic structure as sulfur replaces oxygen atoms in the bridging ligands. First, for the model **20'**, the energy gap (ΔE) between HOMO and HOMO–1 is 0.24 eV, larger than 0.19 eV for the model **18'**. This is consistent with the electrochemistry that shows larger redox potential separation for compound **20**. Recent report[12(a)] of DFT calculations on the dimer of dimers $[(HCO_2)_3M_2]_2(–X–C_6H_4–X)$ (M = Mo and W and X = CO_2, COS and CS_2) revealed that successive substitution of oxygen by sulfur also leads to enhanced electronic coupling as evidenced by the increased energy separation of HOMO and HOMO–1. Secondly, as shown in Figure 39, the MOs contain enhanced character of the bridging atoms as sulfur is used. For example, when oxygen serves as the bridge in **18'**, the LUMO is composed of 2.6% O and the HOMO 1.8% O, but in the sulfur containing model **20'**, sulfur contributes 6.0 and 3.3%, respectively to the LUMO and HOMO. The difference in electronic coupling results from the different orbital profiles for the two models **18'** and **20'** are also quite different. Significant orbital overlap in **20'** is seen between the sulfur and the Mo_2 units but not in **18'**. The increased involvement of bridging atoms in **20'** suggests that superexchange through the sulfur bridges makes a significant contribution that strengthens the electronic coupling. Scheme 16 shows the molecular orbital diagram of the superexchange pathway for the electronic communication for **20**. This pathway is less important for **18**, in which the electronic communication is mainly through direct interaction between δ orbitals. This explains the exceptionally strong electronic communication that occurs in compound **20**, even though

the increase the Mo_2 to Mo_2 distances in this compound relative to that in **2** would be expected to diminishes direct metal–metal interactions. This is also different from that of $[(HCO_2)_3M_2]_2(-X-C_6H_4-X)$, where the LUMO is a bridge–based π^* orbital, and the enhanced coupling arises principally from a lowering of the LUMO of the bridge $-X-C_6H_4-X$ by changing X from O to S.

CHAPTER VII

CONCLUSIONS

In this work, dimolybdenum units with multiple metal-metal bonds have been employed to assemble dimer of dimers and tetranuclear clusters. Electronic coupling between the dimetal centers were investigated through X-ray crystallography, electrochemistry, NIR, EPR, electronic spectra, magnetic measurement and DFT calculations.

In Chapter II, a good, general and convenient synthetic method for the preparation of polyamidate–linked dimolybdenum compounds is described. It is shown that the separation between [Mo$_2$] units has a significant effect in the electronic communication. When compounds **1**–**3**, which are linked with polyamidate groups separated by an aryl group, are compared to analogues with short linkers such as *N,N'*–dimethyloxamidate in the β form, a significant decrease in the electronic communication is observed. In Chapter III, the large rigid, conjugated fluoflavinate anion is the first all–nitrogen donor ligand that has been used to link dimetal units to form dimer–of–dimers type compounds. The electrochemistry of this compound shows three one–electron redox couples; two have been assigned to metal–based oxidations and the third one to a ligand–based oxidation. All three members of the electron–transfer series, [Mo$_2$]fluoflavinate[Mo$_2$]$^{n+}$ (*n* = 0, 1 and 2) were structurally characterized. Various spectroscopic techniques and DFT calculations indicate that the fluoflavinate dianion is a strong mediator of electronic communication.

This complex system provides an excellent example of how intramolecular electron transfer can be modified by ligand design. Calculations at the DFT level were carried out using three functionals B3LYP, mPW1PW91 and BP86 in order to study the electronic structure of **5**, **6**, **7**, and **8**, and with the idea of evaluating how well the calculated results reproduce experimental data in [Mo$_2$]L[Mo$_2$] compounds. The frontier orbitals of such systems consist of the in–phase and out–of–phase combinations of the δ orbitals mediated by the bridge ligand. The results obtained by the three functionals are qualitatively consistent with each other, and mPW1PW91 yields geometries of remarkable accuracy compared to the crystal structures obtained by X–ray diffraction. Chapter IV reported the dimer of dimers containing dimolybdenum units linked by unsubstituted oxamidate and dithiooxamidate. The crystal structures of compounds **10** and **11** are isomorphic and the molecules are planar due to intramolecular hydrogen bonds in the bridge ligands. Compound **11** can further react with LiMe to remove the hydrogen atoms left in the bridge to form compound **12** with two dimetal and two single metal units linked by one bridge. The electronic coupling between the dimetal units in compounds **11** is substantially stronger than that of compound **10**, evidenced by electrochemistry which shows potential separations ($\Delta E_{1/2}$) between two oxidation processes of 204 for **10** and 407 mV for **11**. This corresponds to comportionation constant Kc values of 2.8 × 10^3 and 7.6 × 10^6, respectively. DFT calculations on simplified models **10′** and **11′** show that the electronic structures are different and the energy of bridge π* orbital is much lower for **10′**, which lowers the energy of metal–to–ligand charge–transfer band. The lower energy for the

'electron hopping' pathway explains the large increase in electronic communication by substitution of O to S.

In Chapter V, tetranuclear Mo_4 clusters with two quadruply bonded Mo_2^{4+} units, [$Mo_2(cis$–DAniF)$_2$] linked by methoxide, **13**, and ethoxide groups, **16**, have been prepared by direct assembly from the building block [$Mo_2(cis$–DAniF)$_2(CH_3CN)_4]_2^{2+}$ with the corresponding bridging ligands. The non–bonding separation between the midpoints of the quadruply bonded units, ca. 3.24 Å, is the shortest among compounds having two linked Mo_2^{4+} units. A significant amount of direct δ to δ orbital interaction between the two dimetal centers occurs and accounts for the large electronic coupling between the dimetal units, as shown by the $\Delta E_{1/2}$ values of 554 and 587 mV for **13** and **16**, respectively. When compound **13** was chemically oxidized using 1 equiv of ferrocenium to the mixed–valence species **14** by removal of one electron from a bonding orbital of the dimetal units, the Mo−Mo bond distances were lengthened from 2.1315(7) to 2.1493(3) Å but the separation between dimetal units was shortened by about 0.14 Å. This compound shows two broad absorption bands in the NIR region at 5900 and 7900 cm$^{−1}$, and they are assigned to the HOMO−1 → SOMO and HOMO−2 → SOMO transitions, respectively. The doubly oxidized compound **15** is diamagnetic as shown by the sharp signals in the ^{1}H NMR spectra and the lack of an EPR signal. The Mo−Mo bond lengths, or the short edges of the Mo_4 rectangle in **15**, increase to 2.1779 Å, a distance that is exceptionally long as compared to those in compounds with a Mo_2^{5+} core. The metal–metal separation, or the long edges of the rectangle, of 2.945 Å, is shorter by about 0.16 Å than those in **14** and are close in length to the long edges in

metallacyclobutadiynes. DFT calculations together with the experimental results lead us to conclude that a four–center, two–electron bond is formed in the cyclometallic Mo_4 cluster **15**. In this $[Mo_2]_2(\mu–OMe)_4$ system, a transformation from a neutral compound **13** with no bonding interaction between the two Mo_2 units to a doubly oxidized compound **3** that has a bonding interaction between the two dimolybdenum units was observed; this occurs via an intermediate state having a singly oxidized mixed–valence species **14** that exhibits large electronic communication. Similarly to $[Mo_2]_2(\mu–OR)_4$ tetranuclear cluster containing two quadruply bonded Mo_2 units linked by four hydroxide groups (**17**) and compounds linked by two bidentate bridges ($o–O_2C_6H_4$ for **18,** $o–O_2C_{10}H_6$ for **19** and $o–S_2C_6H_4$ for **20**) were synthesized starting from corner species precursor $[Mo_2(cis–DAniF)_2(NCCH_3)_4](BF_4)_2$ (Chapter VI). The Mo–S distances in **20** are ca. 0.4 Å longer than those of Mo–O bonds in **17**–**19**, and consequently the non–bonding separation between the midpoints of the Mo_2 units changes from 3.27 Å in **17**–**19** to 3.72 Å in **20**. However, the electronic coupling between the two Mo_2 units was enhanced by replacing the O–atoms by S from **18** to **20** as evidenced by electrochemical measurements, which show two reversible one–electron oxidation processes with potential separations ($\Delta E_{1/2}$) between the two oxidation processes of 474 and 776 mV, respectively. DFT calculations suggest that the enhancement in electronic communication between the metal centers in **20** is due to the existence of a super–exchange pathway in **20** that is less important for **18**.

Generally for dimer of dimers, described by a general formula $[Mo_2]L[Mo_2]$, the metal to ligand back bonding is critical to the electron transfer pathway. The electronic

coupling between the metal centers increases as substitution of O–donor atoms to N or S in the linkers if the substitution does not change the structure substantially. The short separation between dimetal units and possible direct δ to δ orbital interactions in tetranuclear Mo_4 clusters accouts for the large electronic communication. The separation between the dimetal units decreases as $[Mo_2(cis–DAniF)_2]_2(\mu–OCH_3)_4$ is singly and then doubly oxidized, which suggests bond formation between dimetal centers while $[Mo_2(cis–DAniF)_2]_2(\mu–o–S_2C_6H_4)_2$ shows an exceptionally strong electronic coupling due to super–exchange pathway.

REFERENCES

[1] (a) Brunschwig, B. S.; Sutin, N. *Coord. Chem. Rev*. **1999**, *187*, 233. (b) Holm, R. H.; Kennepohl, P.; Solomon, E. I. *Chem. Rev*. **1996**, *96*, 2239. (c) Marcus, R. A. *J. Electroanal. Chem*. **1997**, *438*, 251. (d) Cameron, C. G.; Pickup, P. G. *J. Am. Chem. Soc*. **1999**, *121*, 7710. (e) Demadis, K.D.; Hartshorn, C. M.; Meyer, T. J. *Chem. Rev*. **2001**, *101*, 2655. (f) Lau, V. C.; Berben, L. A.; Long, J. R. *J. Am. Chem. Soc*. **2002**, *124*, 9042. (g) Shi, Y.; Yee, G. T.; Wang, G.; Ren, T. *J. Am. Chem. Soc*. **2004**, *126*, 10552.

[2] (a) Fujita, M. *Chem. Soc. Rev*. **1998**, *27*, 417. (b) Leininger, S.; Olenyuk, B.; Stang, P. J. *Chem. Rev*. **2000**, *100*, 853. (c) Sweiger, G. F.; Malefetse, T. J. *Chem. Rev*. **2000**, *100*, 3483. (d) McCleverty, J. A.: Ward, M. D. *Acc. Chem. Res*. **1998**, *31*, 842. (e) Kaim, W.; Klein, A.; Glockle, M. *Acc. Chem. Res*. **2000**, *33,* 755.

[3] Creutz, C.; Taube, H. *J. Am. Chem. Soc*. **1969**, *91*, 3988. (b) Creutz, C.; Taube, H. *J. Am. Chem. Soc*. **1973**, *95*, 1086.

[4] (a) Tolbert, L. M.; Zhao, X.; Ding, Y.; Bottomley, L. A. *J. Am. Chem. Soc*. **1995**, *117*, 12891. (b) Sutter, J. P.; Grove, D. M.; Beley, M.; Collin, J. P.; Veldman, N.; Spek, A. L.; Sauvage, J. P.; Koten, G. V. *Angew. Chem., Int. Ed. Engl.*, **1994**, *33*, 1282.

[5] (a) Joachim, C.; Launay, J. -P.; Woitellier, S. *Chem. Phys*. **1990**, *147*, 131. (b) Ribou, A. -C.; Launay, J. –P.; Sachtleben, M. L.; Li, H.; Spangler, C. W. *Inorg. Chem*. **1996**, *35*, 3735.

[6] (a) Flanagan, J. B.; Margel, S.; Bard, A. J.; Anson, F. C. *J. Am. Chem. Soc*. **1978**, *100*, 4248. (b) Robin, M. B.; Day, P. *Adv. Inorg. Chem. Radiochem*. **1967**, *10*, 247.

[7] Chisholm, M. H.; Macintosh, A. M. *Chem. Rev*. **2005**, *105*, 2929.

[8] (a) Cotton, F. A.; Lin, C.; Murillo, C. A. *Acc. Chem. Res*. **2001**, 34, 759. (b) Cotton, F. A.; Lin, C.; Murillo, C. A. *Proc. Natl. Acad. Sci. USA* **2002**, *99*, 4810. (c) Xu, G. L.; Zou, G.; Ni, Y. H.; DeRosa, M. C.; Crutcheley, R. J.; Ren, T. *J. Am. Chem. Soc*. **2003,** *125,* 10057. (d) Miyasaka, H.; Campos-Fernandez, C. S.; Galan-Mascaros, J. R.; Dunbar, K. R. *Inorg. Chem*. **2000,** 39*,* 5870.

[9] (a) Furholz, U.; Burgi, H.-B.; Wagner, F. E.; Stebler, A.; Ammeter, J. H.; Krausz, E.; Clark, R. J. H.; Stead, M. J.; Ludi, A. *J. Am. Chem. Soc*. **1984**, *106*, 121. (b) Furholz, U.; Joss, S.; Burgi, H.-B.; Ludi, A. *Inorg. Chem*. **1985**, *24*, 943.

[10] *Multiple Bonds Between Metal Atoms*, Cotton, F. A.; Murillo, C. A.; Walton, R. A. Eds. 3rd ed. Springer Science and Business Media, Inc.: New York, 2005,

[11] Cotton, F. A.; Dalal, N. S.; Liu, C. Y.; Murillo, C. A.; North, J. M.; Wang, X. *J. Am. Chem. Soc.* **2003**, *125*, 12945.

[12] (a) Chisholm, M. H.; Patmore, N. J. *Dalton Trans.* **2006**, 3164. (b) Cotton, F. A.; Murillo, C. A.; Villagrán, D.; Yu, R. *J. Am. Chem. Soc*, **2006**, *128*, 3281.

[13] Chisholm, M. H., *Proc. Natl. Acad. Sci. U. S. A.* **2007,** 104, 2563.

[14] (a) Cayton, R. H.; Chisholm, M. H.; Huffman, J. C.; Lobkovsky, E. B. *J. Am. Chem. Soc.* **1991**, *113*, 8709.   (b) Bursten, B. E.; Chisholm, M. H.; Clark, R. J. H.; Firth, S.; Hadad, C. M.; Wilson, P. J.; Woodward, P. M.; Zaleski, J. M. *J. Am. Chem. Soc.* **2002**, *124*, 12244. (c) Bursten, B. E.; Chisholm, M. H.; Clark, R. J. H.; Firth, S.; Hadad, C. M.; Macintosh, A. M.; Wilson, P. J.; Woodward, P. M.; Zaleski, J. M. *J. Am. Chem. Soc.* **2002**, *124*, 3050.

[15] (a) Cotton, F. A.; Donahue, J. P.; Murillo, C. A. *J. Am. Chem. Soc.* **2003**, *125*, 5436. (b) Cotton, F. A.; Donahue, J. P.; Murillo, C. A.; Pérez, L. M. *J. Am. Chem. Soc.* **2003**, *125*, 5486.

[16] Chisholm, M. H.; Feil, F.; Hadad, C. M.; Patmore, N. J. *J. Am. Chem. Soc.* **2005**, *127*, 18150.

[17] (a) Byrnes, M. J.; Chisholm, M. H.; Clark, R. J. H.; Gallucci, J. C.; Hadad, C. M.; Patmore, N. J. *Inorg. Chem.* **2004**, *43*, 6334. (b) Chisholm, M. H.; D'Acchioli, J. S.; Hadad, C. M.; Patmore, N. J. *Inorg. Chem.* **2006**, *45*, 11035.

[18] Cotton, F. A.; Daniels, L. M.; Donahue, J. P.; Liu, C. Y.; Murillo, C. A. *Inorg. Chem.* **2002**, *41*, 1354.

[19] Cotton, F. A.; Liu, C. Y.; Murillo, C. A.; Villagrán, D.; Wang, X. *J. Am. Chem. Soc.* **2003**, *125*, 13564.

[20] Cotton, F. A.; Liu, C. Y.; Murillo, C. A.; Villagrán, D.; Wang, X. *J. Am. Chem. Soc.* **2004**, *126*, 14822.

[21] Beers, W. W. McCarley, R, E.; Martin, D. S.; Miskowski, V. M.; Gray, H. B.; Hopkins, M. D. *Coord. Chem. Rev.* **1999**, *187*, 103.

[22] McGinnis, R. N.; Ryan, T. R.; McCarley, R. E. *J. Am. Chem. Soc.* **1978**, *100*, 7900.

[23] (a) Cotton, F. A.; Liu, C. Y.; Murillo, C. A.; Wang, X. *Chem. Commun.* **2003**, 2190. (b) Cotton, F. A.; Liu, C. Y.; Murillo, C. A.; Zhao, Q. *Inorg. Chem.* **2006**, *45*, 9493.

[24] *SMART V 5.05 Software for the CCD Detector System*; Bruker Analytical X-ray System, Inc.: Madison, WI, 1998.

[25] *SAINT. Data Reduction Software. V 6.36A*; Bruker Analytical X-ray System, Inc.: Madison, WI, 2002.

[26] *SADABS. Bruker/Siemens Area Detector Absorption and Other Corrections. V2.03*; Bruker Analytical X-ray System, Inc.: Madison, WI, 2002.

[27] Sheldrick, G. M., *SHELXTL. V 6.12*; Bruker Analytical X-ray Systems, Inc.: Madison, WI, 2000.

[28] See for example: (a) Concolino, T. E.; Eglin, J. L.; Staples, R. J. *Polyhedron* **1999**, *18*, 915. (b) Bauer, C. B.; Concolino, T. E.; Eglin, J. L.; Rogers, R. D.; Staples, R. J. *Dalton Trans*. **1998**, 2813. (c) Eglin, J. L. *Comments Inorg. Chem*. **2002**, *23*, 23. (d) Dequeant, M.; Eglin, J. L.; Graves-Brook, M. K.; Smith, L. T. *Inorg. Chim. Acta*. **2003**, *351*, 141.

[29] Cotton, F. A.; Daniels, L. M.; Lin, C.; Murillo, C. A. *Inorg. Chem. Commun*. **2001**, *4*, 130.

[30] Cotton, F. A.; Feng, X.; Matusz, M. *Inorg. Chem.* **1989**, *28*, 594.

[31] (a) Creutz, C. *Prog. Inorg. Chem*. **1983**, *30*, 1. (b) Crutchley, R. J. *Adv. Inorg. Chem*. **1994**, *41*, 273. (c) Mosher, P. J.; Yap, G. P. A.; Crutchley, R. J. *Inorg. Chem*. **2001**, *40*, 1189. (d) DeRosa, M. C.; White, C. A.; Evans, C. E. B.; Crutchley, R. J. *J. Am. Chem. Soc*. **2001**, *123*, 1396.

[32] Cotton, F. A.; Pedersen, E. *Inorg. Chem*. **1975**, *14*, 399.

[33] Cotton, F. A.; Daniels, L. M. Hillard, E. A.; Murillo, C. A. *Inorg. Chem*. **2002**, *41*, 1639.

[34] Cotton, F. A.; Donahue, J. P.; Huang, P.; Murillo, C. A.; Villagrán, D.; Wang, X. *Z. Anorg. Allg. Chem.* **2005**, *631*, 2606.

[35] Cotton, F. A.; Liu, C. Y.; Murillo, C. A.; Zhao, Q. L., *Inorg. Chem.* **2006,** 45, 9480 and references therein.

[36] Fisher, H. M.; Lusi, A.; Egerton, R. J. *J. Pharm. Sci.* **1977**, *66*, 1349.

[37] (a) Hohenberg, P.; Kohn, W. *Phys. Rev.* **1964**, *136*, B864. (b) Parr, R. G.; Yang, W. *Density-Functional Theory of Atoms and Molecules*; Oxford University Press: Oxford, 1989.

[38] (a) Becke, A. D. *Phys. Rev. A* **1988**, *38*, 3098. (b) Becke, A. D. *J. Chem. Phys.* **1993**, *98*, 1372. (c) Becke, A. D. *J. Chem. Phys.* **1993**, *98*, 5648. (c) Lee, C.; Yang, W.; Parr, R. G. *Phys. Rev. B*. **1988**, *37*, 785.

[39] Adamo C.; Barone V. *J. Chem. Phys*. **1998**, *108*, 664.

[40] (a) Becke, A. D. *Phys. Rev. A.* **1988**, *38*, 3098 (b) Perdew, J. P. *Phys. Rev. B.* **1986**, 33, 8822.

[41] Gaussian 03, Revision C.02, Frisch, M. J.; Trucks, G. W.; Schlegel, H. B.; Scuseria, G. E.; Robb, M. A.; Cheeseman, J. R.; Montgomery, Jr., J. A.; Vreven, T.; Kudin, K. N.; Burant, J. C.; Millam, J. M.; Iyengar, S. S.; Tomasi, J.; Barone, V.; Mennucci, B.; Cossi, M.; Scalmani, G.; Rega, N.; Petersson, G. A.; Nakatsuji, H.; Hada, M.; Ehara, M.; Toyota, K.; Fukuda, R.; Hasegawa, J.; Ishida, M.; Nakajima, T.; Honda, Y.; Kitao, O.; Nakai, H.; Klene, M.; Li, X.; Knox, J. E.; Hratchian, H. P.; Cross, J. B.; Bakken, V.; Adamo, C.; Jaramillo, J.; Gomperts, R.; Stratmann, R. E.; Yazyev, O.; Austin, A. J.; Cammi, R.; Pomelli, C.; Ochterski, J. W.; Ayala, P. Y.; Morokuma, K.; Voth, G. A.; Salvador, P.; Dannenberg, J. J.; Zakrzewski, V. G.; Dapprich, S.; Daniels, A. D.; Strain, M. C.; Farkas, O.; Malick, D. K.; Rabuck, A. D.; Raghavachari, K.; Foresman, J. B.; Ortiz, J. V.; Cui, Q.; Baboul, A. G.; Clifford, S.; Cioslowski, J.; Stefanov, B. B.; Liu, G.; Liashenko, A.; Piskorz, P.; Komaromi, I.; Martin, R. L.; Fox, D. J.; Keith, T.; Al-Laham, M. A.; Peng, C. Y.; Nanayakkara, A.; Challacombe, M.; Gill, P. M. W.; Johnson, B.; Chen, W.; Wong, M. W.; Gonzalez, C.; and Pople, J. A.; Gaussian, Inc., Wallingford CT, 2004.

[42] (a) Dunning, T. H.; Hay, P. J. In *Modern Theoretical Chemistry. 3. Methods of Electronic Structure Theory*; Schaefer III, H. F., Ed.; Plenum Press: New York, 1977; pp.1-28. (b) Woon, D. E.; Dunning, T. H., *J. Chem. Phys.* **1993,** *98*, 1358.

[43] (a) Wadt, W. R.; Hay, P. J. *J. Chem. Phys.* **1985**, *82*, 284. (b) Hay, P. J.; Wadt, W. R. *J. Chem. Phys.* **1985**, *82*, 299.

[44] Casida, M. E.; Jamorski, C.; Casida, K. C.; Salahub, D. R. *J. Chem. Phys.* **1998**, *108*, 4439.

[45] Bryrnes, M. J.; Chisholm, M. H.; Dye, D. F.; Hadad, C. M.; Pate, B. D.; Wilson, P. J.; Zaleski, J. M. *J. Chem. Soc., Dalton Trans.* **2004**, 523.

[46] See for example: Cotton, F. A.; Daniels, L. M.; Lei, P.; Murillo, C. A.; Wang, X. *Inorg. Chem*. **2001**, *40*, 2778 and references therein.

[47] Cotton, F. A.; Gruhn, N. E.; Gu, J. D.; Huang, P.; Lichtenberger, D. L.; Murillo, C. A.; Van Dorn, L. O.; Wilkinson, C. C. *Science* **2002,** 298, 1971.

[48] Hush, N. S. *Coord. Chem. Rev*. **1985**, *64*, 135.

[49] Chisholm, M. H.; Pate, B. D.; Wilson, P. J.; Zalesky, J. M. *Chem. Commun*. **2002**, 1084.

[50] Cotton, F. A.; Dalal, N. S.; Hillard, E. A.; Huang, P. L.; Murillo, C. A.; Ramsey, C. M., *Inorg. Chem.* **2003,** 42, 1388.

[51] (a) Noodleman, L. J. *Chem. Phys.* **1981**, *74*, 5737. (b) Noodleman, L.; Baerends, E. J. *J. Am. Chem. Soc.* **1984**, *106*, 2316. (c) Noodleman, L.; Davidson, E. R. *Chem. Phys.* **1986**, *109*, 131. (d) Noodleman, L.; Peng, C. Y.; Case, D. A.; Mouesca, J.-M. *Coord. Chem. Rev.* **1995**, *144*, 199.

[52] Soda, T.; Kitagawa, Y.; Onishi, T.; Takano, Y.; Shigeta, Y.; Nagao, H.; Yoshioka, Y.; Yamaguchi, K. *Chem. Phys. Lett.* **2000**, *319*, 223.

[53] (a) Hille, R. *Chem. Rev.* **1996**, *96*, 2757. (b) Czjzek, M.; Santos, J.-P. D.; Pomier, J.; Giordano, G.; Méjean, V.; Haser, R. *J. Mol. Biol.* **1998**, *284*, 435. (c) Hânzelmann, P.; Schindelin, H., *Proc. Natl. Acad. Sci.* **2004,** 101, 12870. (c) Brondino, C. D.; Rivas, M. G.; Romao, M. J.; Moura, J. J. G.; Moura, I., *Acc. Chem. Res.* **2006,** 39, 788.

[54] (a) Enemark, J. H.; Cooney, J. J. A.; Wang. J. –J.; Holm, R. H. *Chem. Rev.* **2004**, *104*, 1175. (b) Carducci, M. D.; Brown, C.; Solomon, E. I.; Enermark, J. H. *J. Am. Chem. Soc.* **1994**, *116*, 11856.

[55] (a) Dunning, T. H. *J. Chem. Phys.* **1989**, *90*, 1007. (b) Wilson, A. K.; Woon, D. E.; Peterson, K. A.; Dunning, T. H. *J. Chem. Phys.* **1999**, *110*, 7667.

[56] Ayerst, E. M.; Duke, J. R. C. *Acta Crystallogr.* **1954**, *7*, 588.

[57] Chisholm, M. H.; Patmore, N. J. *Acc. Chem. Res.* **2007**, *40*, 19.

[58] Chisholm, M. H.; Clark, R. J. H.; Gallucci, J.; Hadad, C. M. Patmore, N. J. *J. Am. Chem. Soc.* **2004**, *126*, 8303.

[59] Chisholm, M. H.; Cotton, F. A.; Daniels, L. M.; Folting, K.; Huffman, J. C.; Iyer, S. S.; Lin, C.; Macintosh, A. M.; Murillo, C. A. *J. Chem. Soc., Dalton Trans.* **1999**, 1387.

[60] (a) Cotton, F. A.; Reid, A. H.; Schwotzer, W. *Inorg. Chem.* **1985**, *24*, 3965. (b) Pimblett, G.; Garner, C. D. *J. Chem. Soc., Dalton Trans.* **1986**, 1257.

[61] Byrnes M. J.; Chisholm, M. H. *Chem. Commun.* **2002**, 2040.

[62] The HOMO−1 (a_g) and SOMO (b_{3u}) are the in-phase and out-of-phase combinations of δ orbitals, and the HOMO−2 (a_g) is an in-phase combination of δ orbitals from the Mo_2 units.

[63] (a) Berlinguette, C. P.; Miyaji, T.; Zhang, Y. G.; Holm, R. H. *Inorg. Chem.* **2006,** *45*, 1997. (b) Rao, P. V.; Holm, R. H. *Chem. Rev.* **2004,** *104*, 527.

VITA

Zhong Li received his B.S. degree in chemistry from the Department for Intensive Instruction, Nanjing University in July of 2002. He began his graduate studies at Texas A&M University in September of 2002 and graduated in August 2007 with a Ph.D. under the advice of Prof. F. A. Cotton. His permanent address is: 138 East Fuqian Street, Suining, Jiangsu, 221200, China.